Università degli studi Roma Tre

Dipartimento di Fisica "Edoardo Amaldi"

Scuola Dottorale in Scienze Matematiche e Fisiche
Sezione di Fisica - XXII ciclo

Measurement of the K_L meson lifetime with the $K_L \to \pi^0\pi^0\pi^0$ decay

Coordinatore:
prof. Guido Altarelli

Relatori:
prof. Filippo Ceradini
dott. Antonio Passeri

Simona Serena Bocchetta

A.A. 2009

Io sono Lilith la dea delle due notti che torna dall'esilio.

Io sono Lilith la donna destino. Nessun maschio le è sfuggito, nessun maschio le vorrebbe sfuggire.

Le due lune Lilith.
Quella nera è completata dalla bianca, perché la mia purezza è la scintilla della dissolutezza, e la mia astinenza l'inizio del possibile. Io sono la donna-paradiso che cadde dal paradiso, e sono la caduta-paradiso.

estratto da "*Il ritorno di Lilith*" (2004) di

Joumana Haddad

Contents

Introduction

The KLOE experiment has been recording e^+e^- collisions at DAΦNE, the ϕ-factory at the Laboratori Nazionali di Frascati, from April 1999 to March 2006. The KLOE detector was designed to measure the CP-violating parameter $\mathrm{Re}(\varepsilon'/\varepsilon)$ in the neutral kaon system with an accuracy of $\sim 10^{-4}$. For this purpose, the DAΦNE collider was designed to work at the ϕ resonance peak ($\sqrt{s} \simeq 1020$ MeV) with high luminosity ($\sim 5\times 10^{32}$ cm^{-2} s^{-1}). Although the luminosity reached by DAΦNE was lower than the design value ($\sim 1.4\times 10^{32}$ cm^{-2} s^{-1}), many interesting physics measurements can be performed with the total integrated luminosity, ~ 2.5 fb^{-1}, collected by the KLOE experiment during 2001-02 and 2004-05 years, corresponding to $\sim 2.5\times 10^9$ $K_S K_L$ pairs produced.

This thesis is focused on one of these measurements, the lifetime of the K_L meson with the $K_L \to \pi^0\pi^0\pi^0$ decay channel.

The K_L lifetime is necessary to determine all the partial decay widths of the K_L from the measured branching ratios, and to extract the CKM matrix element $|V_{\mathrm{us}}|$ from K_L semileptonic decays. The determination of $|V_{\mathrm{us}}|$ from K_L semileptonic decays is dominated by the error on the measurement of the K_L lifetime.

The K_L lifetime was first measured more than 30 years ago [1] with an accuracy of $\sim 0.9\%$.

A new "direct" measurement with a relative error of $\sim 0.6\%$ has been recently published by the KLOE collaboration [2], based on ~ 400 pb^{-1} of data collected in 2001-02.

Moreover, an independent "indirect" K_L lifetime measurement (by requiring the costraint $\sum_i BR_i = 1$ where i is the K_L decay mode) with a relative error of $\sim 0.7\%$, based on the same data sample, has been published [3].

The aim of this thesis is to upgrade the K_L lifetime with ~ 1.2 fb^{-1} of data collected in 2005, to improve the statistical and the systematic error on this measurement.

In the first chapter, the neutral kaons physics is summarized, and the K_L lifetime measurement effects on $|V_{\mathrm{us}}|$ determination are reported.

The DAΦNE collider is described in the second chapter.

In the third chapter, the KLOE apparatus, calibration and monitoring procedures, data acquisition and reconstruction systems are described.

The fourth chapter is dedicated to the data sample and the method used to tag a K_L beam. The K_L decays are signaled by the $K_S \to \pi^+\pi^-$ identification in the opposite side of the detector.

The $K_L \to \pi^0\pi^0\pi^0$ event reconstruction and identification, based only on calorimeter information (photons from π^0 decay), is explained in chapter five, dedicated

to data analysis. The single photon vertex reconstruction efficiency and the spatial resolution of the K_L decay vertex are here analyzed, too.

Chapter six is dedicated to the signal selection to reject the residual background, the backgroung composition, and the selection efficiency.

In the seventh chapter, the fit results and the summary of the systematic uncertainties are shown, with a perspective of a final K_L lifetime result including also the 2004 data sample.

Chapter 1

Neutral kaon physics with KLOE

1.1 Neutral kaons phenomenology

In 1947, while studying cosmic-ray showers with a cloud-chamber, Rochester and Butler [4] observed a V-shaped track in the space below a lead plate (see Fig.1.1 on the left side). They explained this phenomenon as the decay in flight of a new heavy neutral particle with a mass about a thousand times the electron mass.

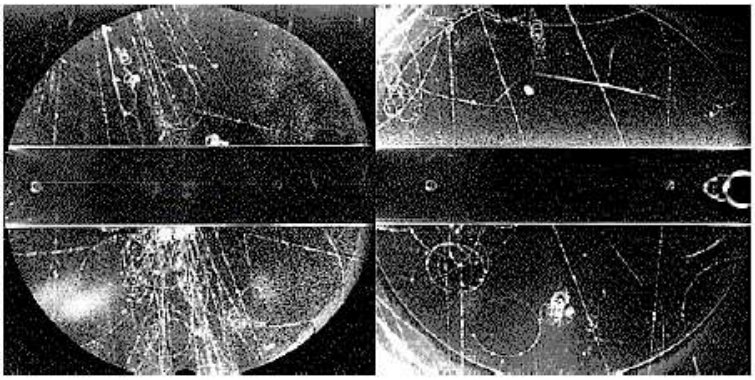

Figure 1.1: **Left**: The decay of the neutral kaon. A V-shaped track is visible in the space below the lead plate. **Right**: A charged kaon decay into a muon and a neutrino. The kaon comes in at the top right of the chamber and the decay occurs where the track appears to bend to the left abruptly.

This particle is now known as the neutral K-meson or neutral kaon (K^0). Though the kaons were produced with a frequency of a few percent relative to π-mesons, and therefore through strong interactions, their lifetime was about 10^{-10} seconds, a time characteristic of weak interactions. Because of this contradiction in behaviour between production and decay, they were called *strange* particles.

After few years, in 1953, Gell-Mann and Nishijima [5, 6] hypothesize the existence of a new quantum number, the *strangeness* (S), conserved in electromagnetic and strong interactions, but not in weak interactions, defined by the relation:

$$Q = I_3 + \frac{B}{2} + \frac{S}{2} \tag{1.1}$$

where Q is the electric charge, B the baryon number and I_3 the third component of isospin. A particle with strangeness $S \neq 0$ cannot decay into any non-strange particles system through interactions which conserve B, Q and I_3, as the strong interaction does. Hence, while strange particles can be produced in pairs through strong interactions of non-strange particles ("associated production"), the decays to non-strange particles can only occur through the weak interactions.

In 1955, Gell-Mann and Pais [7] pointed out that even though K^0 and $\overline{K}^0$ are expected to be different particles for the strong interaction, they could transform into each other through the action of weak interactions via the sequence $K^0 \rightarrow \pi^+\pi^- \rightarrow \overline{K}^0$. Gell-Mann and Pais proposed to represent the decay eigenstates as eigenstates of the operator C, the charge conjugation, that was supposed to be a valid symmetry for all interactions. As these eigenstates would decay through different channels, they should have different lifetimes and masses. In particular the state with $C = -1$ would not decay into the 2π state, and would therefore have a longer lifetime than the state with $C = +1$. A neutral particle with a long lifetime, $\tau > 10^{-9}$ s, consistent with the hypothesis of K^0-type was observed in 1956 [8]. However, it was the regeneration experiments proposed by Pais and Piccioni [9] that provided the decisive proof for the theory of Gell-Mann and Pais.

In 1957, experiments suggested by Lee and Yang [10] proved that the weak interactions are invariant neither under space-inversion nor under charge-conjugation [11, 12, 13]. Moreover, Lee, Oehme and Yang [14] pointed out that assuming only CPT invariance, the main features of the Gell-Mann and Pais theory would remain.

Meanwhile, Landau [15] proposed the combined symmetry CP of space-inversion and charge-conjugation observing that the Gell-Mann and Pais theory would not change by replacing C with CP.

In 1964 Christenson, Cronin, Fitch and Turlay [16] announced the discovery of the decay into two pions for the long-lived kaon. They found a frequency of the decay:

$$BR = \frac{K_L \rightarrow \pi^+\pi^-}{K_L \rightarrow \text{all}} = (2.0 \pm 0.4) \times 10^{-3} \tag{1.2}$$

demonstrating that CP was not conserved in weak decays of neutral kaons.

1.2 Mass and decay matrices

The neutral kaon system time evolution in the particle rest frame can be expressed using an effective 2×2 hamiltonian [17]:

$$|\psi(t)\rangle = A(t)|K^0\rangle + B(t)|\bar{K}^0\rangle \tag{1.3}$$

$$i\frac{\partial}{\partial t}\begin{pmatrix} A(t) \\ B(t) \end{pmatrix} = \begin{pmatrix} h & l \\ m & n \end{pmatrix}\begin{pmatrix} A(t) \\ B(t) \end{pmatrix} = (M - \frac{i}{2}\Gamma)\begin{pmatrix} A(t) \\ B(t) \end{pmatrix} \tag{1.4}$$

where h, l, m, and n are complex numbers, and M and Γ are 2×2 hermitian matrices, respectively the mass and the decay matrices:

$$M = \frac{H + H^\dagger}{2} = \begin{pmatrix} M_{11} & M_{12} \\ M_{21} & M_{22} \end{pmatrix} \tag{1.5}$$

$$\Gamma = i(H - H^\dagger) = \begin{pmatrix} \Gamma_{11} & \Gamma_{12} \\ \Gamma_{21} & \Gamma_{22} \end{pmatrix} \tag{1.6}$$

The total number of parameters is 8. If CPT invariance is imposed, the number of parameters is 6, since CPT requires that both the masses and the decay rates of K^0 and $\bar{K}^0$ have the same value:

$$M_{11} \overset{CPT}{=} M_{22} \qquad \Gamma_{11} \overset{CPT}{=} \Gamma_{22} \tag{1.7}$$

If CP is imposed, with the phase convention $CP|\ K^0\rangle = |\ \bar{K}^0\rangle$, all matrix elements are invariant under the exchange of indices $1 \leftrightarrow 2$:

$$\begin{array}{ll} M_{11} \overset{CP}{=} M_{22} & \Gamma_{11} \overset{CP}{=} \Gamma_{22}; \\ M_{12} \overset{CP}{=} M_{21} = M_{12}^* & \Gamma_{12} \overset{CP}{=} \Gamma_{21} = \Gamma_{12}^*. \end{array} \tag{1.8}$$

so, CP implies CPT invariance. If CP is assumed, the number of parameters in the effective hamiltonian reduces to 4, the mass eigenstates can be written as:

$$|K_1\rangle = \frac{|K^0\rangle + |\bar{K}^0\rangle}{\sqrt{2}} \quad (CP = +1) \tag{1.9}$$

$$|K_2\rangle = \frac{|K^0\rangle - |\bar{K}^0\rangle}{\sqrt{2}} \quad (CP = -1) \tag{1.10}$$

and decay according to the following way:

$$\begin{array}{lll} K_{Short} = K_1 \rightarrow & 2\pi & (CP = +1); \\ K_{Long} = K_2 \rightarrow & 3\pi & (CP = -1). \end{array} \tag{1.11}$$

where *Short* and *Long* labels correspond to the lifetime length of the neutral kaons due to the phase space.

After evidence of CP violation in the 1964, the eigenstates of the hamiltonian (the physical states K_S and K_L) were assumed to be superimpositions of the K^0 and $\bar{K}^0$ states:

$$|K_S\rangle = \frac{1}{\left[2\left(1 + |\epsilon_K + \delta_K|^2\right)\right]^{1/2}} \left\{ \left(1 + \epsilon_K + \delta_K\right) |K^0\rangle + \left(1 - \epsilon_K - \delta_K\right) |\bar{K}^0\rangle \right\} \tag{1.12}$$

$$|K_L\rangle = \frac{1}{\left[2\left(1 + |\epsilon_K - \delta_K|^2\right)\right]^{1/2}} \left\{ \left(1 + \epsilon_K - \delta_K\right) |K^0\rangle - \left(1 - \epsilon_K + \delta_K\right) |\bar{K}^0\rangle \right\} \tag{1.13}$$

with masses and widths, respectively, M_S, M_L and Γ_S, Γ_L, with eigenvalues:

$$\lambda_{S,L} = M_{11} - i\frac{\Gamma_{11}}{2} \pm \frac{\Delta\lambda}{2} = M_{S,L} - i\frac{\Gamma_{S,L}}{2} = \frac{1}{2}\frac{n - h \pm \sqrt{(h-n)^2 + 4lm}}{2l} \tag{1.14}$$

where:

$$\Delta\lambda = (M_S - M_L) - i\frac{\Gamma_S - \Gamma_L}{2} = 2\sqrt{\left(M_{12} - i\frac{\Gamma_{12}}{2}\right)\left(M_{12}^* - i\frac{\Gamma_{12}^*}{2}\right)} \tag{1.15}$$

The parameters ϵ_K and δ_K are two small complex numbers which describe CP and CPT violation in the Hamiltonian. Ignoring negligible quadratic terms, they are:

$$\epsilon_K = \frac{i\left(\mathrm{Im}\, M_{12} - i\mathrm{Im}\, \Gamma_{12}/2\right)}{\left[\left(M_S - M_L\right) - i\left(\Gamma_S - \Gamma_L\right)/2\right]} \tag{1.16}$$

$$\delta_K = \frac{\left(M_{11} - M_{22}\right) - i\left(\Gamma_{11} - \Gamma_{22}\right)/2}{2\left[\left(M_S - M_L\right) - i\left(\Gamma_S - \Gamma_L\right)/2\right]} \tag{1.17}$$

1.3 The K_L lifetime

Precision measurements of the neutral kaons lifetime are particularly difficult, since in general monochromatic beams of neutral particles cannot be prepared. Moreover, decays at rest cannot be observed since neutral kaons cannot be stopped.

KLOE is the ideal experiment, since it enjoys the availability of monochromatic beams. In fact, ϕ mesons at DAΦNE are produced almost at rest with a small transverse momentum (in the horizontal plane) of $\sim$13 MeV/c, so the K_S's and the K_L's are almost monochromatic and have a small momentum (p $\sim$ 110 MeV/c). In particular, the K_L lifetime value of $\sim$50 ns corresponds to a decay length of $\sim$3.4 m and a large fraction of K_L mesons ($\sim$50%) decays inside the KLOE detector.

While the K_S lifetime is known with very high accuracy, $(0.8958 \pm 0.0005) \times 10^{-10}$ s [18], this is not the case for the K_L lifetime.

The first K_L lifetime measurement [1] was performed more than 30 years ago at the Princeton-Pennsylvania Accelerator (PPA), where a K_L beam was created at a $\pi/2$ angle with respect to the 3 GeV proton beam incident on a platinum target. A scintillation-counter experiment measured the exponential decrease in K_L flux as a function of the distance from the target in a collimated neutral beam. The published result, got with 0.4 million events with a statistical error of $\sim$0.9%, is:

$$\tau_L = (51.54 \pm 0.44) \text{ ns} \tag{1.18}$$

KLOE published two K_L lifetime measurements, performed with different approaches:

- the first measurement was performed in 2005 with a sample of $\sim$400 pb^{-1} collected in the 2001-02 run. In this thesis a similar analysis procedure is applied. The K_L lifetime is "directly" obtained from a fit to the K_L proper time distribution in a time interval T; the proper time has been evaluated using the decay length for $K_L \to \pi^0\pi^0\pi^0$ decays. The geometrical features of the detector determine the time window T, since the K_L decays nearest the calorimeter wall are hardly reconstructed. Consequently, *ad hoc* cuts on the fiducial volume have been applied, to obtain a fit time window T for which the reconstruction efficiency is high and uniform within a fiducial volume of $\sim 0.4\lambda_L$. The result [2] obtained with 15 million events is:

$$\tau_L = (50.92 \pm 0.17_{\text{stat}} \pm 0.25_{\text{syst}}) \text{ ns}. \tag{1.19}$$

- the second measurement was performed with the same data sample, by imposing the constraint $\sum_i BR_i = 1$ on the K_L branching ratios. The four dominant K_L branching ratios ($K_L \to \pi^+\pi^-\pi^0$, $3\pi^0$, $\pi e\nu$, $\pi\mu\nu$) have been measured by KLOE, while the PDG '04 [19] provided the less probable branching ratios ($K_L \to \pi^+\pi^-$, $\pi^0\pi^0$, $\gamma\gamma$). The geometrical efficiency for the detection of K_L decays is τ_L-dependent:

$$\frac{BR(K_L \to f)}{BR^{(0)}(K_L \to f)} = 1 + 0.0128 \text{ ns}^{-1}(\tau_L - \tau_L^{(0)}), \tag{1.20}$$

  where $BR^{(0)}$ is the decay branching fraction evaluated with the "nominal" value for the K_L lifetime $\tau_L^{(0)}$. For each major K_L decay, there is a different

relation given by the Eq. 1.20. Joining these conditions to the requirement that the sum of all K_L branching ratios be equal to unity, the K_L lifetime and the four branching ratio values were determined independently of τ_L. The fit result [3], obtained with 13 million events, takes into account the correlation matrix between the K_L lifetime and the measured branching ratios, and is:

$$\tau_L = (50.72 \pm 0.11_{\text{stat}} \pm 0.35_{\text{syst}}) \text{ ns}. \tag{1.21}$$

The statistical error on the lifetime depends on the number of events and on the time interval according to the formula (see Ref. [20]):

$$\frac{\delta\tau}{\tau} = \frac{1}{\sqrt{N}} \times \left[\frac{-1 + e^{3T} + \left(e^T - e^{2T}\right)(3 + T^2)}{(-1 + e^T)^3} \right]^{-1/2}, \tag{1.22}$$

where $T = \Delta t/\tau$ is the time interval covered by the fit in lifetime units and N is the number of events present in that time interval.

This formula arises from the following considerations: the statistical accuracy achievable on a parameter p when a set of N measurements are performed on the quantity x, once the distribution function $f(x;p)$ is known, is given by:

$$\sigma_p = \sqrt{-\frac{1}{\frac{\partial^2 W}{\partial p^2}|_{p=\bar{p}}}} \tag{1.23}$$

where $W = \log \mathcal{L}$, $\mathcal{L} = \prod_{i=1}^{N} f(x_i;p)$ is the likelihood function and $\bar{p}$ is the best evaluation for p which maximizes $\mathcal{L}$. In our case the distribution function is $f(x;p) = e^{-t/\tau}$.

The behaviour of the statistical error given by Eq. 1.22 is shown in Fig. 1.2, on the left side for a constant number N of events, and on the right side with number of events $N \propto T$, which is approximately correct for small values of T. For instance, with T $\sim$ 0.36 and N $\sim 2{\times}10^7$ (this corresponds to our case, with $\sim$1.2 fb^{-1} of the 2005 run data), one can get, in principle, a statistical error of $\sim$0.13%.

The K_L lifetime has been measured in this thesis using the fully neutral $K_L \to \pi^0\pi^0\pi^0$ decay tagged by $K_S \to \pi^+\pi^-$ events. This decay channel has been chosen since it is necessary to maximize the number of tagged events and, at the same time, to avoid any interference among tagging and tagged events in order to minimize the systematic uncertainty. The aim is to improve the previous KLOE "direct" K_L lifetime measurement, by decreasing both the statistical and the systematic error.

1.4 The quark-mixing matrix

In the Standard Model (SM), quarks and leptons are both left-handed doublets and right-handed singlets. The quark mass eigenstates are different from weak eigenstates, and the SM postulates the following form of the Lagrangian for the charged-current weak interaction:

$$\mathcal{L}_{cc} = \frac{g}{\sqrt{2}} W_\alpha^+ \left(\bar{\mathbf{U}}_L \mathbf{V}_{CKM} \gamma^\alpha \mathbf{D}_L + \bar{e}_L \gamma^\alpha \nu_{eL} + \bar{\mu}_L \gamma^\alpha \nu_{\mu L} + \bar{\tau}_L \gamma^\alpha \nu_{\tau L} \right) + \text{ h.c.} \tag{1.24}$$

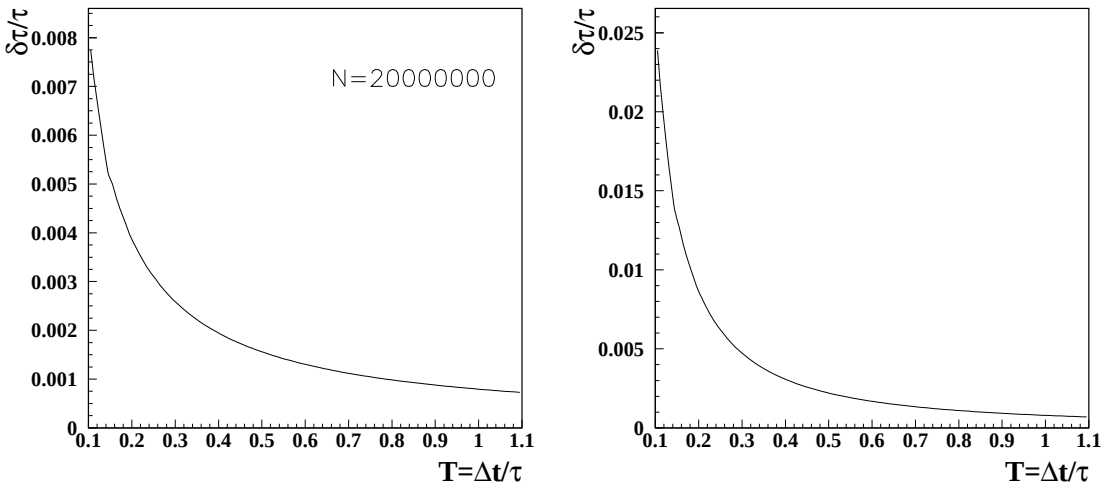

Figure 1.2: Lifetime statistical error as a function of the fit time range in lifetime units, for N=20 million events (**left**) and for $N \propto T$ (**right**).

where $\mathbf{U}^T = (u, c, t)$, $\mathbf{D}^T = (d, s, b)$ and L stands for lefthanded.

The 4-fermion Fermi coupling constant G_F is related to the gauge coupling g by the relation $G_F = g^2/(4\sqrt{2}M_W^2)$. Two outstanding properties arise: there is only one coupling constant for leptons and quarks, and quarks are mixed by the Cabibbo-Kobayashi-Maskawa unitary matrix [21, 22], V_{CKM}.

By convention, the quark mixing is expressed in terms of a 3×3 unitary matrix that acts on the quark eigenstates with charge $-e/3$ (d, s and b):

$$\begin{pmatrix} d' \\ s' \\ b' \end{pmatrix} = V_{CKM} \begin{pmatrix} d \\ s \\ b \end{pmatrix} = \begin{pmatrix} V_{ud} & V_{us} & V_{ub} \\ V_{cd} & V_{cs} & V_{cb} \\ V_{td} & V_{ts} & V_{tb} \end{pmatrix} \begin{pmatrix} d \\ s \\ b \end{pmatrix} \tag{1.25}$$

The mixing matrix can be parameterized by three mixing angles and a CP-violating phase. A standard choice, using the Maiani notation, is:

$$V_{CKM} = \begin{pmatrix} c_{12}c_{13} & s_{12}c_{13} & s_{13}e^{-i\delta} \\ -s_{12}c_{23} - c_{12}s_{23}s_{13}e^{i\delta} & c_{12}c_{23} - s_{12}s_{23}s_{13}e^{i\delta} & s_{23}c_{13} \\ s_{12}s_{23} - c_{12}c_{23}s_{13}e^{i\delta} & -c_{12}s_{23} - s_{12}c_{23}s_{13}e^{i\delta} & c_{23}c_{13} \end{pmatrix}, \tag{1.26}$$

where $s_{ij} = \sin\theta_{ij}$, $c_{ij} = \cos\theta_{ij}$, and δ is the KM phase which describes the CP-violating phenomena in flavor-changing processes in the Standard Model. The angles θ_{ij} can be chosen in the first quadrant, then s_{ij}, $c_{ij} \geq 0$. From experiments, it was found that $s_{13} \ll s_{23} \ll s_{12} \ll 1$, so it's convenient to use the Wolfenstein parameterization [23] to express this hierarchy:

$$V_{CKM} = \begin{pmatrix} 1 - \lambda^2/2 & \lambda & A\lambda^3(\rho - i\eta) \\ -\lambda & 1 - \lambda^2/2 & A\lambda^2 \\ A\lambda^3(1 - \rho - i\eta) & -A\lambda^2 & 1 \end{pmatrix} + \mathcal{O}(\lambda^4). \tag{1.27}$$

where

$$s_{12} = \lambda = \frac{|V_{us}|}{\sqrt{|V_{ud}|^2 + |V_{us}|^2}}, \qquad s_{23} = A\lambda^2 = \lambda \left| \frac{V_{cb}}{V_{us}} \right|, \tag{1.28}$$

$$s_{13}e^{i\delta} = V_{ub}^* = A\lambda^3(\rho + i\eta) = \frac{A\lambda^3(\bar{\rho} + i\bar{\eta})\sqrt{1 - A^2\lambda^4}}{\sqrt{1-\lambda^2}\,[1 - A^2\lambda^4(\bar{\rho} + i\bar{\eta})]}. \tag{1.29}$$

These relations ensure that $\bar{\rho} + i\bar{\eta} = -(V_{ud}V_{ub}^*)/(V_{cd}V_{cb}^*)$ is independent from the phase-convention, and guarantee the unitarity to all orders in λ of the CKM matrix written in terms of λ, A, $\bar{\rho}$, and $\bar{\eta}$. The definitions of $\bar{\rho}$, $\bar{\eta}$ reproduce all approximate results in the literature, for example:

$$\bar{\rho} = \rho(1 - \lambda^2/2 + \cdots) \qquad\qquad \bar{\eta} = \eta(1 - \lambda^2/2 + \cdots) \tag{1.30}$$

The Wolfenstein parameterization highlights our present knowledge of some of the matrix elements to $\mathcal{O}(\lambda^4)$, where $\lambda = \sin\theta_C$ is a real number that describes the s-d quark mixing given by the Cabibbo angle, θ_C. The CP-violating phase appears in only two off-diagonal matrix elements. A is a real number, too, and is close to one, $A \sim 0.84 \pm 0.06$, and $|\rho - i\eta| \sim 0.3$; $\eta \neq 0$ is required for CP-violation.

The CKM matrix elements are relevant parameters of the Standard Model, and they can all be determined from weak decays of the relevant quarks, to make tests of the unitarity. The unitarity of the CKM matrix implies

$$\sum_i V_{ij}V_{ik}^* = \delta_{jk} \qquad \text{and} \qquad \sum_j V_{ij}V_{kj}^* = \delta_{ik}$$

The six vanishing equations can be represented as triangles in a complex plane. The areas of all triangles are equal to half of the Jarlskog invariant, J [24], which is a phase-convention-independent measure of CP violation, defined by

$$\text{Im}\left[V_{ij}V_{kl}V_{il}^*V_{kj}^*\right] = J\sum_{m,n}\varepsilon_{ikm}\varepsilon_{jln}$$

A goal of flavor physics is to overconstrain the CKM matrix elements with different measurements that can be represented in the (ρ, η) plane. Since processes dominated by loop contributions are sensitive to new physics, they can be used to test the Standard Model.

The most common unitarity triangle, shown in Fig. 1.3, is defined by

$$V_{ud}V_{ub}^* + V_{cd}V_{cb}^* + V_{td}V_{tb}^* = 0, \tag{1.31}$$

Following Eq. 1.29 and 1.28, its vertices are (0,0), (1,0) and ($\bar{\rho}$,$\bar{\eta}$).

In particular, the CKM unitarity can be tested with kaon physics by checking the validity of the formula:

$$|V_{ud}|^2 + |V_{us}|^2 + |V_{ub}|^2 = 1 + \epsilon_{NP}, \tag{1.32}$$

by extracting the $|V_{\rm us}|$ from K_L semileptonic decays, as will be described in Sec. 1.5, and using the V_{ud} measurement from $0^+ \to 0^+$ nuclear β decays [25], while ϵ_{NP} parameterizes possible deviations from the Standard Model. The matrix element V_{ub} can be considered negligible, $|V_{ub}|^2 \sim 1.5 \times 10^{-5}$ [18].

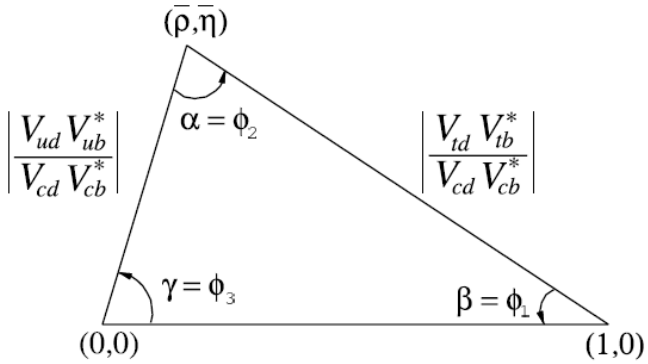

Figure 1.3: Scheme of the most common unitarity triangle.

1.5 Determination of the $|V_{\rm us}|$ matrix element

The $|V_{\rm us}|$ matrix element can be determined from hyperon, τ and kaon decays. Kaon semileptonic decays, being $0^- \to 0^-$ super-allowed Fermi transitions described only by Vector Current matrix elements, offer the cleanest way to extract $|V_{\rm us}|$.

The V_{us} matrix element appears in the kaon semileptonic decay width:

$$\begin{aligned}\Gamma(K_{\ell 3(\gamma)}) &= \frac{BR(K_{\ell 3(\gamma)})}{\tau_K} = \\ &= \frac{C_K^2 G_{\rm F}^2 M_K^5}{192\pi^3}|V_{\rm us}|^2|f_+(0)|^2 I_{K\ell} S_{\rm EW}\left(1+\delta_K^{SU(2)}+\delta_{K\ell}^{\rm EM}\right)^2 \end{aligned} \quad (1.33)$$

where $K = K^0, K^\pm, \ell = e, \mu$ and C_K^2=1/2, 1 for $K^\pm$ and K^0 respectively. $f_+(0) \equiv f_+^{K^0\pi^-}(0)$ is the $K \to \pi$ transition form factor, the hadronic matrix element at zero momentum transfer. Beside the value of $|f_+(0)|$, theory provides $S_{\rm EW} = 1.0232(3)$ for the universal short-distance electroweak correction (ref. [26]), the $SU(2)$-breaking $\delta_K^{SU(2)}$ (due to $m_u \neq m_d$) and long-distance electromagnetic corrections $\delta_{K\ell}^{EM}$, which depend on the kaon charge and on the lepton flavor (see Ref. [27]), given in Tab. 1.1. The dependence of the form factor on the momentum transfer, $t = (P-p)^2$, where P

	$\delta_K^{SU(2)}(\%)$	$\delta_{K\ell}^{EM}(\%)$
K_{e3}^0	0	+0.57(15)
K_{e3}^+	2.36(22)	+0.08(15)
$K_{\mu 3}^0$	0	+0.80(15)
$K_{\mu 3}^+$	2.36(22)	+0.05(15)

Table 1.1: Summary of the isospin-breaking corrections factors (see Ref. [28]). The electromagnetic corrections factors refer to the fully-inclusive $K_{\ell 3(\gamma)}$ rate.

and p are respectively the kaon and the pion momentum, is measured from the pion momentum spectrum; its knowledge is needed to evaluate the phase space integral $I_{K\ell}$. Beside this, experiments provide the measurement of the branching fraction, $BR(K_{\ell 3})$, the mass, M_K, the lifetime, τ_K, and of the Fermi constant. This is the best known quantity in Eq. 1.33: $G_F = 1.16637(1) \times 10^{-5}$ GeV^{-2} [18].

The KLOE experiment contributed to the determination of $\Gamma(K_{\ell 3})$ with the measurements of the semileptonic branching fractions, fully inclusive of final-state radiation, for neutral and charged kaons, the measurement of the neutral kaon mass and of the K_L and $K^{\pm}$ lifetimes.

The FlaviaNet Kaon Working Group presented in 2008 (Ref. [28]) a global analysis of leptonic and semileptonic kaon decays data, including all results by BNL-E865, KLOE, KTeV, ISTRA+ and NA48 experiments. Table 1.2 from Ref. [28] shows that the most promising way to improve the knowledge of $|V_{us}|\times f_+(0)$ is with the K_L meson. But, at the moment, the main source of error in the determination of $|V_{us}|$ from K_L semileptonic decays is the error of the K_L lifetime. The error on the K_L lifetime measurement contributes 0.19% and 0.18% to the value of $|V_{us}|$ derived, respectively, from $K_L \to \pi^{\pm} e^{\mp} \nu$ and $K_L \to \pi^{\pm} \mu^{\mp} \nu$ decays.

Decay mode	$\lvert V_{us}\rvert\times f_+(0)$	% error	BR	τ	δ	$I_{K\ell}$
$K_L \to \pi e \nu$	0.2163 (6)	0.28	0.09	0.19	0.15	0.09
$K_L \to \pi \mu \nu$	0.2168(7)	0.31	0.10	0.18	0.15	0.15
$K_S \to \pi e \nu$	0.2154(13)	0.67	0.65	0.03	0.15	0.09
$K^{\pm} \to \pi e \nu$	0.2173(8)	0.39	0.26	0.09	0.26	0.09
$K^{\pm} \to \pi \mu \nu$	0.2176(11)	0.51	0.40	0.09	0.26	0.15
average	0.2166(5)					

Table 1.2: Summary of $|V_{us}|\times f_+(0)$ determination from all kaon semileptonic decays. Last four columns represent the single contributions to the % error from equation 1.33: the error on the branching ratio, the lifetime τ, the theoretical inputs δ, and the phase space integral $I_{K\ell}$.

1.5.1 Semileptonic K_L decays

The semileptonic kaon decay (see Fig. 1.4) still yields the best way to obtain the

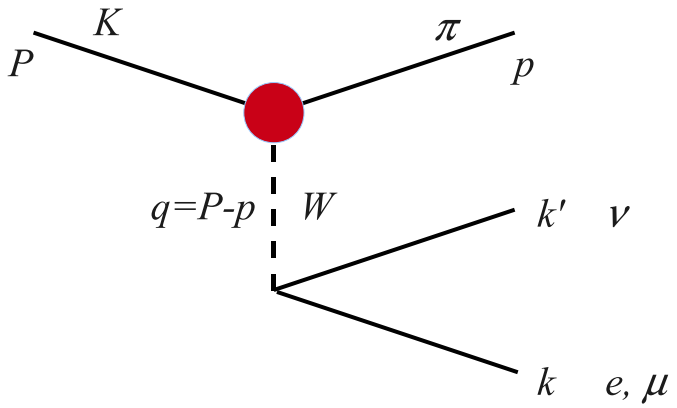

Figure 1.4: Amplitude for kaon semileptonic decay.

$|V_{us}|$ measurement, since only the vector part of the weak current contributes to the

matrix element $\langle\pi|J_\alpha|K\rangle$. In general:

$$\langle\pi|J_\alpha|K\rangle = f_+(t)(P+p)_\alpha + f_-(t)(P-p)_\alpha, \tag{1.34}$$

where P and p are respectively the kaon and pion four-momenta, and $t = (P-p)^2$ is the four-momentum transfer squared. The form factors (FF) f_+ and f_- appear because pions and kaons are not point-like particles and also reflect both $SU(2)$ and $SU(3)$ breaking. Introducing the scalar FF $f_0(t)$, the matrix element above is written in the form:

$$\begin{aligned}\langle\pi(p)|\bar{u}\gamma_\alpha s|K(P)\rangle = \\ = f_+(0) \times \left[(P+p)_\alpha \tilde{f}_+(t) + (P-p)_\alpha \left(\tilde{f}_0(t) - \tilde{f}_+(t)\right)\frac{\Delta_{K\pi}}{t}\right]\end{aligned} \tag{1.35}$$

where $\Delta_{K\pi} = M_K^2 - m_\pi^2$. The f_+ and f_0 FFs must have the same value at $t = 0$, so the term $f_+(0)$ has been factored out. If the FFs are expanded in powers of t up to t^2, four parameters (λ'_+, λ''_+, λ'_0 and λ''_0) can be determined by fitting the experimental pion decay spectrum, but they unfortunately turn out to be strongly correlated (see Ref. [29]).

Recently (Ref. [30]) both $\tilde{f}_0(t)$ and $\tilde{f}_+(t)$ have been expressed using a dispersion relation. A good approximation to both dispersive parameterization is:

$$\tilde{f}_{0,+}(t) = 1 + \lambda_{0,+}\frac{t}{m_\pi^2} + \frac{\lambda_{0,+}^2 + p_2}{2}\left(\frac{t}{m_\pi^2}\right)^2 + \frac{\lambda_{0,+}^3 + 3p_2\lambda_{0,+} + p_3}{6}\left(\frac{t}{m_\pi^2}\right)^3 \tag{1.36}$$

where the parameters p_2 and p_3 have slightly different values for $\tilde{f}_0(t)$ and $\tilde{f}_+(t)$, given in Tab. 1.3. This expression allows to evaluate the FFs slopes by fitting only

	Vector, $\tilde{f}_+(t)$	Scalar, $\tilde{f}_0(t)$
$p_2 \times 10^4$	5.84 ± 0.93	4.16 ± 0.50
$p_3 \times 10^4$	0.30 ± 0.02	0.27 ± 0.01

Table 1.3: Constants appearing in dispersive representations of vector and scalar form factors.

the two parameters λ_0 and λ_+ from the experimental pion decay spectra.

Finally, the phase space integrals for $K_{\ell 3}$ decays, obtained with the dispersive parameterizations of the FFs, are given in Tab. 1.4.

$I(K^0_{e3})$	$I(K^0_{\mu 3})$	$I(K^+_{e3})$	$I(K^+_{\mu 3})$
0.15477(35)	0.10262(47)	0.15913(36)	0.10559(48)

Table 1.4: Phase space integrals for $K_{\ell 3}$ decays, obtained using form factor slopes as determined with dispersive parameterization of the form factors.

Chapter 2

The DAΦNE collider

DAΦNE (**D**ouble **A**nnular Φ-factory for **N**ice **E**xperiments) is an e^+e^- collider designed for high luminosity at a center of mass energy of the ϕ resonance, a so-called ϕ-factory. The layout is shown in Fig. 2.1.

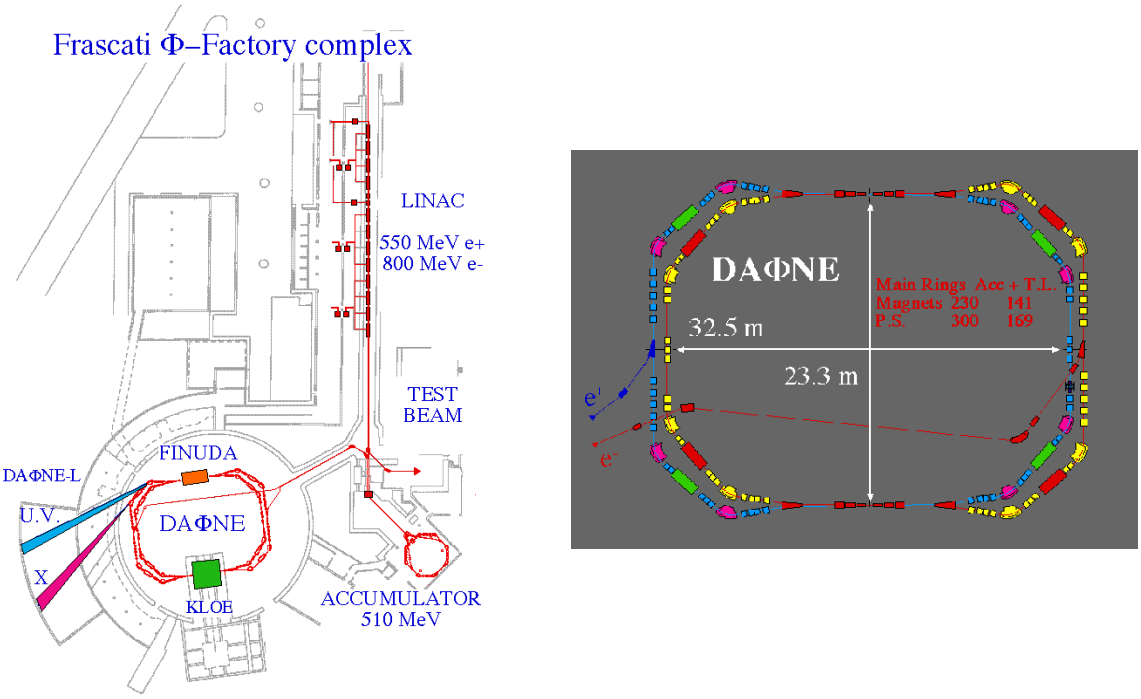

Figure 2.1: **Left**: The DAΦNE complex. **Right**: Schematic layout of the two DAΦNE Main Rings.

The heart of the collider is two rings where 120 bunches of electrons and positrons are stored. Each bunch collides with its counterpart once per turn. The two separate rings scheme is intended to minimize the perturbation of each beam on the other. Electrons and positrons are injected in the rings in bunches separated by 2.715 ns at the energy of ∼510 MeV, and collide at an angle of $(\pi - 0.025)$ radians. Electrons are accelerated to the final energy in the Linac (**Lin**ear **Ac**celerator), accumulated and cooled in the Accumulator and injected in the electron ring with a transfer line. Positrons require first electrons accelerated to 250 MeV to an intermediate station

in the Linac, where positrons are created in a thin target, then follow the same processing as electrons and are injected with another transfer line. Since the main rings beam intensity decays rapidly in time, the transfer cycle is repeated in average three times per hour to maintain high luminosity. The luminosity is defined by the beam parameters:

$$\mathcal{L} = n\frac{\nu N^+ N^-}{4\pi\sigma_x\sigma_y} \tag{2.1}$$

where n is the number of the bunches, each collecting N particles, ν is the revolution frequency in the storage ring, σ_x and σ_y are the standard deviations of the horizontal and vertical transverse beam profile at the interaction point. The main parameters of DAΦNE are summarized in Table 2.1.

Energy	0.51 GeV
Trajectory length	97.69 m
RF frequency	368.26 MHz
Harmonic number	120
Damping time, τ_E/τ_x	17.8/36.0 ms
Bunch length at full current e^-/e^+	2.8/2.2 cm
Beam currents e^-/e^+	2/1.4 Amps
Number of colliding bunches, n	108
σ_x	700 μm
σ_y	7 μm
σ_z	25 mm

Table 2.1: Parameters of DAΦNE during the 2004-2005 run period.

DAΦNE runs mostly at center-of-mass energy of $M_\phi \approx 1019.45$ MeV. The ϕ production cross section is $\sigma(e^+e^- \to \phi) \simeq 3.1$ μb.

The dominant ϕ meson decays [18] are shown in Tab. 2.2.

Decay mode	Branching ratio
K^+K^-	(48.9 $\pm$ 0.5)%
$K^0_L K^0_S$	(34.2 $\pm$ 0.4)%
$\rho\pi$ + $\pi^+\pi^-\pi^0$	(15.32 $\pm$ 0.32)%
$\eta\gamma$	(1.309 $\pm$ 0.024)%
$\pi^0\gamma$	(1.27 $\pm$ 0.06)$\times 10^{-3}$
e^+e^-	(2.954 $\pm$ 0.030)$\times 10^{-4}$
$\mu^+\mu^-$	(2.87 $\pm$ 0.19)$\times 10^{-4}$
$\eta\, e^+e^-$	(1.15 $\pm$ 0.10)$\times 10^{-4}$

Table 2.2: Main branching ratios of ϕ meson decays.

A ϕ factory is thus a copious source of monochromatic kaons, both neutral and charged. The production of a kaon with known energy and direction is guaranteed by the detection of the anti-kaon. This procedure will be called the *kaon tagging*

in the following. In this analysis the selection of K_L mesons will be based on the signature of a K_S meson.

The analysis is performed in the ϕ-meson center of mass. The ϕ-mesons produced in the collisions move in the laboratory system toward the center of the storage rings with a transverse momentum ∼13 MeV, corresponding to $\beta_\phi = 0.015$, $\gamma_\phi = 1.0001$. K mesons from ϕ-decays are therefore not monochromatic in the laboratory (see Fig. 2.2). The ϕ transverse momentum is measured run by run to high accuracy with Bhabha scattering events.

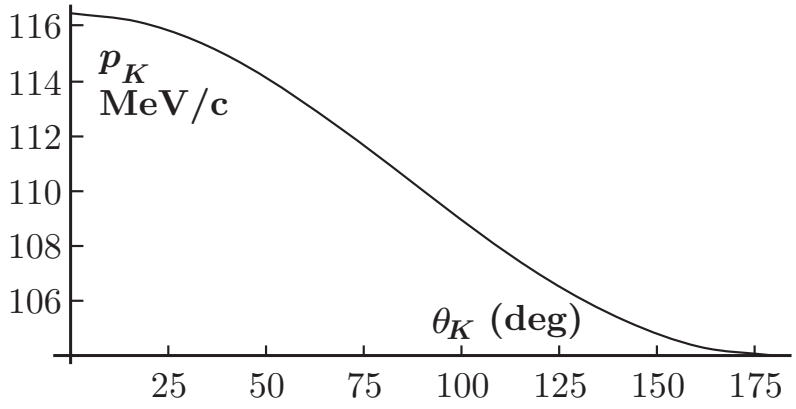

Figure 2.2: Laboratory momentum *vs* angle relative to the x-axis for K^0-mesons.

All discussion to follow refers to a system of coordinates with the x-axis in the horizontal plane, towards the center of DAΦNE, the y-axis vertical, pointing upwards and the z-axis bisecting the angle of the two beamlines (see sketch in Fig. 2.3). The

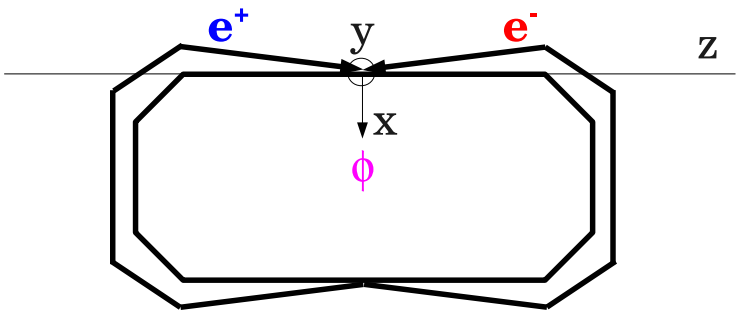

Figure 2.3: Sketch of the system of coordinates.

momentum of the neutral kaons varies between 104 and 116 MeV and is a single value function of the angle between the kaon momentum in the laboratory and the ϕ momentum, *i.e.* the x-axis. Knowledge of the kaon direction to a few degrees allows to determine to the ϕ-meson center of mass momentum (Fig. 2.2).

Chapter 3

The KLOE detector

A transverse view of the KLOE detector is shown in Fig. 3.1.

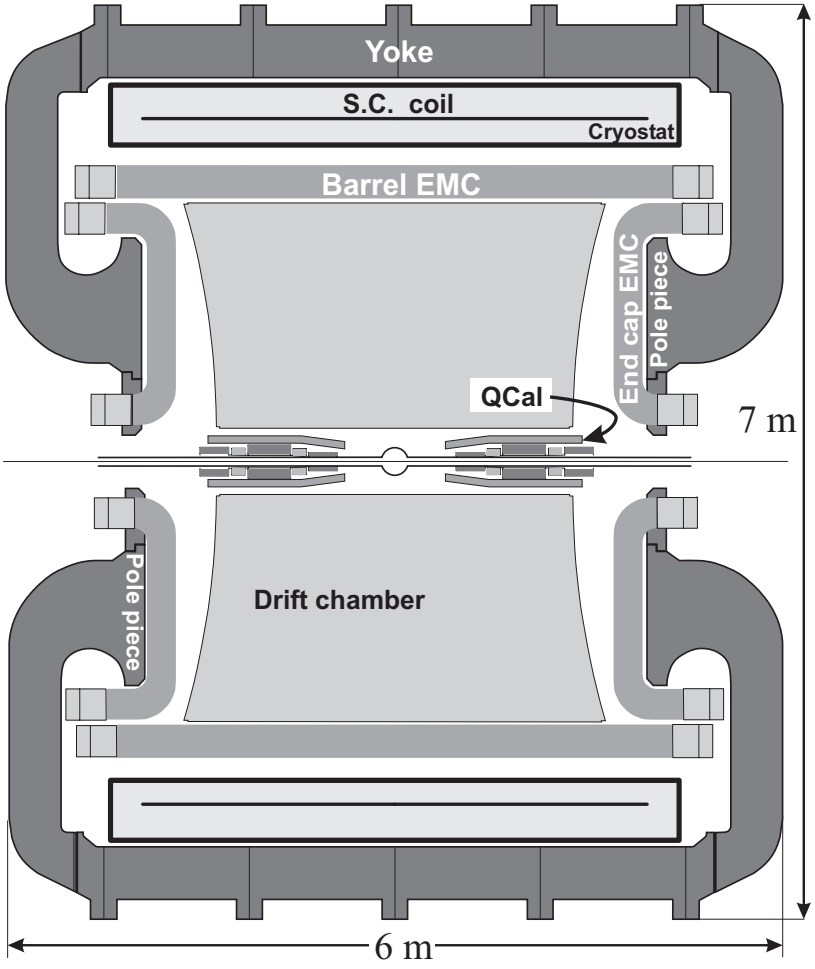

Figure 3.1: Vertical cross section of the KLOE detector, showing the interaction region (IP), the low-beta quadrupoles with the small quad-calorimeters (QCAL), the drift chamber (DC), the calorimeter (EMC), the superconducting coil, and the return yoke of the magnet.

The design was driven by the intent of being a definitive high precision experiment, while the size was dictated by the long decay length of the K_L meson. Kaons from ϕ-mesons decaying at rest travel at approximately one fifth of the speed of light; the mean path travelled by a K_L-meson $\lambda_L = \beta\gamma c\tau$ is 3.4 m; with a radius of about two meters, KLOE can catch $\sim$50% of K_L decays.

The major components of the detector that enclose the decay volume around the interaction point (IP) are, going outwards radially, a large tracking device to reconstruct the trajectory of charged particles, the Drift Chamber (DC), surrounded by a hermetic calorimeter to measure the energy and the entry point of neutral and charged particles, the Barrel and two Endcaps (EMC). The tracking chamber and the calorimeter are immersed in an axial magnetic field of 0.52 T, provided by a superconducting coil enclosed in its iron yoke. Two small calorimeters, QCAL, are wrapped around the low-beta quadrupoles placed at a distance of 46 cm from the IP to detect photons that otherwise will be absorbed.

The K_S decay length is $\sim$0.6 cm and the beam pipe at the interaction point is designed such that all K_S mesons decay in vacuum. A sphere of 10 cm radius made of an alloy composed of Beryllium and Aluminium, respectively in the proportions 62%-38%, is welded on the beam pipe, shown in Fig. 3.2. This is intended to minimize

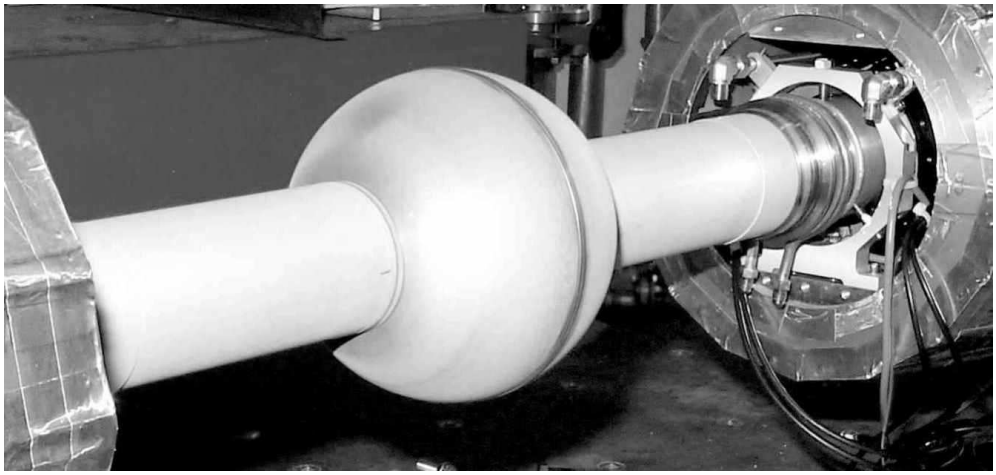

Figure 3.2: Beam pipe at the KLOE interaction region.

nuclear interactions, photon absorption and kaon regeneration, that mostly arises on the surfaces expanded in Fig. 3.3.

3.1 The Drift Chamber

The tracking chamber [31] design was motivated by the request to catch all the charged secondary products from a decay and measure their properties with high precision, without affecting the performance of the calorimeter in the detection of the neutral secondary products. Hence the detector requirement of being as transparent as possible. Moreover, the space resolution is limited by the multiple coulomb scattering that increases with the atomic number of the material. Another funda-

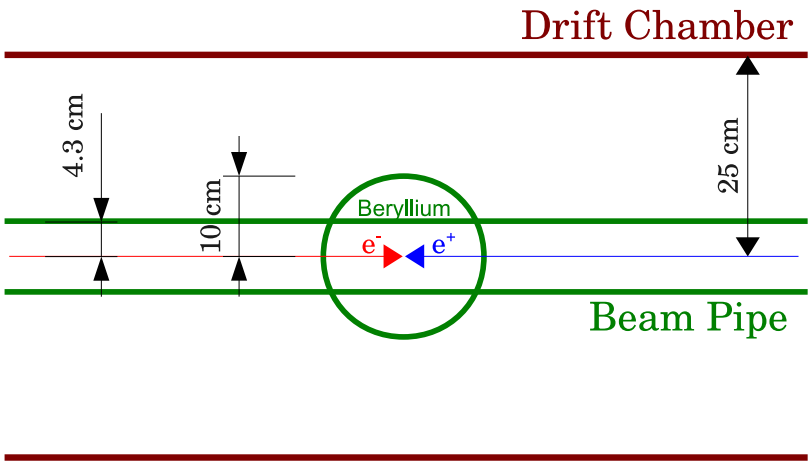

Figure 3.3: Regenerating surfaces geometry.

mental requirement is high efficiency in the reconstruction of secondary vertices, as uniform as possible in angle and distance from the IP.

The tracking detector is a large volume drift chamber with a wire configuration made of alternated stereo views, filled with a light gas mixture of 90% Helium and 10% Isobutane. The average value of the radiation length in the DC volume is $X_0 \sim$ 900 m, including the wire's contribution. The mechanical structure is made of carbon fiber composite, a low-Z and low density material, to minimize multiple coulomb scattering, absorption of photons and $K_L \rightarrow K_S$ regeneration, that simulates CP violating decays. The chamber volume is delimited by an outer cylinder of 2 m radius, an inner cylinder of 25 cm radius and closed by two 9 mm thick annular endplates. To hold the wire tension, the end-plates were pre-stressed to maintain a radius of curvature of 9.8 m.

The chamber has 12582 almost square drift cells with a ratio of anode to cathode wires of 3:1 arranged in 58 concentric cylinders inclined with alternated stereo angle that progressively increases with the radius. Since the track density is higher at small radii, the cells have 2×2 cm dimension in the 12 innermost layers and 3×3 cm in the other 48 layers.

Fig. 3.4 shows the wire geometry illuminated by light during the DC construction. The wires form a stereo angle ϵ with the z-axis as shown in more detail in Fig. 3.5.

Consecutive layers have alternating signs of the angle and its absolute value increases from 60 to 150 mrad with the layer radius while keeping fixed the 1.5 cm difference between the R_p and R_0 distance defined in Fig. 3.5 on the left. This design results in a uniform filling of the sensitive volume, with almost-square drift cells whose shape changes slowly along z, and results in a highly uniform tracking and vertex finding efficiency over the large sensitive volume.

To determine the space position from the measured drift time there is need to know the *space-time relation* describing the cell response. The whole DC geometry is described with 232 space-time relations, parametrized in terms of the angles β

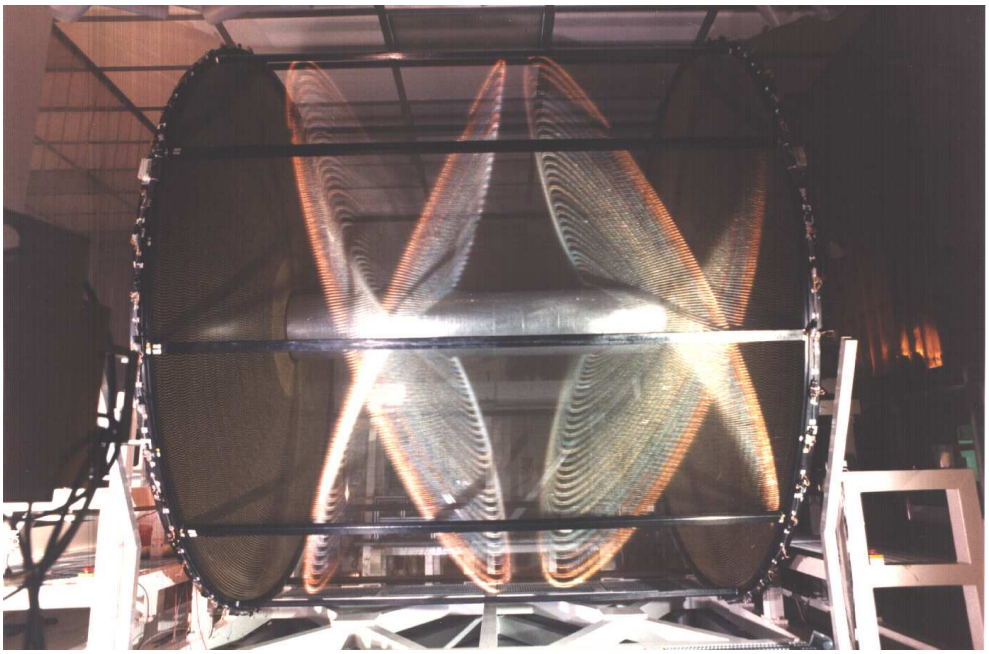

Figure 3.4: DC all stereo geometry.

and $\tilde{\phi}$ defined in Fig. 3.5 on the right. The β angle characterizes the geometry of the cell, directly related to the electric field shape. The $\tilde{\phi}$ angle gives the orientation of the particle trajectory in the cell's reference frame, in the transverse plane and with origin in the anode wire.

3.1.1 Tracking and vertexing

The presence of a signal on a wire of the drift chamber is called a *hit*. Once we have the hits, and the corresponding drift time, we can proceed with the event reconstruction using the wire geometry, the appropriate space-time relation and the map of the magnetic field.

This procedure follows three steps:

- pattern recognition;
- track fit;
- vertex fit.

The *pattern recognition* associates hits close in space in each stereo view to form track segments. These are joined to form track candidates and to provide a first estimate of the track parameters. Then the two stereo projections are merged to form the track and the *track fit* provides the final values of the parameters minimizing a χ^2 function based on the difference between the fit and the expected drift distances (residuals) as evaluated from a realistic knowledge of the cells response (measured drift times and space-time relation). This is an iterative procedure because the cells response depends on the track parameters. Finally the *vertex fit* searches for

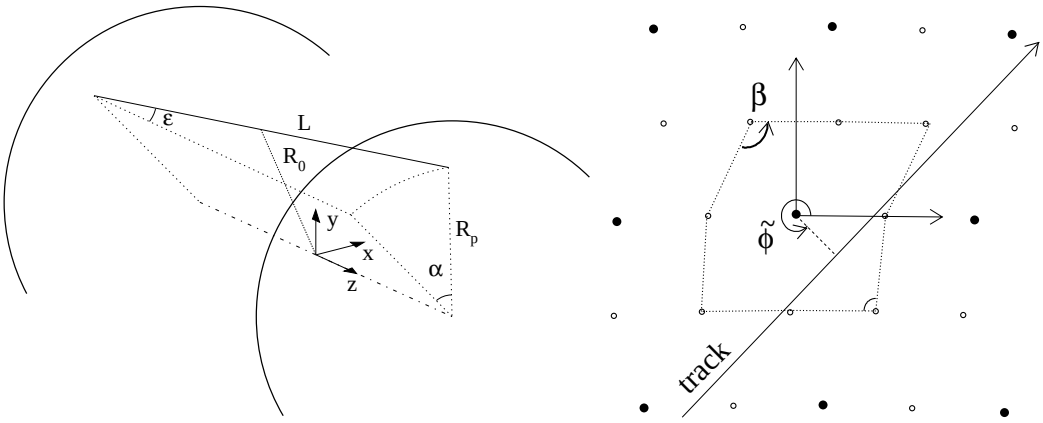

Figure 3.5: **Left**: Wire geometry with the definition of stereo angle ϵ between the wire of length L and the z-axis. **Right**: Definition of β and $\tilde{\phi}$ characterizing the shape of the cell and the angle of the incident track.

possible primary and secondary vertices, on the basis of the distance of closest approach between tracks.

3.1.2 Spatial resolution and calibration

The drift chamber provides tracking in three dimensions with a resolution of ∼200 μm in the bending plane, of ∼2 mm in the z direction and with a decay vertex resolution of ∼1 mm. The particle momentum is determined from the curvature of its trajectory in the magnetic field with a fractional accuracy of ∼0.4% for polar angles larger than 45°. The calibration of the absolute momentum scale has a fractional accuracy of few 10^{-4} determined using several two- and three-body processes ($e^+e^- \to e^+e^-$, $e^+e^- \to \mu^+\mu^-$, $K_L \to \pi l\nu$, $K_L \to \pi^+\pi^-\pi^0$, $K^\pm \to \mu^\pm\nu$, $K^\pm \to \pi^\pm\pi^0$) covering a wide momentum range.

Bhabha scattering events are in particular very useful for their clean signature and the high rate. They are routinely used to measure the beam-beam interaction point position, the ϕ transverse momentum, the center of mass energy, the beam-beam energy spread and the luminosity. The resolution on the measurements of these parameters on a run-by-run basis is summarized in Tab. 3.1 (see Ref. [32]).

Longitudinal beam-beam IP position (Δz)	(12.0 ± 0.1) mm
Horizontal beam-beam IP position (Δx)	(1.20 ± 0.05) mm
ϕ transverse momentum	(13.0 ± 0.1) MeV
Center of mass energy	(1019.5 ± 0.5) MeV
Beam-beam energy spread	(0.302 ± 0.001) MeV
Luminosity $\delta\mathcal{L}/\mathcal{L}$	0.6 %

Table 3.1: Measurements of the beam-beam interaction parameters using Bhabha scattering events.

However, to calibrate the DC response and to monitor the 232 space-time relations there is need for tracks with all possible orientations to simulate the K_L decay products. This is done with cosmic rays. A calibration program, incorporated into the KLOE online system, automatically starts at the beginning of each run and selects about 80,000 cosmic-ray events. These events are tracked using the existing space-time relations and the average value of the residuals for hits in the central part of the cells is monitored. If the residuals exceed 40 μm then about 300,000 cosmic-ray events are collected and a new set of calibration constants is obtained.

3.2 The Calorimeter

The calorimeter [33] has been designed to satisfy a set of stringent requirements such as providing a hermetic detection of low energy photons with high efficiency, a reasonably good energy resolution and an excellent time and space resolution to reconstruct the vertex for the K_L neutral decays. Then it is not only a calorimeter, but also a rough tracker and a time of flight detector. The calorimeter response has also to be fast since its signals are used to provide the main first-level trigger for the events.

The chosen solution for the EMC is a finely segmented sampling calorimeter, composed of lead passive layers and of scintillating fiber sensing layers. It is made of cladded 1 mm diameter scintillating fibers sandwiched between 0.5 mm thick lead foils. The foils are imprinted with grooves wide enough to accommodate the fibers and some epoxy, without compressing the fibers. This precaution prevents damage to the fiber-cladding interface. The epoxy around the fibers also provides structural strength and prevents light travelling in the cladding.

About 200 such layers are stacked, glued, and pressed, resulting in a bulk material. The resulting composite has a fibers:lead:glue volume ratio of 48:42:10 which corresponds to a density of 5 g/cm^3, an equivalent radiation length of $X_0 = 1.5$ cm and an electromagnetic sampling fraction of $\sim$13%. The large ratio of active material to radiator, the frequent signal sampling and the special fiber arrangement result in a factor $\sqrt{2}$ improvement in energy resolution with respect to calorimeter with slabs of equivalent scintillator to lead ratio.

This material is shaped into modules 23 cm thick ($\sim$15 X_0). 24 modules of trapezoidal cross section are arranged in azimuth to form the calorimeter barrel, aligned with the beams and surrounding the DC. An additional 32 modules with rectangular cross section, are wrapped around each of the pole pieces of the magnet yoke to form the endcaps, which hermetically close the calorimeter up to $\sim$98% of 4π, see Fig. 3.6. The unobstructed solid-angle coverage of the calorimeter as viewed from the origin is $\sim$94% [33].

The fibers run parallel to the axis of the detector in the barrel, vertically in the endcaps, and are connected at both ends to lucite light guides of area of 4.4×4.4 cm^2. The light guides are shaped as Winston cones with the other area coupled to the photocathode of fine mesh photomultipliers of 1.5 inches diameter with quantum efficiency of $\sim$20%. Thus each module is segmented in five consecutive layers each made of 4.4×4.4 cm^2 *calorimeter cells*. 4880 photomultiplier tubes view the 24+32+32 modules. The total length of scintillating fibers is 15,000 km.

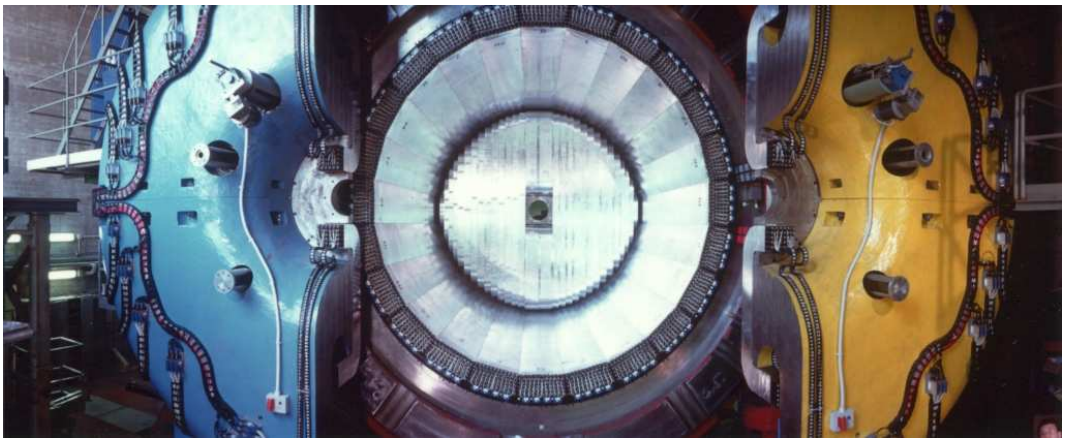

Figure 3.6: EMC viewed before DC insertion. Note endcaps attached to pole pieces seen in profile.

Fibers have attenuation length between 3 and 5 m. The light yield is of ∼35 photo-electron/layer for a minimum ionizing particle crossing a calorimeter module at the center.

3.2.1 Clustering

The calorimeter read-out granularity is defined by the light collection segmentation. The fiber's direction is referred to in the following as longitudinal. This segmentation provides the determination of the position of energy deposits in r-ϕ for the barrel and in x-z for the end-cap. Two ends of a calorimeter segment (cell) are labelled as A and B. For each cell, two time signals, $t_{A,B}$ and two amplitude signals $S_{A,B}$ are recorded from the corresponding PM's signals. The times $t_{A,B}$ (in ns) are related to $T_{A,B}$, the times in TDC counts, by the equations:

$$t_{A,B} = c_{A,B} \times T_{A,B}, \tag{3.1}$$

where $c_{A,B}$ (in ns/TDC counts) are the TDC calibration constants. The longitudinal position of the energy deposit is obtained from the difference $t_A - t_B$.

The particle arrival time t and its coordinate z along the fiber direction, the zero being taken at the fiber center, are obtained from $t_{A,B}$ as:

$$t(\text{ns}) = \frac{t_A + t_B}{2} - \frac{t_A^0 + t_B^0}{2} - \frac{L}{2v} \tag{3.2}$$

$$z(\text{cm}) = \frac{v}{2}\,(t_A - t_B - t_A^0 + t_B^0) \tag{3.3}$$

where $t_{A,B}^0$ are the overall time offsets, and L and v are respectively the cell length (cm) and the light velocity in the fibers (cm/ns). The energy signal, E, on each side of a cell i is obtained from S as

$$E_{A,B}^i(\text{MeV}) = \frac{S_{A,B}^i - S_{A,B}^{0,i}}{S^{mip,\,i}} \times k_E \tag{3.4}$$

All signals S above are in ADC counts. $S^{0,i}$ are the zero-offsets of the amplitude scale. $S^{mip,i}$ is the response for a minimum ionizing particle crossing the calorimeter center. Dividing by $S^{mip,i}$ Eq. 3.4 above accounts for PM response, fiber light yield and electronics gain. k_E gives the energy scale in MeV, and it is obtained from showering particles of known energy.

In order to obtain a calorimeter response independent of the position, a correction factor $A^i_{A,B}(z)$, due to the attenuation along the fiber length, is applied. The cell energy, E_i, is taken as the mean of the determinations at both ends:

$$E_i(\text{MeV}) = \frac{E^i_A A^i_A + E^i_B A^i_B}{2}. \tag{3.5}$$

The determination of the absolute energy scale relies instead on the use of the monochromatic source of 510 MeV photons: the $e^+e^- \to \gamma\gamma$ sample. This calibration is routinely done each 200-400 nb^{-1} of integrated luminosity (*i.e.*, approximately every 1-2 hours during normal data taking). For the timing, the relative time offsets of each channel, t_{i0}, related to cable lengths and electronic delays and the light velocity in the fibers are evaluated every few days with high momentum cosmic rays selected with DC information. An iterative procedure uses the extrapolation of the tracks to the calorimeter to minimize the residuals between the expected and measured times in each cell. A precision of few tens of picoseconds is obtained for these offsets.

The clustering procedure associates different hits in the calorimeter cells in a single cluster as due to the same particle. Each group collects hit cells which are close to each other. Among these, the cell with highest energy release is found; then, the nearest hit cells are associated to that highest one, in order to reconstruct a cluster.

The cluster energy is obtained by adding the energy released in the nearest cells:

$$E_{clu} = \sum_i E_i, \tag{3.6}$$

where i is the index of the cell number.

The cluster position is evaluated as the energy-weighted average of the cell coordinates:

$$\vec{R}_{clu} = \frac{\sum_i E_i \vec{R}_i}{\sum_i E_i}, \tag{3.7}$$

where $\vec{R}_i = (x_i,\ y_i,\ z_i)$, z_i is the cell coordinate along the fiber (see Eq. 3.3), and x_i, y_i are the nominal positions of the cell.

Finally, the cluster time is obtained in an analogous way:

$$T_{clu} = \frac{\sum_i E_i t_i}{\sum_i E_i}, \tag{3.8}$$

where t_i are evaluated as in Eq. 3.2.

3.2.2 Time, energy and spatial resolution

After the description of the calibration and monitoring procedures, the resolution of the calorimeter is here summarized.

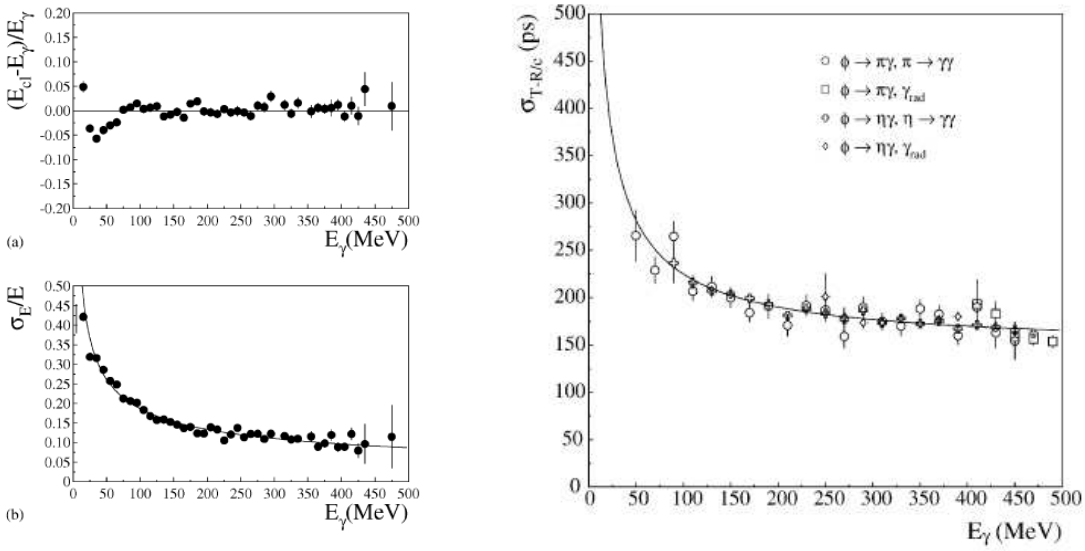

Figure 3.7: **Top left**: Energy linear response $(E_{clu} - E_\gamma)/E_\gamma$ vs. E_γ; **Bottom left**: Energy resolution vs. E_γ as a function of E_γ; both the curves are obtained with radiative Bhabha events $e^+e^-\gamma$; the fit result obtained is given by Eq. 3.9. **Right**: Time resolution as a function of E_γ for ϕ radiative decays.

The energy resolution function (see Fig. 3.7 on the left side) is determined with radiative Bhabha events, $e^+e^- \to e^+e^-\gamma$, where E_γ is measured by the DC tracking:

$$\frac{\sigma_E}{E_\gamma} = \frac{0.057}{\sqrt{E_\gamma\,(\mathrm{GeV})}} \tag{3.9}$$

The intrinsic time resolution is $\sigma_t = 57$ ps$/\sqrt{E\ (GeV)}$ dominated by photoelectron statistics (see Fig. 3.7 on the right side).
A constant term determined from $e^+e^- \to \gamma\gamma$, radiative ϕ decays and $\phi \to \pi^+\pi^-\pi^0$ events has to be added in quadrature. This constant term is shared between a channel by channel uncorrelated term and a term common to all channels. The uncorrelated term is mostly due to the calorimeter calibration while the common term is related to the uncertainty of the event T_0, arising from the DAΦNE bunch-length and from the jitter in the trigger phase-locking to the machine RF. By measuring the average and the difference of $T_{clu} - R_{clu}/c$ for the two photons in $\phi \to \pi^+\pi^-\pi^0$ events, a similar contribution of $\sim$100 ps for the two terms has been estimated. Thus the resolution is:

$$\sigma_t = 57\ \mathrm{ps}/\sqrt{E\ (GeV)} \oplus 140\ \mathrm{ps}. \tag{3.10}$$

In the same way, using control samples where the photon direction is measured with the DC, the cluster position resolution function has been determined. The resolution is 1.3 cm in the coordinate transverse to the fibers and of 1.2 cm$/\sqrt{E\ (GeV)}$ in the coordinate along the fibers. This enables to localize the $\gamma\gamma$ vertex in $K_L \to \pi^+\pi^-\pi^0$ decays with $\sigma \simeq 2$ cm along the K_L line of flight as reconstructed from the tagging K_S decay.

The quadrupole calorimeter

Two triplets of permanent quadrupoles for the beam final focus are located inside the detector starting from a distance of 46 cm from IP, and surrounding the beam pipe, as shown in Fig. 3.8.

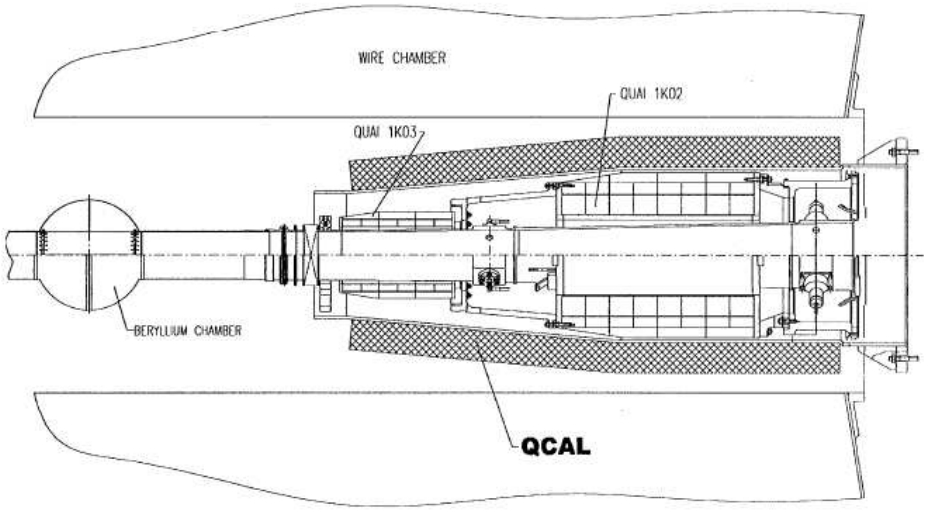

Figure 3.8: One side of the interaction region. Two permanent quadrupoles are shown together with the surrounding calorimeter (QCAL) corresponding to the shaded area, starting at a distance of 46 cm from the IP (the center of the sphere in the sketch).

The quadrupoles of this low-beta insertion are equipped with two calorimeters made of lead plates and scintillator tiles of $\sim 5X_0$ thickness, called QCAL [34]. The task of QCAL is to identify photons from $K_L \to \pi^0\pi^0\pi^0$ decays that would mimic the CP-violating $K_L \to \pi^0\pi^0$ decay if the photon would be absorbed by the quadrupoles.

Each calorimeter consists of a sampling structure of lead and scintillator tiles arranged in 16 azimuthal sectors. The readout is done with plastic wavelength shifting (WLS) fibers coupled to mesh photomultipliers. The arrangement of the WLS fibers allows the measurement of the longitudinal z coordinate by time difference. Although the tiles are assembled in a way to optimize the efficiency for photons originated in K_L decays, a high efficiency is in fact also obtained for photons coming from the IP. This allows to extend the calorimeter coverage of the solid angle down to $\cos\theta = 0.99$.

3.3 The trigger

Event rates at DAΦNE are high: at a luminosity of 10^{32} cm^{-2} s^{-1} up to 300 ϕ decays and 30,000 Bhabha events are produced per second in the KLOE acceptance. The trigger design [35] is optimized to retain all ϕ decays. Moreover, all Bhabha and e^+e^- $\rightarrow \gamma\gamma$ events produced at large polar angles are accepted for detector monitoring and calibration, as well as a downscaled fraction of cosmic rays, which cross the detector at a rate of 3000 Hz. Finally, the trigger provides efficient rejection of the two main sources of background: small angle Bhabha scattering events, and particle lost from the DAΦNE beams, resulting in very high photon and electron fluxes in the interaction region.

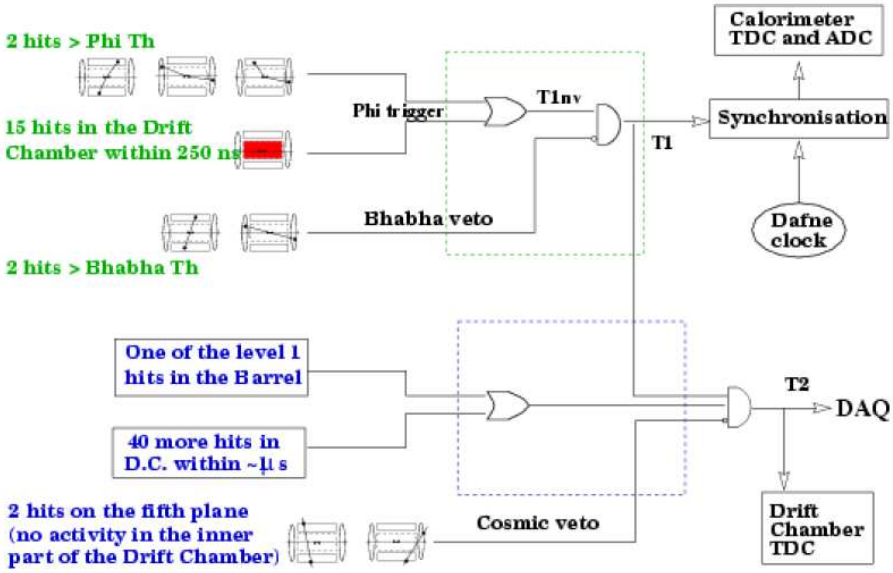

Figure 3.9: KLOE trigger logical scheme.

The trigger logic, shown in Fig. 3.9, rapidly recognizes event topologies and energy deposits of interest processing the signals from the DC and the EMC. Since ϕ decay events have a relatively high multiplicity, they can be efficiently selected by the EMC trigger by requiring at least two isolated energy deposits in the calorimeter ($\geq$ 2 trigger sectors [1]) above a given threshold. The threshold for most of the data was chosen 50 MeV in the barrel and 150 MeV in the endcaps. Events with only two trigger sectors in the same endcap are not accepted, because this topology is dominated by machine background. Events with charged particles give a large number of hits in the DC. The trigger uses the information from groups of DC drift cells requiring the presence of at least 15 hits within a time window of 250 ns from the beam crossing.

An event satisfying at least one of the two above conditions generates a first level trigger, **T1**, which is produced with minimal delay and is synchronized with the DAΦNE RF clock. The T1 signal initiates the data conversion in the front-end

[1] A trigger sector collects PM signals from adjacent columns of the calorimeter, see Ref. [35] for barrel and endcaps scheme.

electronics circuits and enables the second level trigger. The second level trigger logic **T2** verifies the EMC trigger and, in case of a DC trigger, requires at least 120 DC hits within a 1.2 μs time window.

Data conversion and readout is done in a fixed time of 2 μs following the T1 signal. The logic OR of two independent triggers allows to evaluate the trigger efficiency for the different analyses.

The trigger also implements a logic to flag cosmic-ray events, which are recognized by the presence of two energy deposits above 30 MeV in the outermost calorimeter layers. Such events are rejected after partial reconstruction by an online software filter. A fraction of downscaled cosmic-ray events is anyway retained to evaluate the trigger efficiency.

3.4 Data acquisition and processing

At a luminosity of 10^{32} cm^{-2} s^{-1}, the trigger rate is ∼2000 Hz. Of these, ∼500 Hz are from ϕ decays or Bhabha scattering. All digitized signals from the calorimeter, drift chamber, calibration and monitoring systems are fed via optic fibers from the front-end electronics, placed on platforms mounted on the KLOE iron yoke, to the computers in the near-by building. The Data Acquisition architecture has been designed to sustain a throughput of 50 Mbytes/s all along this path. In the near-by control room one can see real time displays of reconstructed charged tracks traversing the DC and energy clusters in the EMC. The display of two events is shown in Fig. 3.10.

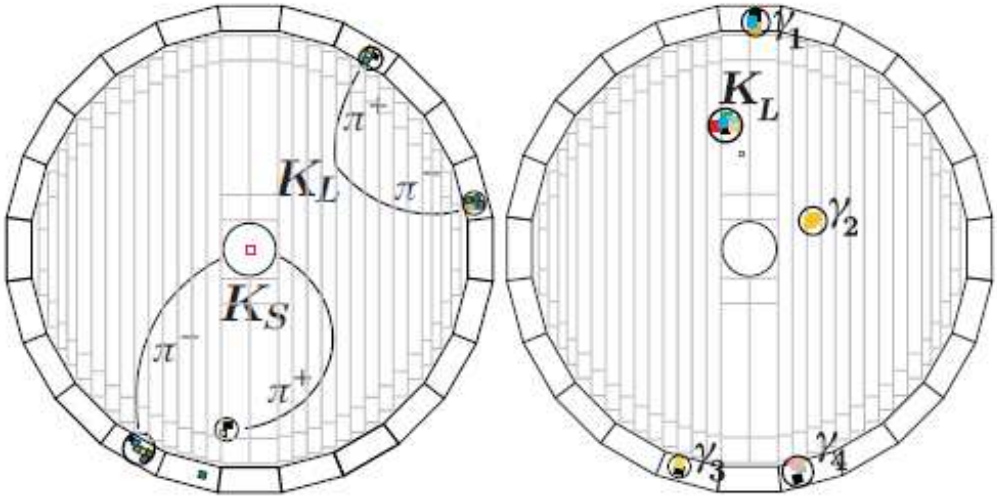

Figure 3.10: K_SK_L events in KLOE. **Left**: Both K_L and K_S decay to charged pions $\pi^+\pi^-$. Coloured areas indicate energy in the calorimeter. **Right**: 5 neutral particles. γ_1 through γ_4 are showers from 4 photons from $K_S \to \pi^0\pi^0 \to 4\ \gamma$. The K_L-meson reaches the calorimeter before decaying. It literally crashes in the EMC, producing a large energy release.

The events are reconstructed, *i.e.* charged tracks and energy deposits that occurred at the same instant in time on the various subcomponents of the detector

are associated together, properly labelled and packed into a unique data file. To optimize the event reconstruction we use continuously updated calibration constants for the time and energy scales. Furthermore, background hits are acquired using a random trigger, which are recorded to be used in the Monte Carlo (MC) simulation of events.

The MC simulation program [36, 37] reproduces accurately the detector geometry, the response of the detectors and the trigger requirements (see Sec. 3.7). The background is then added for groups of runs taken in comparable background conditions.

All these tasks need to be performed without adding dead time and assuring the completeness of every collected event.

The KLOE DAQ scheme is shown in Fig. 3.11. The DAQ readout system involves some 23,000 channels of FEE (Front End Electronics) from calorimeters, tracking chamber and trigger. For each trigger, relevant data coming from the whole FEE have to be concentrated in a single CPU, where a dedicated process builds the complete event. For this aim, a three-level data concentration scheme has been implemented (see Fig. 3.11):

- **L1** level gathers single event data within a single FEE crate;
- **L2** level combines the information from several crates;
- the third level is responsible for final event building and subsequent monitor and storage tasks.

All raw data for interactions and background, physics and MC reconstructed events are recorded on tape. KLOE has a huge tape library of ∼800 TB capacity [38]. At reconstruction time, events are classified into broad categories, called *streams*. Data summary tapes are produced with a separate procedure.

3.5 FILFO filtering

After data acquisition, the event is analyzed with the background rejection filter, FILFO (*FILtro del FOndo*). The background rejection algorithm is based on cluster formation and on DC cells counts, so background events are rejected before the reconstruction in the drift chamber, the sub-detector more involved in reconstruction algorithms processing. FILFO is in charge of cosmic rays contamination and machine background rejection. To identify background events, some cuts are applied, studied to minimize the signal loss. Irrespective of the FILFO selection, a fraction of events is anyway kept to monitor the FILFO rejection factor.

3.6 Event reconstruction

Event reconstruction algorithms correspond to modules that perform on the offline farm the following tasks (see Ref. [39]):

- loading of DC and calorimeter calibration constants;

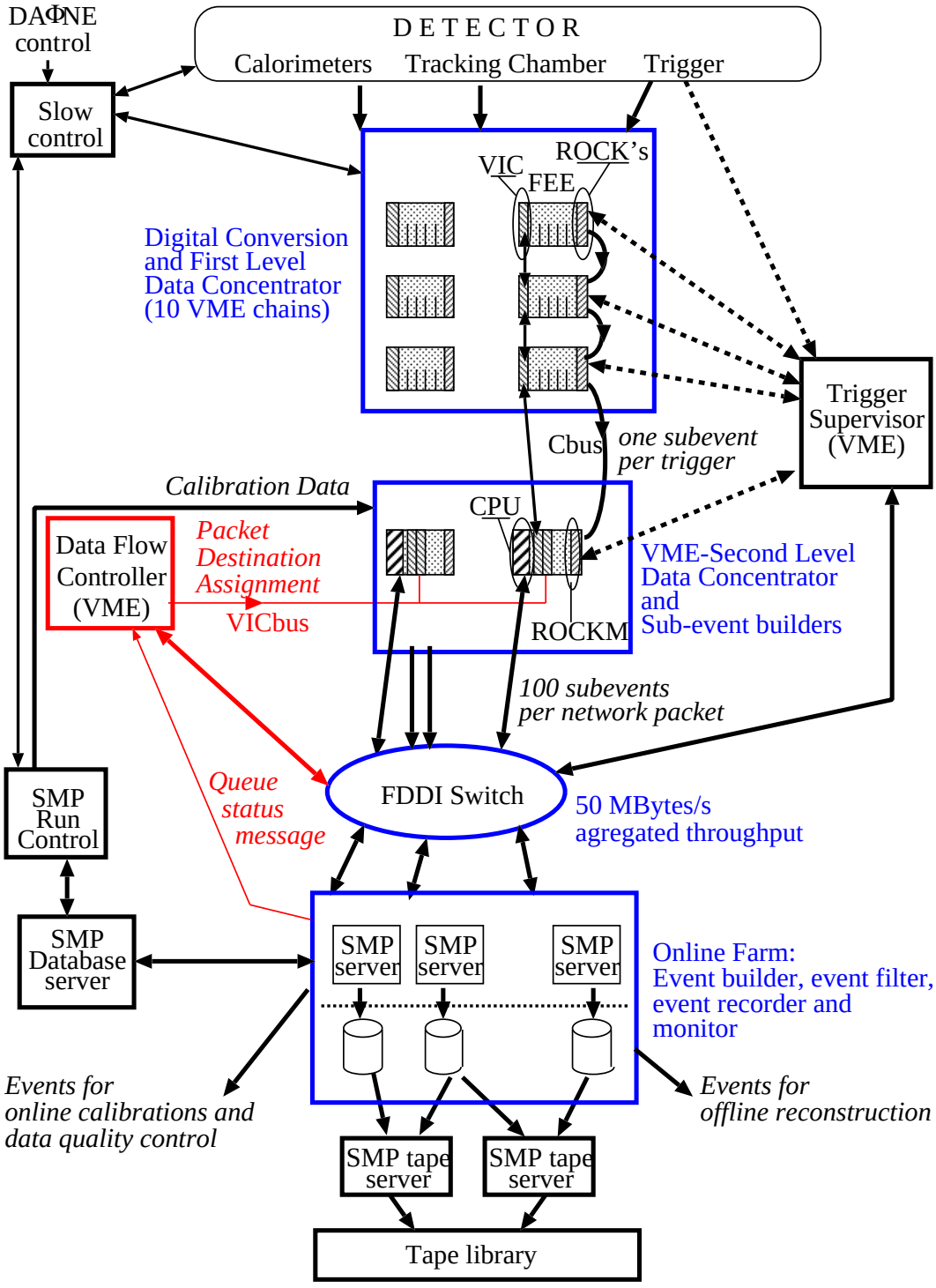

Figure 3.11: DAQ architecture.

- calorimeter cluster reconstruction from single cells and evaluation of deposited energy and time of flight (as described in Sec. 3.2.1);
- determination of the correct bunch crossing (see next Sec. 3.6.1);
- rejection of machine-background and cosmic-ray events;
- pattern recognition and track fitting for charged particles in the DC (see Sec. 3.1.1);
- vertex reconstruction for charged particles (see Sec. 3.1.1);
- association of DC tracks with calorimeter clusters (this algorithm will be explained in Sec. 3.6.2);
- event classification (see next Sec. 3.6.3).

3.6.1 Bunch-crossing identification

DAΦNE operates with 120 bunches per ring, that correspond to a bunch-crossing period $T_{RF} = 2.715$ ns. Due to the short bunch-crossing period and the large spread of the particle arrival times, the trigger is not able to identify the bunch crossing related to each event, which has to be determined offline.

The start signal for the electronics devoted to time measurement (TDC) is obtained by phase-locking the trigger level-1 signal (Sec. 3.3) to a replica of the RF frequency.

The clock period is $4 \times T_{RF} = 10.86$ ns. The time measured by the TDC is then related to the time of flight of the particle from the event origin to the calorimeter, T_{TOF}, by the formula:

$$T_{TDC} = T_{TOF} + \delta_C - N_{BC} T_{RF} \tag{3.11}$$

where δ_C is a single number accounting for the overall electronic offset and cable delay, and N_{BC} is the number of bunch-crossings needed to generate the start to the TDC (see Fig. 3.12).

The values of δ_C and T_{RF} are determined for each data taking run with $e^+e^- \rightarrow \gamma\gamma$ events. For such events, we look at the distribution of $\Delta_{TOF} = T_{clu} - R_{clu}/c$, where R_{clu} is the γ cluster position and T_{clu} is the γ cluster time reconstructed by the cluster algorithm applied to the T_{TDC} (see Sec. 3.2.1): well separated peaks correspond to different values of N_{BC} for events in the sample (see Fig. 3.13). δ_C is arbitrarily defined as the position of the peak with the largest statistics, and T_{RF} is determined from the peaks time separation. Both quantities are evaluated with a precision of $\sim$4 ps in a run of 200 nb^{-1} of integrated luminosity.

During offline processing, to allow the cluster times T_{clu} to correspond to particle times of flight T_{TOF}, a time offset $t_{0,\,evt} \equiv \delta_C - N_{BC} T_{RF}$ has to be subtracted from all cluster times (see Eq. 3.11). The time needed for the first level trigger formation,

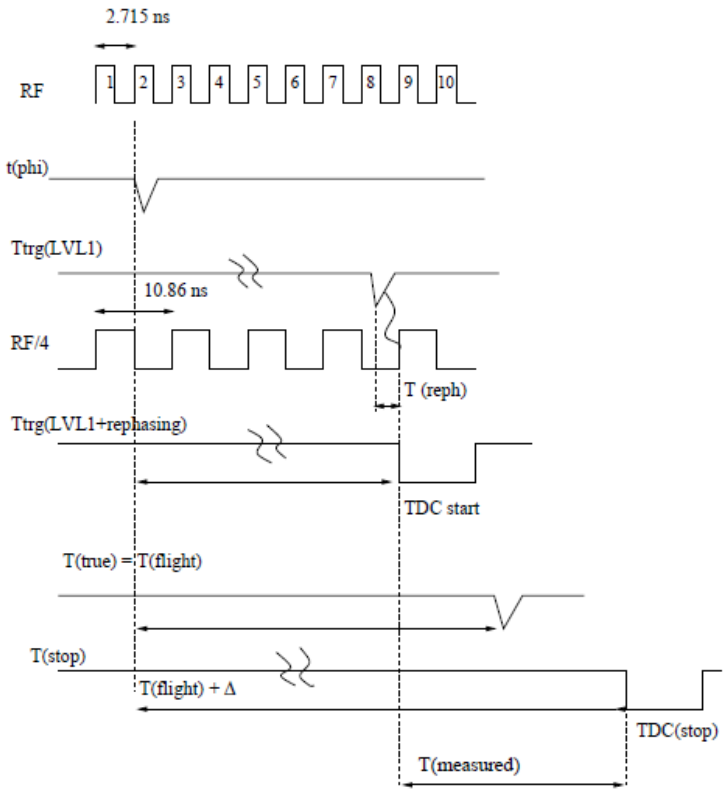

Figure 3.12: Timing scheme for bunch-crossing signal, calorimeter signals, and level-1 trigger formation.

$N_{BC}T_{RF}$, varies on an event by event basis; it is determined offline at different points of the reconstruction path. A value for N_{BC} at zero-th order (and thus $t_{0,\,evt}$) for all analyses is evaluated by assuming that the earliest cluster in the event is due to a prompt photon coming from the interaction point: by imposing $T_{TOF} = R_{clu}/c$ for this cluster, one gets the event-start time, $t_{0,\,evt}$:

$$t_{0,\,evt} = \delta_C - Int\left[\frac{R_{clu}/c - T_{clu} + \delta_C}{T_{RF}}\right] T_{RF}, \tag{3.12}$$

where $Int\,[\,]$ means the nearest integer to the quantity in square brackets.

The accidental coincidence of machine-background events with the beam collision can produce soft clusters that arrive earlier than the fastest cluster from the collision event itself. To increase the reliability of the estimate of $t_{0,\,evt}$, the cluster used for its evaluation must also satisfy the condition $E_{clu} > 50$ MeV.

Further corrections are analysis dependent (see Sec. 4.2.1).

3.6.2 Track-to-cluster association algorithm

The track-to-cluster association module finds correspondences between tracks in the drift chamber and clusters in the calorimeter.

The first step is to combine reconstructed tracks and vertices into decay chains. Then, only the tracks at the ends of these chains are considered and extrapolated

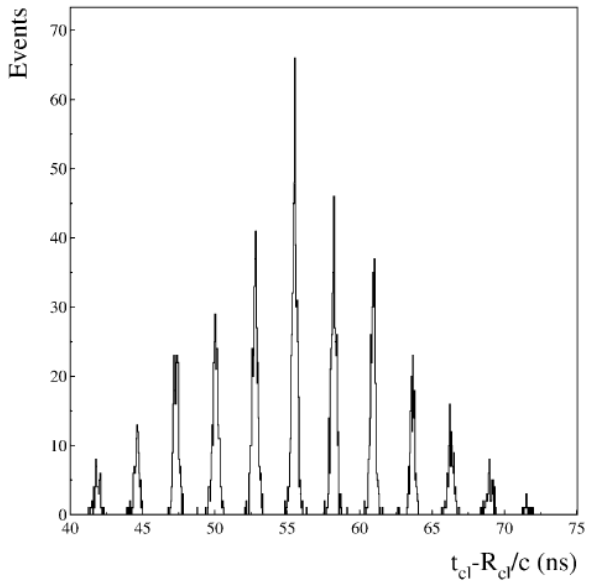

Figure 3.13: $\Delta_{TOF} = T_{clu} - R_{clu}/c$ distribution for 2γ events. Peaks are separated by $T_{RF} = 2.715$ ns.

to the calorimeter by using the measured momentum and the position of the last hit in the drift chamber. The track length L_{ext} from the last hit in the DC to the calorimeter surface, the momentum $\vec{p}_{ext}$ and the position $\vec{x}_{ext}$ of the particle at the calorimeter surface are evaluated from the extrapolation. The impact point $\vec{x}_{ext}$ so obtained is then compared with the position $\vec{R}_{clu}$ of the reconstructed calorimeter cluster centroid. A track is associated to a cluster if the distance between the impact point and the cluster centroid in the plane orthogonal to the direction of incidence of the particle on the calorimeter, $d^{\perp}_{TCA}$, satisfies:

$$d^{\perp}_{TCA} = \left| \frac{\left(\vec{R}_{clu} - \vec{x}_{ext}\right) \times \vec{p}_{ext}}{|\vec{p}_{ext}|} \right| < 30 \text{ cm}. \tag{3.13}$$

Clusters are assigned either to charged or to neutral particles by event classification algorithms if they respectively have or not have associated tracks by the track-to-cluster association module.

3.6.3 Event classification

The main classification algorithms include different modules for the identification of the following major physics channels at DAΦNE:

- generic background, identified using calorimeter clustering and DC hit counting, and rejected before DC reconstruction:
  - beam background;
  - cosmic-ray muons, vetoed from the trigger system that uses dedicated thresholds on the energy deposition in the outermost layer of the calorimeter,

- fragments of small-angle Bhabhas, identified by the presence of spatially concentrated clusters on the endcap calorimeters that arrive within a narrow time window;

- large-angle Bhabhas and $e^+e^- \to \gamma\gamma$ events, selected to calibrate the calorimeter and to evaluate the luminosity. These events are identified using only calorimetric information;

- tagged K_L or K_S decays (see next Sec. 4.2);

- tagged K^+ or K^- decays;

- $\phi \to \pi^+\pi^-\pi^0$ decays, obtained by searching for a vertex near the IP ($R_{xy} < 8$ cm, $|z| < 15$ cm) with two connected tracks of opposite charge, by cutting on the missing momentum and energy;

- $\pi^+\pi^- + n\gamma$ and fully neutral $n\gamma$ final states coming from various primary processes such as $e^+e^- \to \pi^+\pi^-\gamma$, $e^+e^- \to \phi \to \eta\gamma$ or $\eta'\gamma$, $e^+e^- \to \phi \to f_0(980)\gamma$ or $a_0(980)\gamma$, etc.

3.7 Monte Carlo simulation

The KLOE Monte Carlo simulation program, GEANFI, is based on GEANT 3.21 [36, 37] libraries, often used for high energy physics or astrophysics experiments.

All relevant machine parameters like $\sqrt{s}$ and $\vec{p}_\phi$ are entered in the Monte Carlo simulation run-by-run. In particular, the machine background has occurred with significant variations in different running periods, so it has been added to GEANFI using an offline procedure to select accidental DC and calorimeter hits on data, for each run.

GEANFI includes also an accurate description of the KLOE detector, which includes:

- the interaction region: beam line, low β quadrupoles and QCAL;

- the drift chamber;

- the calorimeter (barrel and endcaps);

- the magnetic field.

Moreover, a set of dedicated routines has been built to simulate each sub-detector response, starting by the fundamental informations got from particle tracking and association to energy-releases routines. Hadronic interactions are simulated using the GHEISHA hadronic showers generator. It has been necessary to carry out a dedicated simulation, since the hadronic showers package in the GEANT3, FLUKA libraries doesn't simulate the hadronic interactions in the energy range interested by KLOE. The hadronic cross sections for low energy kaons, and especially for $K_L \to K_S$, $K_S \to K_L$ regeneration processes, have been modified with respect to the original GHEISHA library, and have been included in the code GEANFILASTDB.

Chapter 4

Data Sample and K_L tag

Most KLOE data were taken during two running periods. The 2001-2002 run yielded 450 pb^{-1} of data, corresponding to approximately 140 million tagged K_S decays, 230 million tagged K_L decays, and 340 million tagged $K^{\pm}$ decays. KLOE also took data in 2004-2005, after completion of a number of DAΦNE modifications intended to increase the luminosity. About 2 fb^{-1} were collected, giving a fivefold increase in statistics. In total, KLOE has collected during the years 1999-2005 $\sim$2.5 fb^{-1} luminosity (see Fig. 4.1).

4.1 Data sample for the K_L lifetime

All data set collected by KLOE in 2005 has been used in this analysis, it corresponding to an integrated luminosity of $\sim$1.2 fb^{-1}. A single run corresponds to an integrated luminosity of $\sim$200 nb^{-1}, collected in about one hour of data taking. First, runs are divided in periods with approximately the same value of $\sqrt{s}$. When a single run with $\sqrt{s}$ completely different from other runs is found, it is rejected.

Cuts on integrated luminosity are applied for each run period. Only periods with more than $\sim$200 nb^{-1} are retained. Each data run collected has been simulated with the KLOE standard Monte Carlo with a well-defined production procedure.

Moreover, a set of requests on the kinematics of e^+e^--system in the initial state are applied for each run period:

- the average value of y and z components of ϕ total momentum (evaluated using Bhabha scattering events on a run-by-run basis) must satisfy:

$$\left|p_\phi^y\right| < 3 \text{ MeV}, \qquad \left|p_\phi^z\right| < 3 \text{ MeV}, \tag{4.1}$$

  where $\vec{p}_\phi = p_\phi^x\,\hat{i} + p_\phi^y\,\hat{j} + p_\phi^z\,\hat{k}$ is the ϕ total momentum and $\hat{i}$, $\hat{j}$ and $\hat{k}$ are the unit vectors respectively along the x, y and z axes as defined in the end of Chap. 2;

- the average total energy in the center of mass must satisfy:

$$\left|\sqrt{s} - M_\phi\right| < 5 \text{ MeV}; \tag{4.2}$$

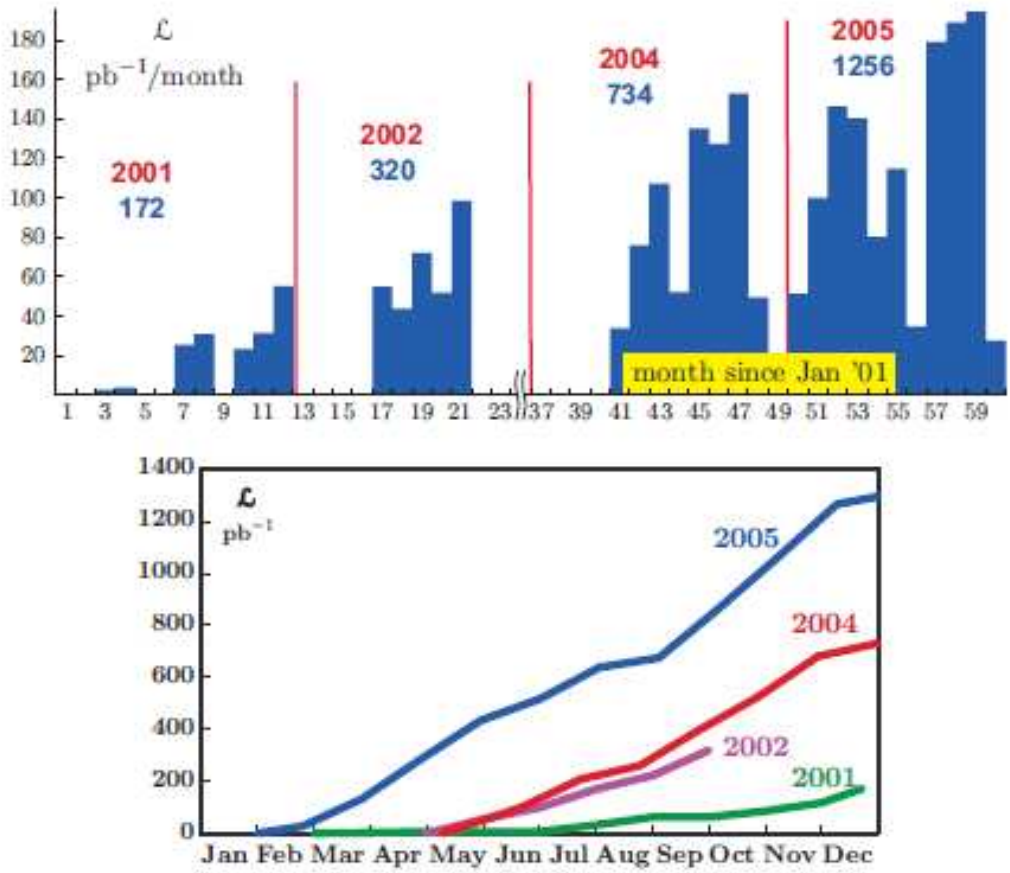

Figure 4.1: Integrated luminosity since January 2001: by month (**top**) and by year (**bottom**).

- the average position of the beam crossing point must satisfy:

$$|x| < 3 \text{ cm}, \qquad |y| < 3 \text{ cm}, \qquad |z| < 5 \text{ cm}; \tag{4.3}$$

- the spread in the beam interaction region must satisfy:

$$\sigma_x < 3 \text{ cm}, \qquad \sigma_z < 3 \text{ cm}. \tag{4.4}$$

All these values have been obtained from standard deviations of Gaussian fits.

Each run used in this analysis has been simulated with Monte Carlo GEANFI (see Sec. 3.7): the number of simulated events for each run is the same expected number evaluated from run luminosity. A Monte Carlo set is used to simulate ϕ decays in this analysis, according to respective branching ratios. Initial- and final-state radiation are also included in the simulation. This Monte Carlo set has been used both for signal and background samples of this analysis.

All relevant machine parameters like $\sqrt{s}$ and $\vec{p}_\phi$ are entered in the Monte Carlo simulation run-by-run. In particular, the machine background at DAΦNE has occurred with significant variations in different running periods, so it has been added

to GEANFI using an offline procedure to select accidental DC and calorimeter hits on data, for each run.

Data runs collected in 2005 [40] have been divided in 10 close run periods with a quite stable value of $\sqrt{s}$ around the nominal value $\sqrt{s} = M_\phi = 1019.5$ MeV, since collider running conditions and $\sqrt{s}$ during the years were subject to frequent changes, and $\sqrt{s}$ as well, with a fluctuaction of ∼0.06% (∼0.6 MeV) around the nominal value. Fig. 4.2 shows the run periods division.

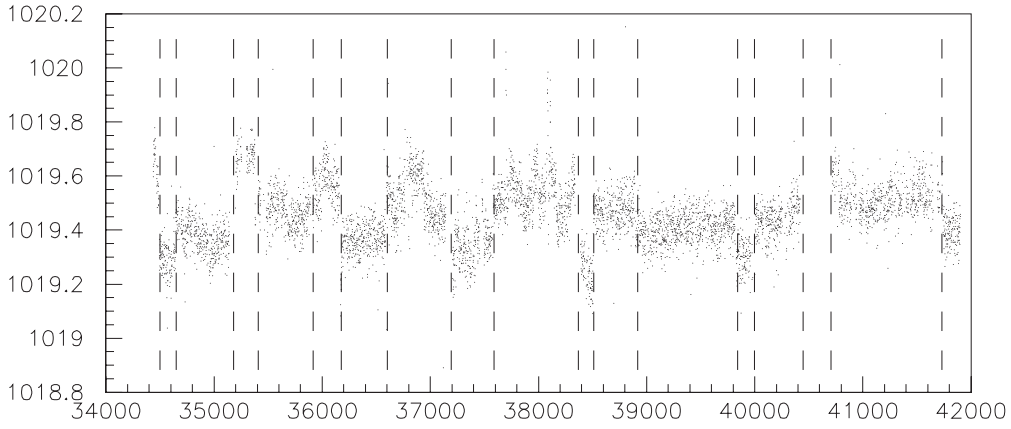

Figure 4.2: Data sample collected in 2005: $\sqrt{s}$ vs. run number N.

The K_L lifetime measurement in this thesis has been evaluated with ∼1.2 fb^{-1} data sample collected by KLOE in 2005.

4.2 The K_L tag

$\phi \to K^0\overline{K}^0$ decay occurs ∼34.2% of the times. The neutral kaon pair is a pure $J^{PC} = 1^{--}$ state, therefore the initial two-kaon state can be written, in the ϕ-rest frame, as:

$$\begin{aligned} |K\bar{K}, t = 0\rangle &= (|K^0, \vec{p}\rangle|\overline{K}^0, -\vec{p}\rangle - |\overline{K}^0, \vec{p}\rangle|K^0, -\vec{p}\rangle)/\sqrt{2} = \\ &= (|K_S, \vec{p}\rangle|K_L, -\vec{p}\rangle - |K_L, \vec{p}\rangle|K_S, -\vec{p}\rangle)/\sqrt{2}. \end{aligned} \tag{4.5}$$

Detection of a K_S (K_L) thus signals (*tags*) the presence of a K_L (K_S) on the opposite side of the detector, and the same applies to K^+ and K^- mesons. DAΦNE provides pure K_S and K_L beams of precisely known momenta (event by event).

Candidate K_L mesons are identified by the presence of a $K_S \to \pi^+\pi^-$ decay ($BR \sim 69.2\%$), by requiring these conditions:

- a vertex with two tracks of opposite curvature with origin within a cylindrical fiducial volume [1] of radius $r < 10$ cm and length $|z| < 20$ cm, centered on the collision region, as determined for each run using Bhabha events;

[1] The beam pipe sphere radius corresponds to more than 15 K_S lifetimes.

- the two-track invariant mass, calculated assuming the pion mass for both tracks, must be within 15 MeV of the neutral kaon mass;

- the magnitude of the total momentum of the two tracks must be within 10 MeV of the value expected from two-body ϕ decay kinematics and the value of $\vec{p}_\phi$.

If more than one vertex satisfies these criteria, that closest to the nominal ϕ vertex position is identified as the K_S decay vertex. The efficiency for finding $K_S \to \pi^+\pi^-$ decays is ∼68%.

A K_L could be wrongly identified as a K_S if it decays near the IP. In this case, either a particle that decays near the IP (anyway outside our fiducial volume) will be found on the other side of the detector (expected to be the tagged K_L), or a "fake" K_S vertex is reconstructed, due to tracking interference between the K_S and K_L charged decay products: a wrong K_L line of flight will be evaluated.

The best estimate of the magnitude of the K_S momentum, p_{K_S}, is obtained from the kinematics of the $\phi \to K_S K_L$ decay, using the K_S direction reconstructed from the measured momenta of the $\pi^+\pi^-$ tracks and the known value of $\vec{p}_\phi$. The central value of the K_S momentum depends on the kaon mass.

The resolution on the K_S momentum obtained with this method is dominated by the beam-energy spread. The value of p_{K_S} is very sensitive to the value of the kaon mass:

$$\frac{dp_K}{p_K} = \frac{1}{\beta^2}\frac{dE}{E} + \frac{dM_K}{M_K} \tag{4.6}$$

where β is the kaon velocity. For this reason, the KLOE measurement [41] for the value of the K_S mass has been used.

The position of the ϕ production point, $\vec{x}_\phi$, is determined as the point of closest approach of the K_S momentum, propagated backwards from the K_S vertex, to the beam line. The K_L line of flight is then constructed from the K_L momentum, $\vec{p}_{K_L} = \vec{p}_\phi - \vec{p}_{K_S}$, and the position of the production vertex, $\vec{x}_\phi$.

Successful calculation of $\vec{p}_{K_L}$ is the minimal requirement for a K_L tag. Additional informations can be obtained using the K_L tag: the event $t_{0,\,evt}$ starting time (see Sec. 4.2.1) and whether or not the clusters from the K_S unambiguously satisfy the calorimeter trigger.

To determine the event $t_{0,\,evt}$, each of the tracks from the K_S vertex are extrapolated to the calorimeter.

In this analysis, two track-cluster residuals are defined for the purposes of track-to-cluster association: d_{TCA}, the distance from the extrapolated impact point on the calorimeter to the cluster centroid; and $d^{\perp}_{TCA}$, the component of this distance in the plane transverse to the momentum of the track at impact.

4.2.1 Determination of the event $t_{0,\,evt}$

As a result of the DAΦNE bunch-crossing period, which is short relative to the trigger-formation time, the experiment cannot be triggered with every bunch crossing. The level-1 trigger is rephased with the bunch-crossing time, and the bunch crossing which originated a given event is determined offline [33, 39].

As explained in Sec. 3.6.1, the starting event time $t_{0,\,evt}$, or, equivalently, the number of bunch crossing N_{BC} necessary to start the trigger, is determined offline. Before tracking procedure and event classification, N_{BC} can be evaluated by supposing that the first event cluster is due to a photon that arises from the interaction point. This first determination allows to reconstruct and classify the event as a physical mode. Nevertheless, many decays modes produced at DAΦNE, including $K_L \to \pi^0\pi^0\pi^0$ here analyzed, does not carry "prompt" photons in the final state, therefore the $t_{0,\,evt}$ corrected cluster times, $T^{(0)}_{clu}$, can be different from effective time of flight for an integer number of bunch crossing ΔN_{BC}:

$$T^{(0)}_{clu} = T_{TOF} - \Delta N_{BC} T_{RF} \tag{4.7}$$

The correction $\Delta N_{BC} T_{RF}$ can be obtained by using events with topology that could easily be associated to a track; it can be determined by evaluating:

$$\Delta N_{BC} T_{RF} = \frac{L}{\beta c} - T^{(0)}_{clu} \tag{4.8}$$

where L is the path length traveled by the particle to which the selected cluster is associated, and β is the particle velocity.

For this analysis, the event $t_{0,\,evt}$ is determined using the tracks from the K_S. Clusters with $d^{\perp}_{TCA} < 30$ cm about the extrapolation of each track are first considered, and only clusters with E $>$ 100 MeV are retained. If there is more than one candidate, the cluster nearest to the track is used, *i.e.*, that for which $d^{\perp}_{TCA}$ is smallest.

If a cluster is successfully associated to the track, the difference between the measured time of flight and that predicted on the basis of path-length and momentum measurements is used to estimate the event $t_{0,\,evt}$:

$$\Delta_{TOF} = T_{clu} - \left[\frac{L_{K_S}}{\beta_{K_S} c} + \frac{L_\pi}{\beta_\pi c} + \delta t_{int} \right], \tag{4.9}$$

where L_{K_S} is the distance between the K_S vertex and the ϕ vertex calculated for the event ($\vec{x}_\phi$), β_{K_S} is calculated from the magnitude of the tagging momentum, L_π refers to the entire path length of the extrapolated pion track, including the reverse extrapolation to the K_S vertex and the forward extrapolation to the calorimeter, as well as the length of the pion track itself, and δt_{int} is a tunable parameter of the order of 400 ps which is intended to take into account the mean residual between calorimeter-impact and cluster-centroid times.

From each value of Δ_{TOF}, an estimate of the event $t_{0,\,evt}$ is obtained in the usual way, *i.e.*, by first calculating the trigger time, $t_{trig} \equiv N_{BC} T_{RF}$, as:

$$t_{trig} \equiv T_{exp} + \delta_C - T^{(0)}_{clu} = \delta_C - \Delta_{TOF}, \tag{4.10}$$

where δ_C is a single number accounting for the overall electronic offset and cable delay; the event $t_{0,\,evt}$ ($t_{0,\,evt} \equiv \delta_C - N_{BC}\, T_{RF}$) is obtained once δ_C is subtracted.

Once a good estimate of the event $t_{0,\,evt}$ has been obtained, all cluster times are adjusted accordingly.

4.2.2 Dependence of the tagging efficiency with L_K

$K_L \to \pi^0\pi^0\pi^0$ events are tagged by $K_S \to \pi^+\pi^-$ events which satisfy the requirements described in Sec. 4.2. The tagging efficiency has been evaluated by Monte Carlo as a function of L_K (K_L decay vertex position) for the dominant K_L decay channels. For a K_L decaying in a given channel at a given L_K, the tagging efficiency is defined as:

$$\varepsilon(tag, K_L \to i, L_K) = \frac{N(tag, K_L \to i, L_K)}{N(K_L \to i, L_K)} \tag{4.11}$$

where $N(tag, K_L \to i, L_K)$ is the number of $K_L \to i$ decay mode events retained after the tagging procedure, and $N(K_L \to i, L_K)$ is the total number of $K_L \to i$ decay mode events. The results are shown in Fig. 4.3.

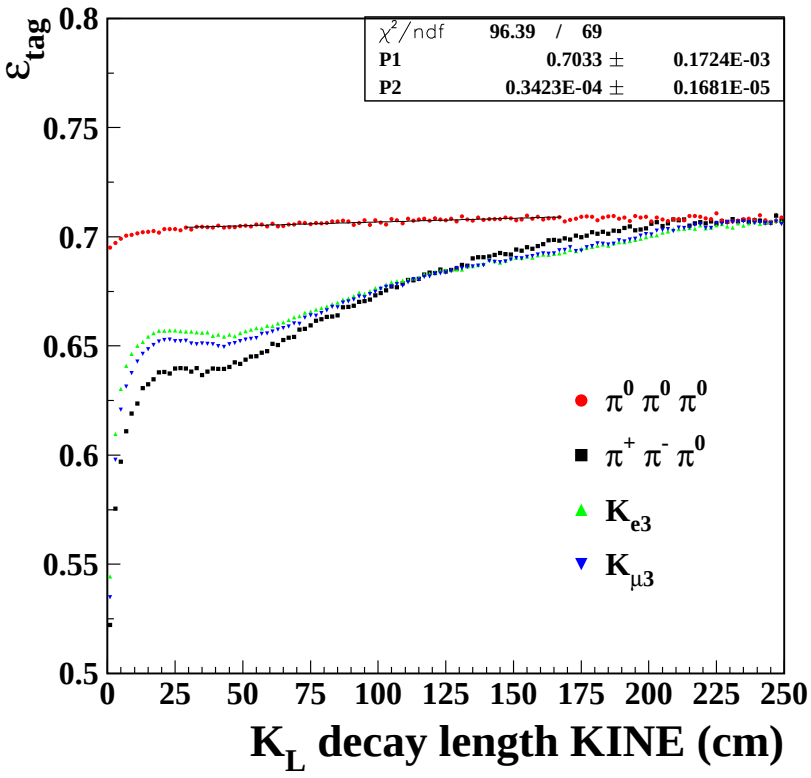

Figure 4.3: Tagging efficiency as a function of L_K for main K_L decay modes.

The difference in tagging efficiency among the modes is mainly due to the dependence of the trigger efficiency on the K_L behaviour (Ref. [42]). Only the calorimeter trigger (Ref. [35]), which requires two local energy deposits above some threshold, is used for the present analysis (see Sec. 3.3).

The reconstructed transverse radius distributions of the K_L vertex with very loose tagging requests have been studied on 2001-02 data sample (Ref. [42]). They show a very good data - Monte Carlo agreement in the fiducial volume for charged K_L decays and $K_L \to \pi^0\pi^0\pi^0$ decay, respectively shown in fig. 4.4 left and right. The slight disagreement in the first bins of the spectrum in the charged decays has been further investigated in the quoted reference, to understand tracking inefficiencies,

while the good agreement in the $K_L \to \pi^0\pi^0\pi^0$ decay allows us to consider the data tagging efficiency well reproduced by the Monte Carlo.

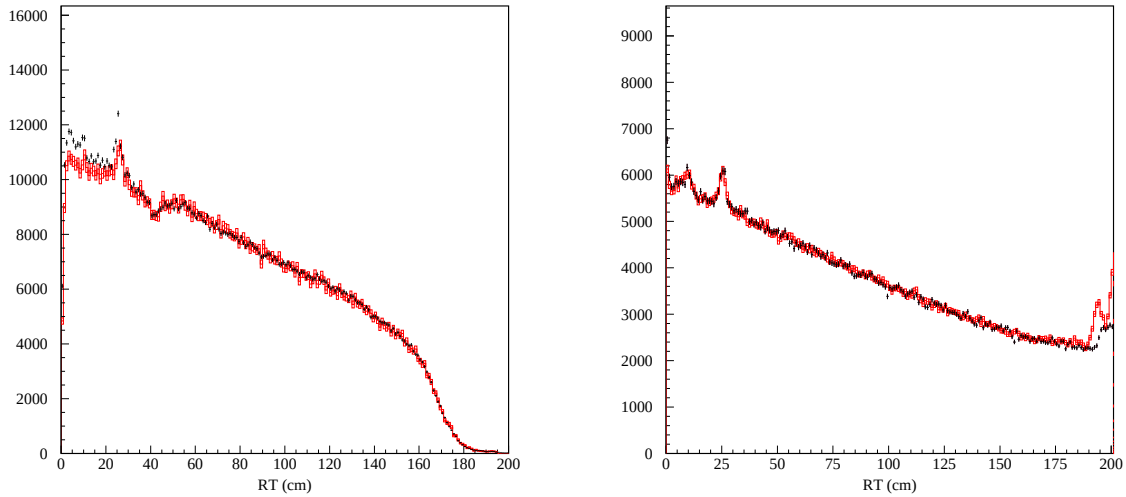

Figure 4.4: Reconstructed R_T distributions for K_L decays to charged particles (**left**) and $3\pi^0$ (**right**), for data (black) and Monte Carlo (red), plots from Ref. [42].

The trigger efficiency is, on average, ∼100 % for $K_L \to \pi^0\pi^0\pi^0$ and between 85 - 95% for charged K_L decays. The trigger efficiency also depends on the position of the K_L decay vertex due to the use of position-dependent trigger thresholds. Another contribution is the dependence of the reconstruction efficiency for the pion tracks from $K_S \to \pi^+\pi^-$ on the presence of other tracks in the drift chamber. This contribution depends on the position of the K_L decay point and affects mainly events with $K_L \to$ charged particles near to the IP. The tagging efficiency (Fig. 4.3) has been evaluated on generated events, so it includes the trigger efficiency. It has a linear dependence with L_K for the $K_L \to \pi^0\pi^0\pi^0$ channel, with a slope almost compatible with zero, $b = (3.42 \pm 0.17) \times 10^{-5}$/cm, and an intercept $a = (70.333 \pm 0.017)\%$.

4.2.3 The fiducial volume

The fiducial volume, FV, used for the analysis lies completely within the drift chamber and is defined by both the conditions:

$$FV : \begin{cases} 35 < R_T < 150 \text{ cm} \\ |z| < 120 \text{ cm} \end{cases} \tag{4.12}$$

where

$$R_T = \sqrt{x^2 + y^2} \tag{4.13}$$

and (x, y, z) are the coordinates of the K_L decay vertex position. Since the mean K_L decay length in KLOE is 340 cm, the FV contains ∼26.1% of the K_L decays. This choice minimizes the difference in tag bias among decay modes.

4.2.4 The Calorimeter regions

The calorimeter has been divided into three different regions:

- **BA**: the *barrel*, $R_T < 200\,cm$ and $|z| < 150\,cm$;
- **EC**: the *endcaps*, $25\,cm < R_T < 175\,cm$ and $|z| > 170\,cm$;
- **OV**: the *barrel-endcap overlap* region, $R_T > 200\,cm$ and $|z| > 150\,cm$, or $R_T > 175\,cm$ and $|z| > 170\,cm$.

Chapter 5

Data analysis

5.1 Introduction

The K_L lifetime has been measured using the decay channel $K_L \to \pi^0\pi^0\pi^0$. The choice of the fully neutral decay is intended to minimize the superposition with the $K_S \to \pi^+\pi^-$decay products. In fact, the tagging efficiency is almost independent of the K_L decay length as shown in Fig. 4.3 thus minimizing the systematic error of the efficiency.

This analysis makes use of $\sim$1.2 fb^{-1} data sample taken in 2005. The data set has been divided in periods having approximately the same value of $\sqrt{s}$.

The branching ratio of $\phi \to K_S K_L$ is $\sim$34%. The signal of K_L meson production is given by the observation of the $K_S \to \pi^+\pi^-$ decay (see Sec. 4.2).

As mentioned in the thesis introduction, this measurement has been already performed by KLOE in 2005 (Ref. [2]), but also if the technique of the measurement presented in this thesis is similar, there are many differences between the two:

- the bunch crossing period has been lowered from 5.43 to 2.715 ns; this adjustment yielded an increase of machine background, and a finer analysis was needed to cope with the latter;
- the tagging requests are slightly different: stronger cuts have been applied to preserve data quality, due to the short bunch crossing period;
- the time calibration and the neutral vertex spatial resolution have been studied for each run period;
- the single-photon neutral vertex reconstruction efficiencies as a function of the K_L vertex position and the photon energy have been measured on data and applied on the Monte Carlo with a hit or miss method;
- the machine background measured in data has been included run-by-run in the Monte Carlo program;
- the background rejection selections are different;
- the fit technique is much different: while in the previous measurement the data proper time distribution was efficiency corrected and background subtracted

bin-by-bin, in this analysis we do not modify the data distribution while both efficiency and background are included in the fit function;

- the systematic errors are completely uncorrelated, with the exception of the systematics due to the nuclear interactions.

From now on, the expressions "*charged vertex*" and "*neutral vertex*" will be used respectively for a vertex reconstruction obtained by using tracks (drift chamber information) and clusters not-associated-to-tracks (calorimeter information), like explained in Sec. 3.6.2.

The two pions from $K_S \to \pi^+\pi^-$ decay determine the K_S direction in the ϕ rest frame: the $K_L \to \pi^0\pi^0\pi^0$ neutral vertex is reconstructed along the opposite direction using the calorimeter information, which provides the spatial coordinates, energies and time of the photons.

The tagging $K_S \to \pi^+\pi^-$ decays must satisfy the following requests:

1. there must be two opposite curvature tracks originating from a point C inside a cylinder, centered at the IP (interaction point, see Chap. 3), of 10 cm radius and $|z| < 20$ cm;

2. the K_S momentum in the ϕ rest frame must satisfy $100 < p(K_S) < 120$ MeV/c;

3. the dipion invariant mass, $M(\pi\pi)$, has to lie in the interval

$$482.6 < M(\pi\pi) < 512.6 \text{ MeV}/c^2; \tag{5.1}$$

4. at least one of the two tracks has to be associated to a calorimeter cluster of E $\geq$ 100 MeV, to evaluate the event $t_{0,\,evt}$ (see Sec. 4.2).

The efficiency for finding $K_S \to \pi^+\pi^-$ decays is $\sim$68%.

The previous KLOE lifetime measurement made use of the same tagging requests at items n.1 and 2, while the dipion invariant mass cut in the item n.3 was tighter ($\pm$5 MeV) and the energy threshold in the item n.4 was lower (E $\geq$ 50 MeV).

The event $t_{0,\,evt}$ for $K_S \to \pi^+\pi^-$ decays is evaluated using the pion arrival time on the calorimeter, the pion track length reconstructed by the DC, and its velocity (see Sec. 4.2.1).

The $t_{0,\,evt}$ evaluation is used to correct all particles arrival times measured by the calorimeter. The accuracy of this procedure is tested using the control sample of $K_L \to \pi^+\pi^-\pi^0$ decays as explained in the following. The correct event bunch crossing time assignment implies to satisfy the condition:

$$T_{clu} = \frac{L_K}{\beta c} + \frac{L_\gamma}{c}, \tag{5.2}$$

where T_{clu} is the arrival time on the calorimeter of one of the two photons from π^0 decay, L_K and β are the decay length and the velocity of the K_L, L_γ is the photon path length and c the speed of light. L_K is evaluated using the charged vertex given by $\pi^+\pi^-$, while L_γ is the distance between the K_L charged vertex and the cluster centroid. The $(T_{clu} - L_K/\beta c - L_\gamma/c)$ distribution for $K_L \to \pi^+\pi^-\pi^0$ control sample is shown in Fig. 5.1: when a correct bunch crossing is assigned to the event, a peak

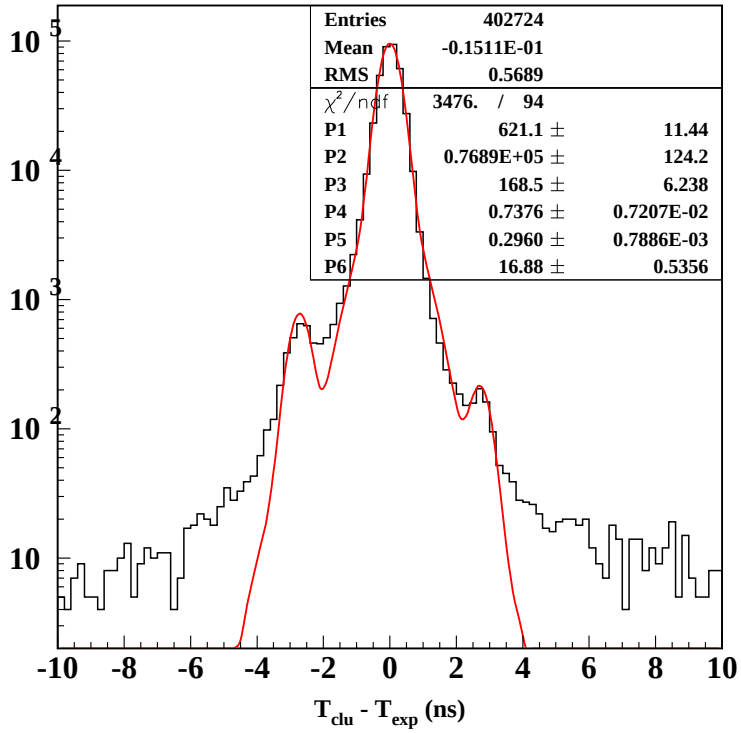

Figure 5.1: $T_{clu} - L_K/\beta c - L_\gamma/c$ distribution of one photon from π^0 decay from $K_L \to \pi^+\pi^-\pi^0$ decay after the $t_{0,\,evt}$ correction: two visible peaks at $\pm$ 2.715 ns arise from events with uncorrect bunch crossing identification.

centered at zero is expected, while when the bunch crossing identification is wrong, peaks centered at multiple values of the bunch crossing period 2.715 ns are expected (further tails in the distribution). An approximate fit (a sum of three gaussians has been used) to the distribution $(T_{clu} - L_K/\beta c - L_\gamma/c)$ obtained by our tagging request yields an uncorrect bunch crossing identification rate of $\sim$1%.

The K_L momentum, $\vec{p}_{K_L} = \vec{p}_\phi - \vec{p}_{K_S}$ (see Sec. 4.2), has been measured using the K_S momentum (measured event-by-event from $\pi^+\pi^-$ tracks) and ϕ momentum (evaluated run-by-run using Bhabha events). The precision in the determination of the K_L line of flight is once again evaluated using the control sample $K_L \to \pi^+\pi^-\pi^0$, measuring the angle between $\vec{p}_{K_L}$ and the line joining the ϕ production point and the K_L decay vertex, resulting in an angular resolution of $\sigma_\phi = 1.5^\circ$ for the azimuthal and $\sigma_\theta = 1.8^\circ$ for the polar angle, respectively.

The main feature of the $K_L \to \pi^0\pi^0\pi^0$ decay is to have a large number of photons. In order to minimize the effects due to the cluster reconstruction efficiency and the acceptance corrections, almost all configuration of clusters are retained for the analysis. K_L events have been selected with at least three calorimeter clusters not associated to any track (see Sec. 3.6.2) with a minimum energy $E_{thr} = 20$ MeV. The threshold is chosen to reject low energy clusters produced mainly from machine background. The residual background contamination is studied in Chap. 6. The reconstruction efficiency has been evaluated from Monte Carlo: $\varepsilon = (99.2 \pm 0.1\%)$.

In order to reduce the contamination of $K_L \to K_S \to \pi^0\pi^0$ regeneration in

the inner wall and in the external plates of the drift chamber, and the efficiency loss due to the QCALs (see Fig. 3.8), a cut on the K_L polar angle is applied: $40^\circ < \theta_{K_L} < 140^\circ$. Since the angular distribution of $K_S K_L$ from a ϕ decay is $dN/d\cos\theta \propto \sin^2\theta$, the fraction of K_L in this angular range is large: 92.5%.

5.2 The neutral vertex

The position of the K_L decay vertex is measured using the K_L line of flight and the positions and the arrival times of the photons measured by the calorimeter [39]. For each photon there is an independent determination of the neutral vertex position of the K_L, by solving the Eqs. (5.3),

$$\begin{cases} L^2 + L_K^2 - 2LL_K\cos\theta &= L_\gamma^2 \\ \frac{L_K}{\beta c} + \frac{L_\gamma}{c} &= T_{clu} \end{cases} \tag{5.3}$$

where, as shown in Fig. 5.2, L is the distance between the interaction point and the cluster centroid, L_γ is the distance between the K_L decay vertex and the calorimeter cluster centroid, T_{clu} is the measured arrival time of the photon and β is the velocity of the K_L evaluated from the K_L tag procedure.

Each photon defines a triangle IDA, see Fig. 5.2. I is the interaction point, D the K_L decay point, A the photon entry point in the calorimeter, $\overline{\mathrm{ID}}$ is L_K and $\overline{\mathrm{DA}}$ is L_γ. From the known positions of I and A, the $\widehat{\mathrm{AID}} = \theta$ angle and the time spent by the kaon and the photon to cover the path IDA, we find the length of $\overline{\mathrm{ID}}$. There are two solutions. One of them corresponds to D being along the K_S path and is rejected.

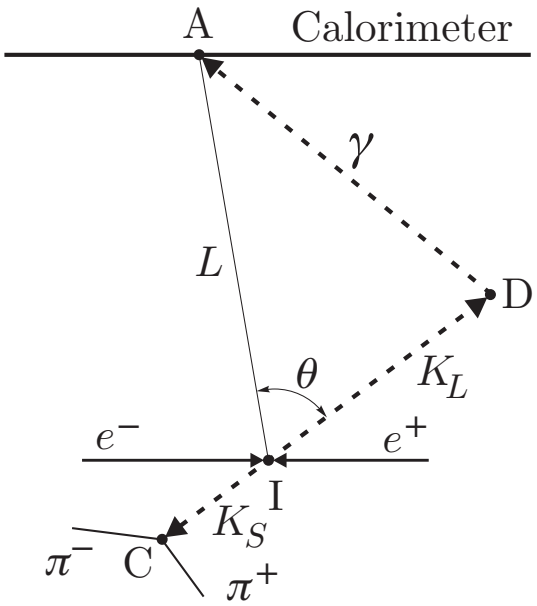

Figure 5.2: Single photon geometry.

Tab. 5.1 shows a summary of the main variables used in this analysis.

L_γ	photon path length ($\overline{\mathrm{DA}}$)
L_K	K_L decay length ($\overline{\mathrm{ID}}$)
L_K^{ch}	K_L decay length evaluated with the $K_L \to \pi^+\pi^-\pi^0$ charged vertex
R_T	transverse radius of the K_L decay vertex position
β	K_L velocity given by the tag
T_{clu}	measured photon cluster time in the EMC
E_{clu}	measured photon cluster energy in the EMC
R_{clu}	measured photon cluster position in the EMC
t_{exp}	expected arrival time of the photon on the EMC given by kinematics
R_{γ_i}	K_L neutral vertex position evaluated with the i-th photon
σ_{γ_i}	spatial resolution on the K_L neutral vertex position evaluated with the i-th photon

Table 5.1: Summary of the analysis variables.

The resolution on the vertex position as a function of the cluster energy goes as

$$\sigma_{R_\gamma}(E_{clu}) \sim \frac{a}{E_{clu}^{3/2}} \tag{5.4}$$

where R_γ is the K_L decay length evaluated by the neutral vertex, E_{clu} is the measured photon cluster energy and a is a parameter that will be extracted from a fit (see Sec. 5.3.1).

5.3 The control sample $K_L \to \pi^+\pi^-\pi^0$ analysis

The $K_L \to \pi^+\pi^-\pi^0$ events are used as a control sample to determine:

- the calorimeter time scale;
- the resolution of the K_L direction;
- the resolution of the neutral vertex position;
- the single-photon reconstruction efficiency as a function of the decay length.

5.3.1 Single-photon neutral vertex reconstruction quality

The single-photon neutral vertex reconstruction quality has been studied using $K_L \to \pi^+\pi^-\pi^0$ decays, by comparing the charged vertex position given by the $\pi^+\pi^-$ tracks with the neutral vertex position evaluated using photons arrival times from π^0 decay. After that, we derive

- the time scale corrections, to calibrate the K_L decay length measurements;
- the spatial resolution of the K_L decay length reconstruction.

Since the K_L lifetime is evaluated fitting the proper time distribution, directly related to decay length distribution, these corrections are fundamental for a precise measurement.

Selection of $K_L \to \pi^+\pi^-\pi^0$ events

The selection of $K_L \to \pi^+\pi^-\pi^0$ events is done without cutting on quantities related to the vertex position, to avoid any possible bias. Events with two charged tracks reconstructing a K_L decay vertex are selected. The missing momentum, the missing energy and the missing mass are evaluated:

$$\vec{p}_{miss} = \vec{p}_{K_L} - \vec{p}_1 - \vec{p}_2 \quad (5.5)$$

$$E_{miss} = E_{K_L} - E_1 - E_{2,} \quad (5.6)$$

$$M^2_{miss} = E^2_{miss} - |\vec{p}_{miss}|^2 \quad (5.7)$$

where $\vec{p}_{K_L}$ and E_{K_L} are respectively the momentum and the energy of the K_L meson, obtained from the reconstruction of the tagging $K_S \to \pi^+\pi^-$ decay; $\vec{p}_i$ and E_i are respectively the momentum of the positive and negative track (i=1,2) associated to the K_L line of flight and the energy of these particles in the charged pion mass hypothesis. $K_L \to \pi^+\pi^-\pi^0$ events are selected applying the cut:

$$|M_{miss} - M_{\pi^0}| < 4\,\mathrm{MeV} \quad (5.8)$$

which corresponds to about two standard deviations in the missing mass distribution. After these cuts, we searched for the two photon clusters from the π^0 decay. The sample used for the single-photon efficiency evaluation is selected requiring one photon cluster (the *tagging* photon) with a neutral vertex reconstructed within 5σ from the charged vertex.

Spatial calibration and resolution

For each event, the distance between the charged vertex and the single-photon neutral vertex has been evaluated (see Fig. 5.3 on the left side):

$$\Delta R \equiv L^{ch}_K - R_{\gamma_i} \quad (5.9)$$

being L^{ch}_K the K_L decay length evaluated using the charged pion tracks, and R_{γ_i} the distance between the ϕ decay point and the neutral vertex computed with the i-th photon. Fig. 5.4 on the left side shows the average value of ΔR as a function of R_T, the transverse radius of the K_L charged vertex (a variable strongly related to L_K) for the barrel region of the calorimeter (see definitions in Sec. 4.2.4). The charged vertex position has been used to perform the time calibration, in order to get a time independent measurement and to take advantage of the fine DC spatial resolution. The average value is not centered at zero as one would expect. To understand this trend, the comparison between measured times (used to evaluate R_{γ_i}) and expected times (estimated from decay kinematics) has been studied.

Calorimeter time scale calibration

It is necessary to calibrate the calorimeter time scale to study the spatial resolution of the single-photon neutral vertex reconstruction. The expected arrival time of the photon on the calorimeter is evaluated using the charged vertex information (still use of $K_L \to \pi^+\pi^-\pi^0$ decays):

$$t_{exp\ \gamma_i} = \frac{L^{ch}_K}{\beta c} + \frac{L_{\gamma_i}}{c}, \quad (5.10)$$

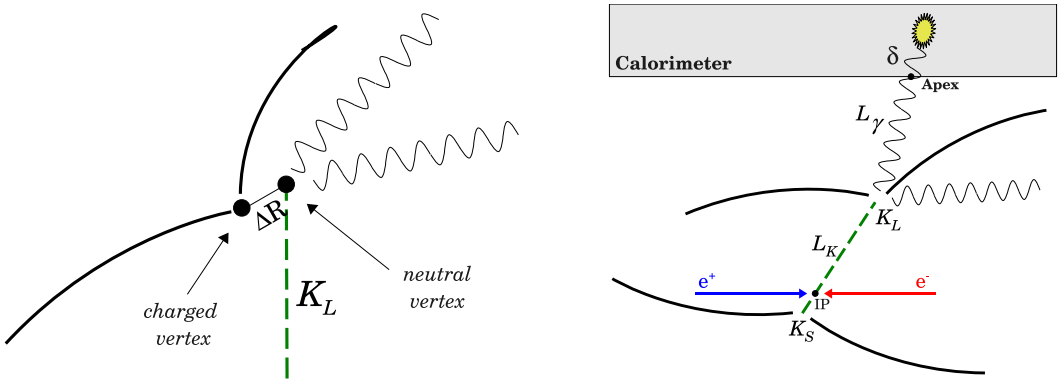

Figure 5.3: Scheme of the $K_L \to \pi^+\pi^-\pi^0$ geometry for the spatial resolution: ΔR distance between charged and single-photon neutral vertex (**left**) and depth δ and apex impact point (**right**).

where i=1,2 is the cluster index, L_{γ_i} is the distance between the charged vertex and the cluster centroid. The time difference between the measured and expected arrival time of each photon has been evaluated, in order to calibrate the time scale:

$$\Delta t_{\gamma_i} = T_{clu\ \gamma_i} - t_{exp\ \gamma_i}. \tag{5.11}$$

Fig. 5.4 on the right side shows the Δt_{γ_i} distribution as a function of the K_L decay length in the transverse plane. For each dot, the average value is obtained performing a gaussian fit of slices in R_T. The Δt_γ distribution is not flat and significantly far from zero compared with the errors, that take into account the charged and the neutral vertex uncertainties. The photon path and the propagation of the shower inside the calorimeter have been studied to reduce the difference between measured time by the calorimeter and expected time from kinematics. The photon is expected to travel along L_γ with velocity equal to c, therefore $t_{exp\ \gamma_i}$ has been evaluated in this hypothesis. Actually, photons travel with c velocity until the impact point (the so-called *apex*) on the calorimeter, then they produce a shower. Considering the path from *apex* to cluster centroid, one has to account for the shower propagation inside the calorimeter.

This effect has been parameterized with a fictitious photon velocity inside the calorimeter, β_γ^{calo}.

The *apex* is defined by the intersection between the photon line of flight and the calorimeter internal plane; it is evaluated using the charged vertex and the neutral vertex information for each region of the calorimeter (barrel, endcaps and the overlap region, see Sec. 4.2.4). The so-called *depth*, δ, is evaluated as the distance between the apex and the cluster centroid. So the expected time spent by the photon until the apex can be computed as:

$$t_{exp\ apex} = \frac{L_K}{\beta c} + \frac{L_{\gamma_{apex}}}{c} \tag{5.12}$$

where $L_{\gamma_{apex}}$ is the path traveled by the photon from the K_L charged vertex to the impact point on the calorimeter (apex), as sketched in Fig. 5.3 on the right side.

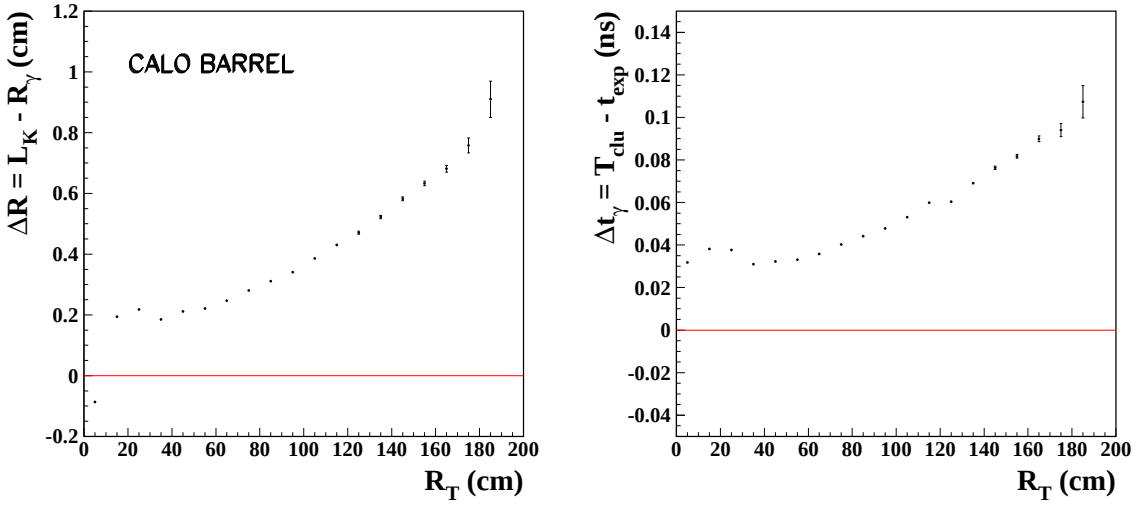

Figure 5.4: **Left**: average value of ΔR, the distance between the charged vertex and the single-photon neutral vertex as a function of R_T in the transverse plane using the charged vertex position, for $K_L \to \pi^+\pi^-\pi^0$ events in the barrel region of the calorimeter. Black dots corresponds to 10 cm bin in R_T. For each dot, the average value is obtained performing a gaussian fit of ΔR distribution. **Right**: average value of Δt_γ, the difference between cluster measured time and expected photon time for $K_L \to \pi^+\pi^-\pi^0$ events. Black dots corresponds to 10 cm bin in R_T. For each dot, the average value is obtained performing a gaussian fit of Δt_γ distribution.

To improve the time resolution, T_{clu} needs to be corrected with a function that parameterizes the time spent by the electromagnetic shower to travel along the δ distance, t_{depth}. For each run period and calorimeter zone (barrel, endcaps and overlap), the difference between calorimeter cluster arrival time and expected time of flight until the apex point has been evaluated, as a function of δ:

$$\Delta t^{(0)} = T_{clu} - t_{exp\ apex} \tag{5.13}$$

$\Delta t^{(0)}$ is expected to be related to the t_{depth} variable. The t_{depth} distribution can be parameterized with a linear function, $P(1) + P(2) \times \delta$. The amount of the time deviation is $\sim$100 ps, about the same order of magnitude of the calorimeter time resolution ($\sim$200 ps), and depends on the photon energy. The parameters $P(1)$ and $P(2)$ are evaluated separately for each run period and each calorimeter region.

Finally, a correction is applied by subtracting t_{depth} to the measured time T_{clu} (the so-called "linear correction"):

$$T^{(1)}_{clu\ corr} = T_{clu} - t_{depth} = T_{clu} - [P(1) + P(2) \times \delta]\,, \tag{5.14}$$

where δ is the depth distance computed using the neutral vertex information, as explained in the following. The depth value δ is unknown in K_L decays to neutral particles, since the photon impact point on the calorimeter cannot be evaluated with high precision, then the δ value has been computed using an iterative procedure:

- find a neutral vertex and the related δ by using the measured cluster time information without any correction;

- compute a new neutral vertex applying a linear correction (Eq. 5.14) to the measured cluster time, and find a new depth value.

Three iterations of these steps are enough to get a δ value compatible with the value obtained from the charged vertex.

Fig. 5.5 shows the result of the corrections for barrel and endcaps calorimeter regions. The distortions from the linear trend for high values of depth are due to the fact that the calorimeter thickness is 23 cm and the cluster reconstruction accuracy decreases. Once the measured time is corrected with the time spent by the photon

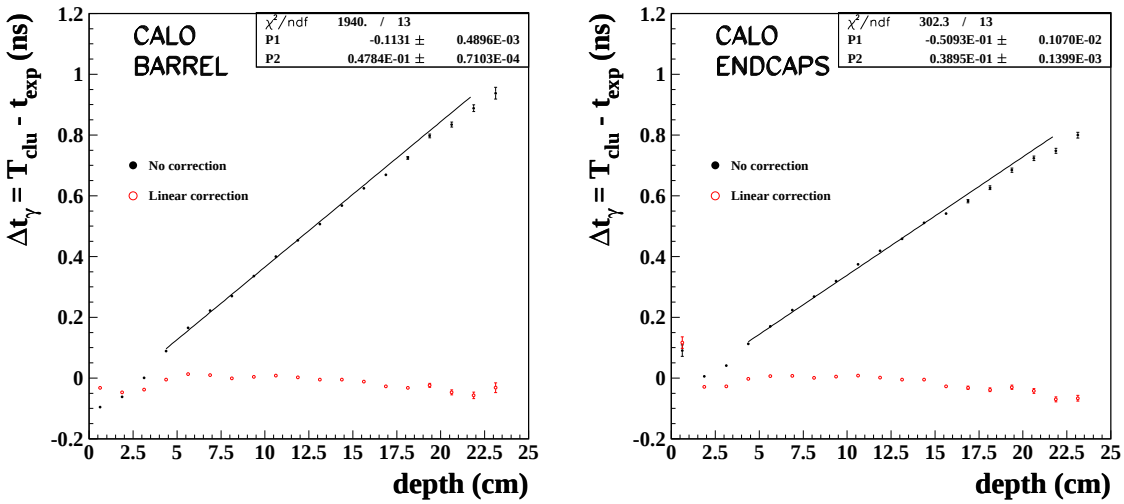

Figure 5.5: Δt distribution as a function of *depth* before and after the linear correction (Eq. 5.14). **Left**: barrel region; **Right**: end-caps.

travelling along the depth distance, a new time difference is evaluated:

$$\Delta t^{(1)} = T_{clu} - t_{exp\ lin} \tag{5.15}$$

where $t_{exp\ lin}$ is defined as

$$t_{exp\ lin} = \frac{L_K}{\beta c} + \frac{L_{\gamma_{apex}}}{c} + \left[P(1) + P(2) \times \delta^{ch}\right] \tag{5.16}$$

δ^{ch} is the "true" depth value, derived from the charged vertex information.

The $\Delta t^{(1)}$ distribution as a function of L_K is shown in Fig. 5.6 on the left side. The linear correction is not enough to flatten the distribution and reach the zero axis: there is still a trend. This could be due to a TDC counts miscalibration. To correct the TDC's miscalibration it is necessary to correct the cluster time at raw data level, before the $t_{0,\ evt}$ corrections from the trigger (see Sec. 3.3). The deviations from the expected time can be described by a function: $f(T_{clu\ corr} + t_{0,\ evt})$. The time corrections at the second order are parameterized fitting $\Delta t^{(2)}$ difference, defined as:

$$\Delta t^{(2)} = t_{exp\ apex} - T_{clu\ corr} \tag{5.17}$$

as a function of the raw cluster time: $T_{clu\ corr} + t_{0,\ evt}$. For each run period a polynomial function is used: quadratic for low, and cubic for high $T_{clu\ corr} + t_{0,\ evt}$ times.

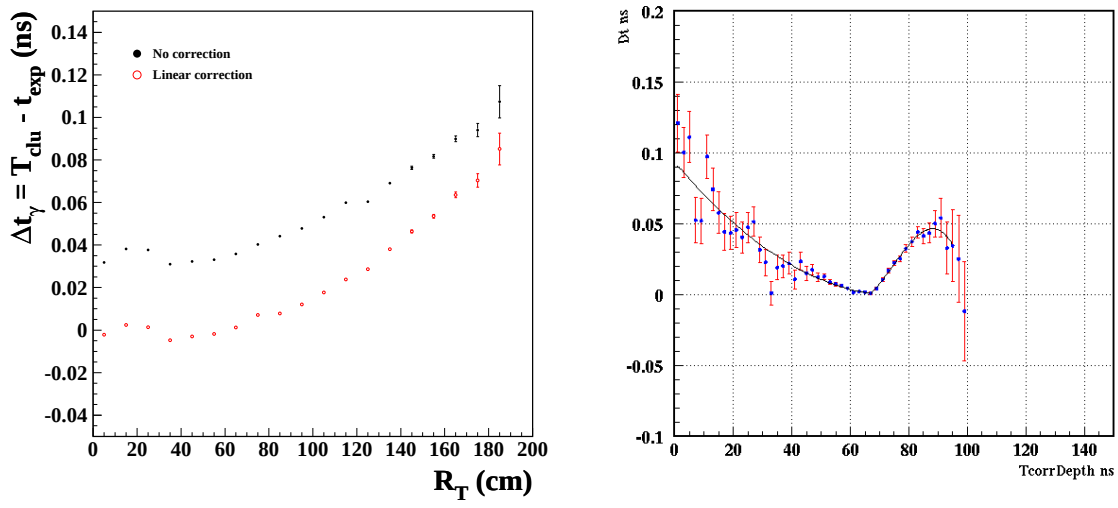

Figure 5.6: **Left**: Distribution of the Δt distribution as a function of L_K, before (black dots) and after (red dots) the linear correction. **Right**: Distribution of the $\Delta t^{(2)}$ difference as a function of the raw measured cluster time for one of the run periods. The fit function is a polynomial of second degree for $t < 70$ ns, and third degree for $t > 70$ ns.

Fig. 5.6 on the right side shows the correction fit result for the period n.8 as an example. Once extracted from the polynomial fit all the corrections for each run period, necessary to parameterize the TDC counts miscalibration, the cluster time is corrected with a function at raw level, $f(t^{\emptyset})$ with $t^{\emptyset} = T_{clu} + t_{0,\,evt}$, to correct the difference between expected and measured photon times.

$$T^{(2)}_{clu\ corr} = T^{(1)}_{clu\ corr} + f(t^{\emptyset}) \tag{5.18}$$

Similar time calibration has been applied to the Monte Carlo sample: the linear correction depth-dependent has been applied for each run period and each calorimeter zone.

Single-photon neutral vertex spatial resolution

After evaluating the parameters needed to re-calibrate the calorimeter raw times, the new neutral vertex has been computed using all the corrections, $R^{(1)}_{\gamma_i}$, $R^{(2)}_{\gamma_i}$. The new ΔR distributions are

$$\Delta R^{(0)} = L_K - R_{\gamma_i}$$
$$\Delta R^{(1)} = L_K - R^{(1)}_{\gamma_i}$$
$$\Delta R^{(2)} = L_K - R^{(2)}_{\gamma_i}$$

Fig. 5.7 shows ΔR for different calorimeter regions (barrel, end-caps left and right, overlap region) selected using the transverse radius R_T, which is the K_L decay length projected onto the transverse plane respect to the beam crossing line. Both corrections move the distributions towards zero, but this is not enough to obtain a flat distribution, especially for high values of R_T. The deviation ΔR reaches $\sim$0.2

cm on the fiducial volume border, this translates in a few permil effect on the K_L lifetime, that will be evaluated with a toy Monte Carlo and will be taken into account in the systematic error.

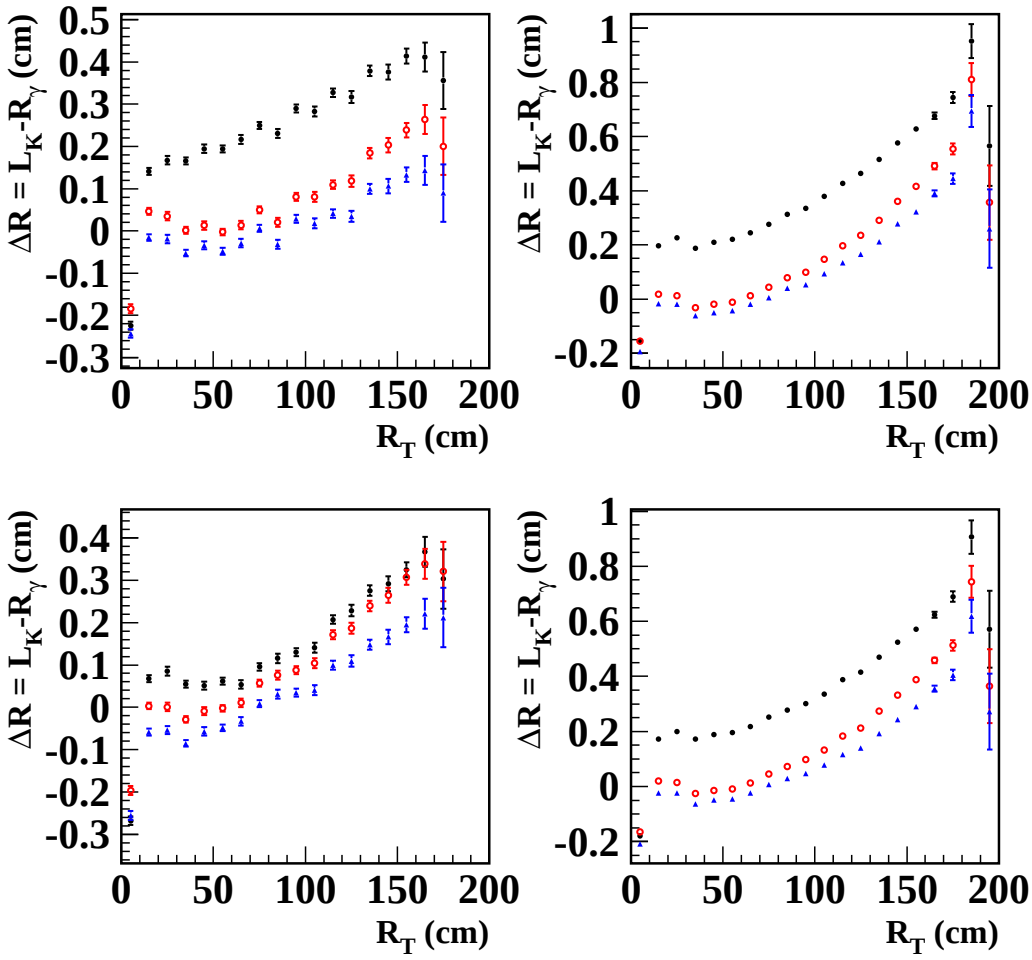

Figure 5.7: Data sample: ΔR distribution as a function of R_T for all 2005 statistics and different calorimeter regions. Black dots are used for neutral vertex evaluated without corrections, red circles for linear correction and blue triangles for the TDC miscalibration correction. **Top left**: end-cap left; **Top right**: barrel region; **Bottom left**: end-cap right; **Bottom right**: all the calorimeter.

The ΔR distributions for barrel, endcaps and overall calorimeter from Monte Carlo are shown in Fig. 5.8 with (red) and without correction (black). Without the correction, the shape is almost flat but shifted from zero; the linear correction is enough to shift towards zero the distribution.

The control sample $K_L \to \pi^+\pi^-\pi^0$ has been also used to estimate the spatial resolution of the single-photon neutral vertex reconstruction as a function of the measured energy, E_{clu}; it is better than 2.5% for photon clusters having $E > 50$ MeV. The spatial resolution to be used for $K_L \to \pi^0\pi^0\pi^0$ events has been parameterized

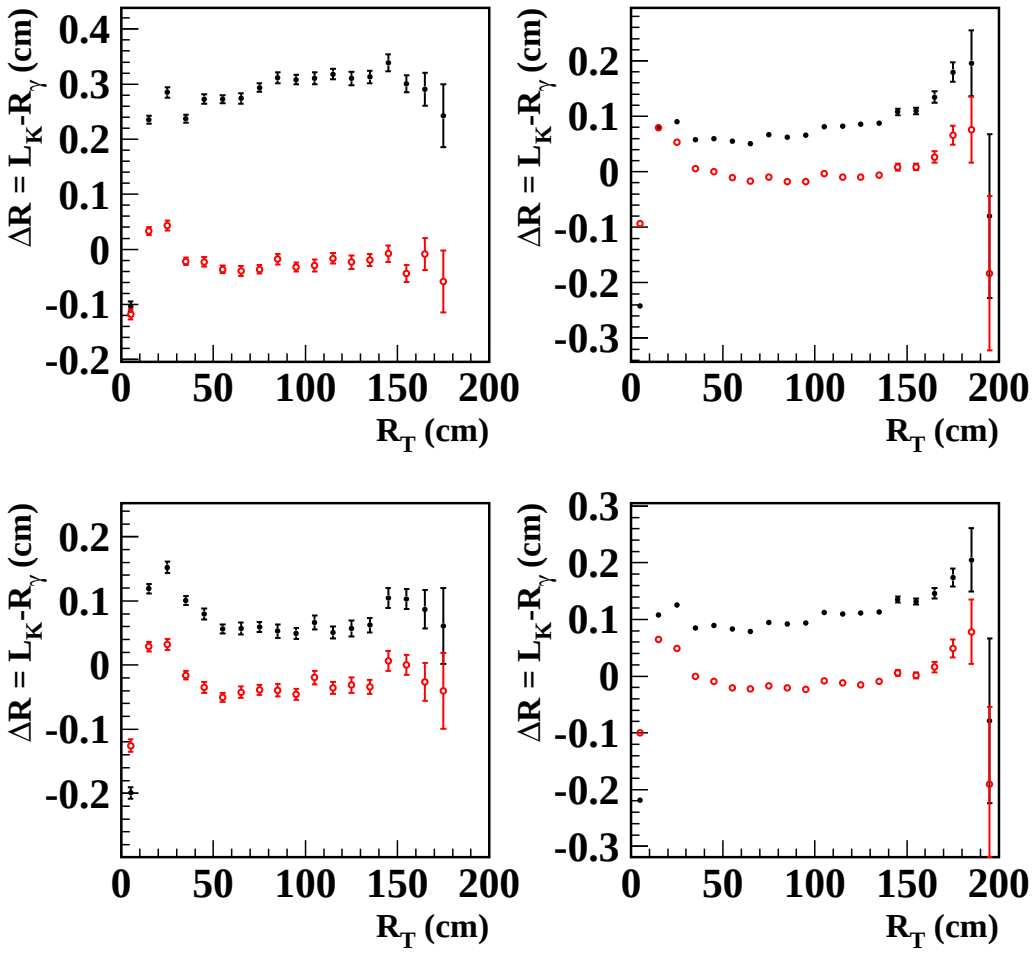

Figure 5.8: Monte Carlo sample: ΔR distribution as a function of R_T for all 2005 statistics and different calorimeter regions. Black dots are used for neutral vertex evaluated without corrections and red circles for linear correction. **Top left**: end-cap left; **Top right**: barrel region; **Bottom left**: end-cap right; **Bottom right**: all the calorimeter.

with an empirical law:

$$\sigma_{R_{\gamma_i}} = \left(\sigma_1^2 + \frac{\sigma_2^2}{E_{clu\,\gamma\,i}^{3/2}} \right)^{1/2} \tag{5.19}$$

where σ_1 and σ_2 are free parameters obtained by the fit separately for each run period. The ΔR difference distribution and its σ as a function of the energy E_{clu} is shown in Fig. 5.9 and Fig. 5.10 respectively for data and Monte Carlo.

The fit function for data in Fig. 5.9 does not reproduce the shape of σ for high values of energy: this can be explained with the worse spatial resolution of a high energy photon coupled with a second low energy photon. This could be due to a fake effect related to the way used to evaluate this resolution.

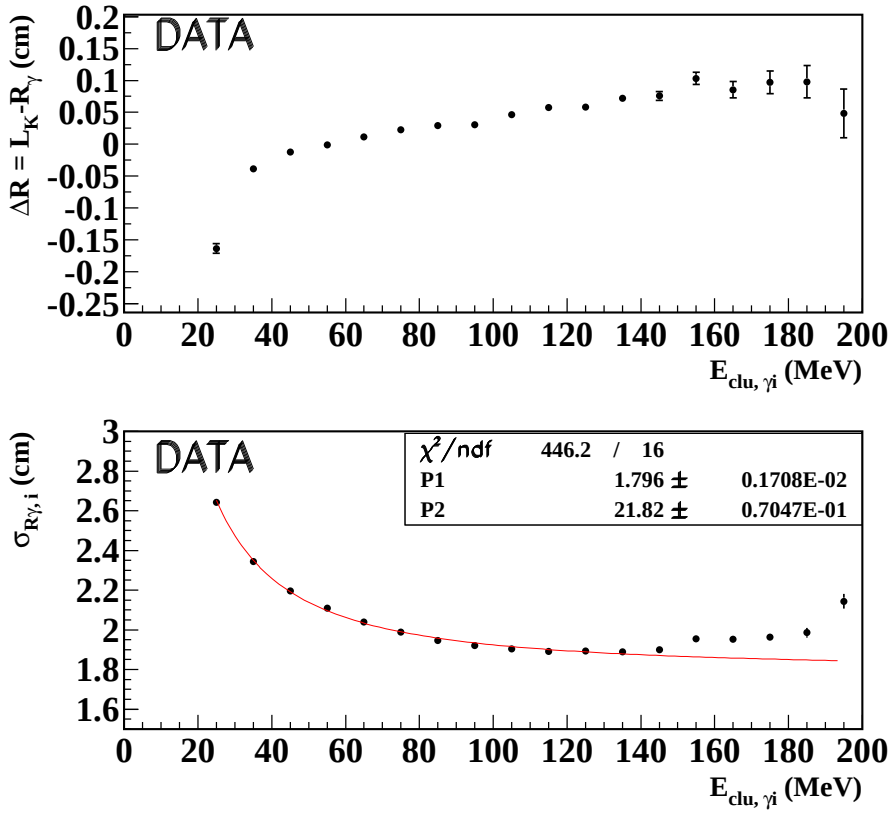

Figure 5.9: **Top**: Distribution of the difference ΔR as a function of the i-th photon cluster energy $E_{clu\,\gamma_i}$ for the 2005 $K_L \to \pi^+\pi^-\pi^0$ data sample. **Bottom**: Spatial resolution of the single-photon neutral vertex as a function of the energy.

5.3.2 Single-photon K_L neutral vertex reconstruction efficiency

After the calibration of the position of the single-photon neutral vertex for data and Monte Carlo, and after the determination of the spatial resolution as a function of the photon energy, the single-photon K_L neutral vertex reconstruction efficiency has been evaluated. The $K_L \to \pi^+\pi^-\pi^0$ events are again used, selected with the criteria explained in Sec. 5.3.1.

The vertex reconstruction efficiency has been evaluated computing the ratio:

$$\varepsilon_\gamma = \frac{N_{\gamma\,rec}}{N_{\gamma\,tag}} \tag{5.20}$$

where $N_{\gamma\,rec}$ is the number of $K_L \to \pi^+\pi^-\pi^0$ events when both photons from $\pi^0 \to \gamma\gamma$ are detected, and $N_{\gamma\,tag}$ is the number of events when at least one photon (the *tagging* photon γ_{tag}) is detected. The procedure is the following:

1. using the γ_{tag} photon measured momentum and kinematic constraints of the $\pi^0 \to \gamma\gamma$ two-body decay, the expected momentum of the second photon γ_{exp} is evaluated;

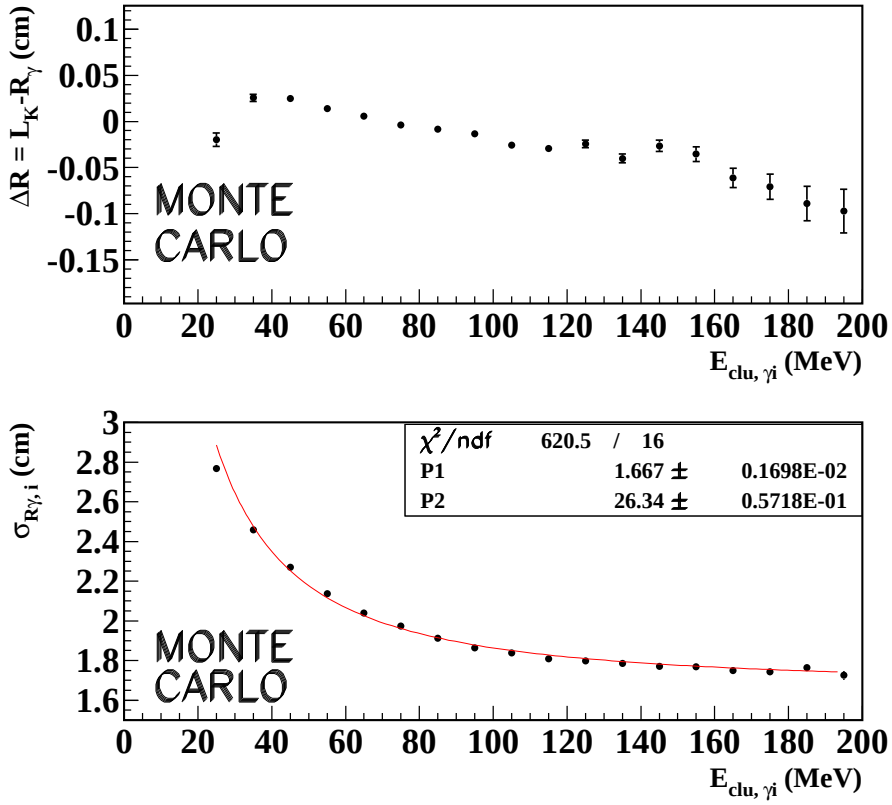

Figure 5.10: **Top**: Distribution of the difference ΔR as a function of the i-th photon cluster energy $E_{clu\,\gamma_i}$ for the 2005 $K_L \to \pi^+\pi^-\pi^0$ Monte Carlo sample. **Bottom**: Spatial resolution of the single-photon neutral vertex as a function of the energy.

2. a second photon γ_{rec} is looked for, and, if found, the compatibility between the γ_{rec} and γ_{exp} momenta is checked.

First, a tagging photon is searched for. Only events with at least one cluster reconstructing a vertex with $\Delta R = L_K - R_\gamma$ within $5\sigma_R$ from the L_K charged vertex are selected, using Eq. (5.19) for the evaluation of σ_R. All these photons are treated as γ_{tag} in turn. Using the K_L vertex position evaluated by the charged tracks and the γ_{tag} cluster position on the calorimeter, one can determine the unit vector of the momentum of the tagging photon $\hat{\omega}_{\gamma\,tag}$. Since the K_L momentum (from the $K_S \to \pi^+\pi^-$ tagging decay) and the charged pion tracks momenta are well measured, the missing momentum and energy are computed, as done in Sec. 5.3.1, assuming that γ_{tag} originates from a $\pi^0 \to \gamma\gamma$ decay. The energy of the tagging photon is obtained as:

$$E_{\gamma\,tag} = \frac{m_{\pi^0}^2}{2\,(E_{miss} - \vec{p}_{miss} \cdot \hat{\omega}_{\gamma\,tag})} \tag{5.21}$$

The momentum vector and energy of the second expected photon γ_{exp} from the π^0 decay have been evaluated:

$$\vec{\omega}_{\gamma\,exp} = \frac{\vec{p}_{miss} - E_{\gamma\,tag}\;\hat{\omega}_{\gamma\,tag}}{E_{miss} - E_{\gamma\,tag}} \tag{5.22}$$

and

$$E_{\gamma\, exp} = E_{miss} - E_{\gamma\, tag} \tag{5.23}$$

Only events which have the direction of γ_{exp} not crossing the beam line are selected, and this direction is extrapolated to obtain the expected impact point of the photon on the calorimeter.

To avoid associating γ_{exp} to a charged particle cluster, the reconstructed tracks from $K_S \to \pi^+\pi^-$ and $K_L \to \pi^+\pi^-\pi^0$ decays are extrapolated to the calorimeter and the corresponding impact points are estimated. The distance between the impact point of γ_{exp} and of any track is required to be greater than 30 cm and greater than 8 cm in each of the coordinates x, y, z.

If a candidate γ_{rec} cluster is found that could correspond to the γ_{exp} cluster, to ensure the compatibility the criteria described in the following are applied. The position of the single-photon neutral vertex must satisfy:

$$\Delta R \equiv |R_{\gamma\, tag} - R_{\gamma\, rec}| < 5\sigma_R \tag{5.24}$$

where σ_R is estimated as the sum combined in quadrature of the values from Eq. (5.19) for γ_{tag} and γ_{rec}. Using the γ_{rec} cluster position and the charged vertex position, it is possible to compute the γ_{rec} momentum unit vector, $\hat{\omega}_{\gamma\, rec}$, and evaluate the angle between the γ_{exp} and γ_{rec} momenta:

$$\cos\vartheta_{rec\, exp} = \hat{\omega}_{\gamma\, rec} \cdot \hat{\omega}_{\gamma\, exp} \tag{5.25}$$

To count a photon as found for the efficiency evaluation (for the numerator of Eq. (5.20)), we required $\cos\vartheta_{rec\, exp} > 0.6$ for data and $\cos\vartheta_{rec\, exp} > 0.65$ for Monte Carlo. This latter cut is a little tighter compared to data because Monte Carlo events have a slightly better resolution. Moreover, the cluster has to be in the same region (barrel, endcap or overlap) where it is expected it to be from kinematics.

The single-photon vertex reconstruction efficiency has been evaluated according to the Eq. (5.20), with two different approaches:

1. photons are counted as found for $N_{\gamma\, rec}$ by requiring: the compatibility of the γ_{tag} and γ_{rec} neutral vertex, and a cluster not associated to charged tracks; all the clusters not associated to charged tracks are used for the normalization $N_{\gamma\, tag}$;

2. all the calorimeter clusters are counted for the normalization $N_{\gamma\, tag}$, while the compatibility of the γ_{exp} and γ_{rec} neutral vertex is required for $N_{\gamma\, rec}$. Clusters mis-associated to tracks, due to a wrong extrapolation of a reconstructed track, are also recovered, requiring a 5σ compatibility from the charged vertex, an angular compatibility applying the cut $\cos\vartheta_{rec\, exp} > 0.95$ for data and Monte Carlo, and $|\delta_{TOF}| < 2$, where $\delta_{TOF} = T_{clu} - \frac{L_K}{\beta c} - \frac{d}{\beta_\pi c}$ represents the difference between the cluster measured time and the time-of-flight of the particles. L_K is the charged vertex, and d is the extrapolated distance from the point of closest approach of the track to the K_L line of flight to the impact point on the calorimeter [42].

The reconstruction efficiency was evaluated as a function of the expected photon energy $E_{\gamma_{exp}}$ and the transverse radius $R_T = \sqrt{x^2 + y^2}$, with x, y coordinates of the

K_L neutral vertex given by the tagging photon; the efficiencies have been studied for both approaches and for each of the three calorimeter regions (BA, EC, OV).

Figs. 5.11 and 5.12 show the data and Monte Carlo comparison for the efficiency computed with both approaches, for barrel, endcaps and overlap region, as a function of $E_{\gamma_{exp}}$ and of the transverse radius R_T of the single-photon K_L neutral vertex reconstructed using γ_{tag}.

These distributions show a very good data-Monte Carlo agreement. The efficiency evaluated with the second method is always lower than with the first method, because in the first approach the π^0 Dalitz decays ($\pi^0 \to e^+e^-\gamma \sim 1.2\%$) are not taken into account, and in the second approach the clusters of these events are counted in the normalization factor $N_{\gamma\, tag}$.

The efficiency increases with the energy of the photon, and the trend depends on the calorimeter region, Fig. 5.11:

- in the barrel (BA) the efficiency rapidly increases and reaches a plateau in both approaches for photons with energy greater than 50 MeV, and shows a small decreases for photons with energy greater than 150 MeV; this effect is due to the worse reconstruction of a low energy tagging photon;

- in the endcaps (EC) with the first approach the efficiency increases with the energy until a plateau is reached, while with the second approach the efficiency does not reach a well-defined plateau;

- in the overlap region (OV) the efficiency curve has a different behaviour than in the previous cases, but similar in both approaches.

As one can see in Fig. 5.12, the single-photon neutral vertex reconstruction efficiency is strongly dependent on the transverse radius R_T of the K_L decay vertex: when a π^0 decays near the calorimeter (high transverse radius R_T), it's more difficult to separate and identify the produced photons. Moreover, the tracks detected by the DC are shorter, and the low accuracy reconstruction doesn't allow to recover the clusters wrongly associated to tracks.

The more the vertex is far from low acceptance detector regions, like beam line or QCALs (small angle calorimeters, whose information is not used in this analysis), the higher is the probability to detect the photons.

Also if the second approach to evaluate the efficiency tries to recover the clusters misassociated to tracks, too loose cuts cannot be used, since spurious tracks could be considered: in fact, the very restrictive requests on the K_L vertex and cluster times compatibility make this approach not sufficient to perform this recovery.

In the efficiency evaluation algorithm, the photons must be in the same calorimeter region predicted from kinematics. This request is independent of the neutral vertex compatibility cut, so the spatial acceptance is further reduced. The efficiency obtained with these methods cannot be directly used and there is need to correct the absolute Monte Carlo efficiency with the ratio $\varepsilon_{data}/\varepsilon_{MC}$, evaluated for both methods.

The shape of the efficiencies already evaluated for data and Monte Carlo are similar. Fig. 5.13 shows the efficiencies ratio $\varepsilon_{data}/\varepsilon_{MC}$ as a function of the energy of the expected photon and as a function of the transverse radius of the tagging

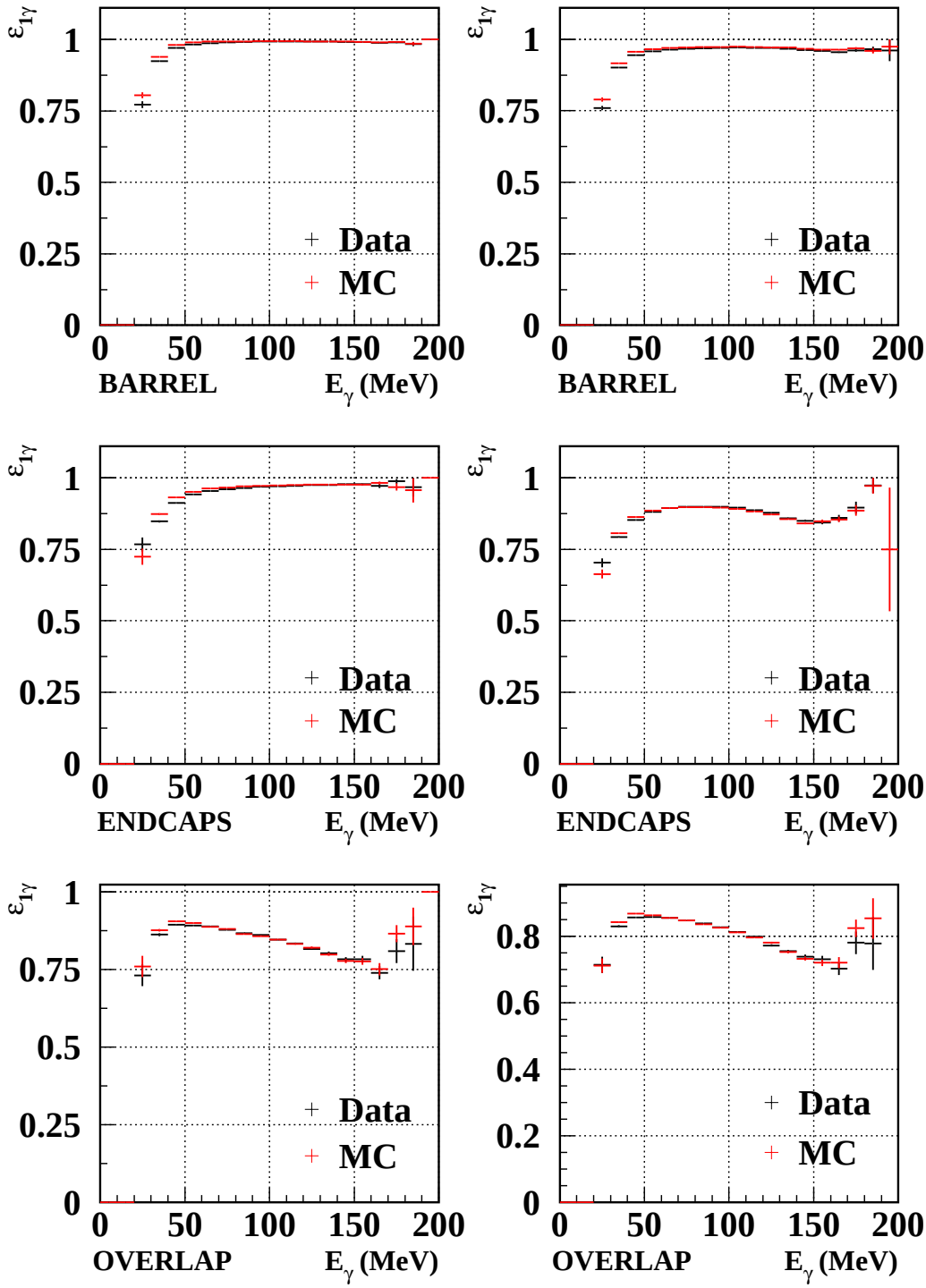

Figure 5.11: Single-photon efficiency as a function of $E_{\gamma_{exp}}$ for data (black) and Monte Carlo (red), from top to bottom for Barrel, Endcaps and Overlap regions. **Left**: First approach; **Right**: Second approach.

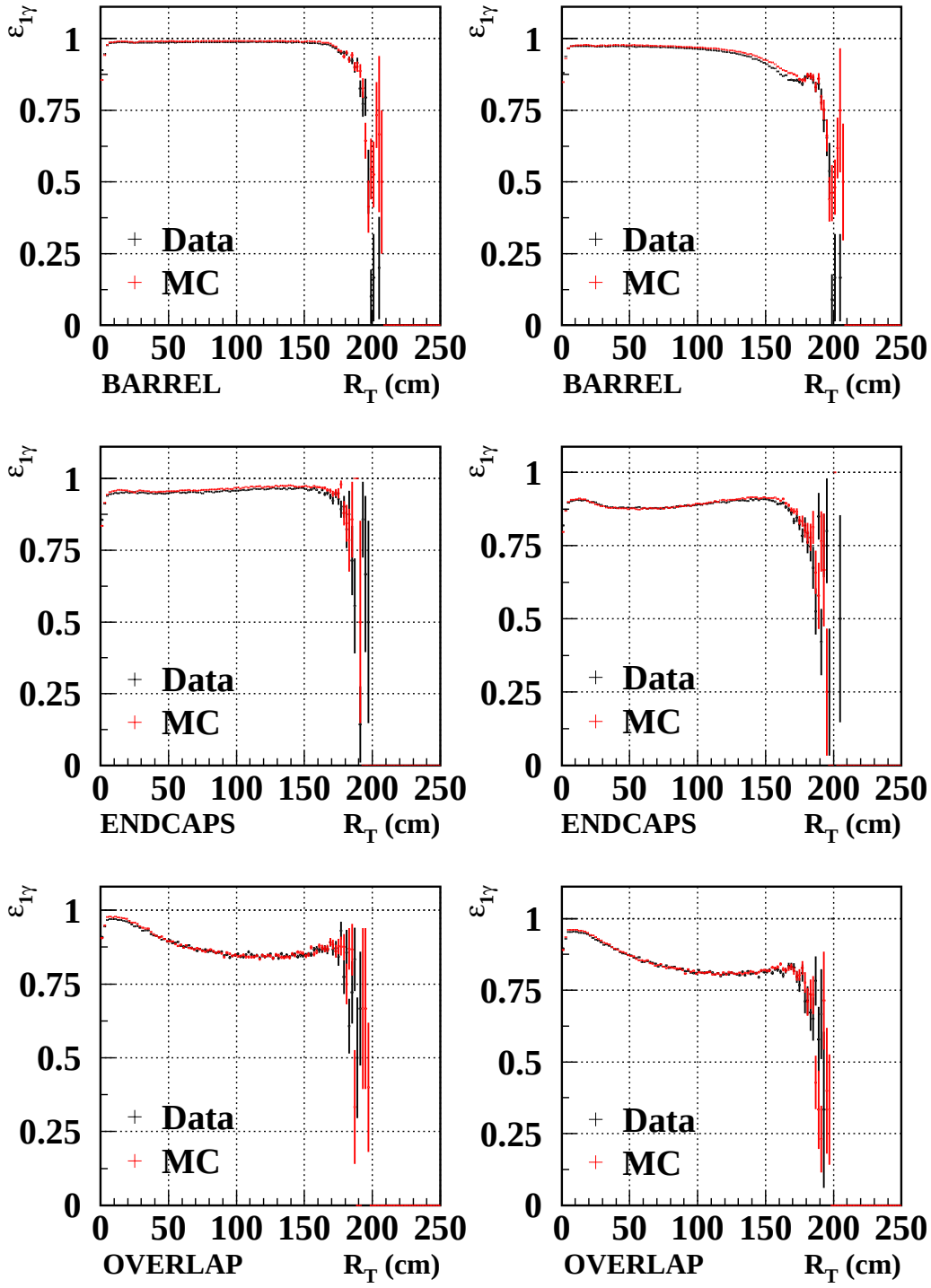

Figure 5.12: Single-photon efficiency as a function of the transverse radius R_T of the γ_{tag} single-photon K_L neutral vertex evaluated for data (black) and Monte Carlo (red), from top to bottom for Barrel, Endcaps and Overlap regions. **Left**: First approach; **Right**: Second approach.

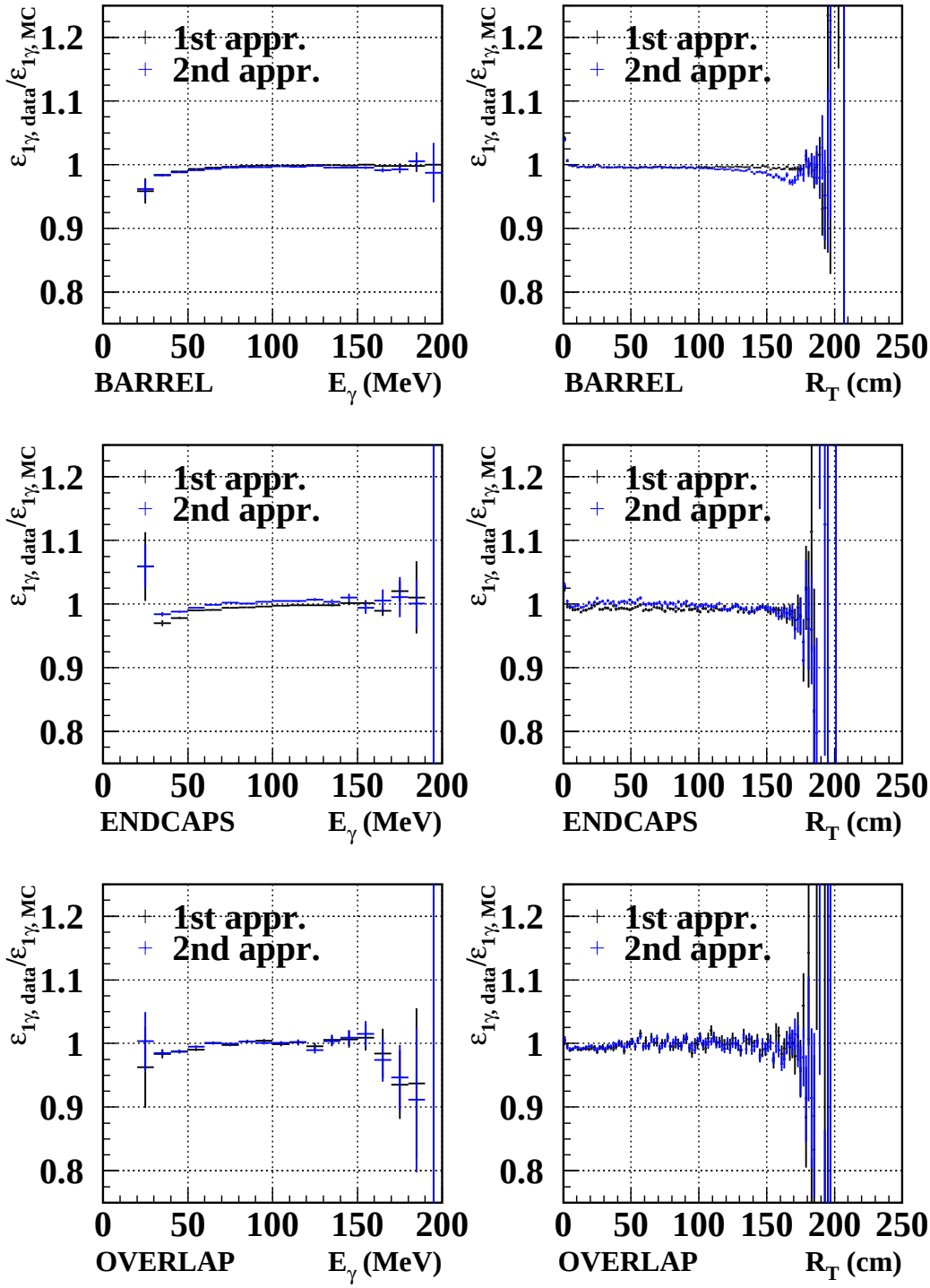

Figure 5.13: Ratio of data-Monte Carlo single-photon efficiencies $\varepsilon_{data}/\varepsilon_{MC}$ as a function of $E_{\gamma_{exp}}$ (**left**) and as a function of the transverse radius R_T of the γ_{tag} single-photon neutral vertex (**right**), black and blue dots are respectively for the first and second approach, from top to bottom for Barrel, Endcaps and Overlap regions.

photon, for each one of the three calorimeter regions. For both approaches, these ratios appear to be compatible. The fall of the ratio $\varepsilon_{data}/\varepsilon_{MC}$ for transverse radii $R_T > 160$ cm is not worrying, since decays will be selected in a safe fiducial volume. Only events with neutral vertex reconstructed with transverse radius in the range $35 < R_T < 160$ cm will be retained.

The single-photon reconstruction efficiency depends on the two variables, E_γ and R_T, hence, to correct the absolute Monte Carlo efficiency, a two-dimensional matrix has been used to take into account of the correlations.

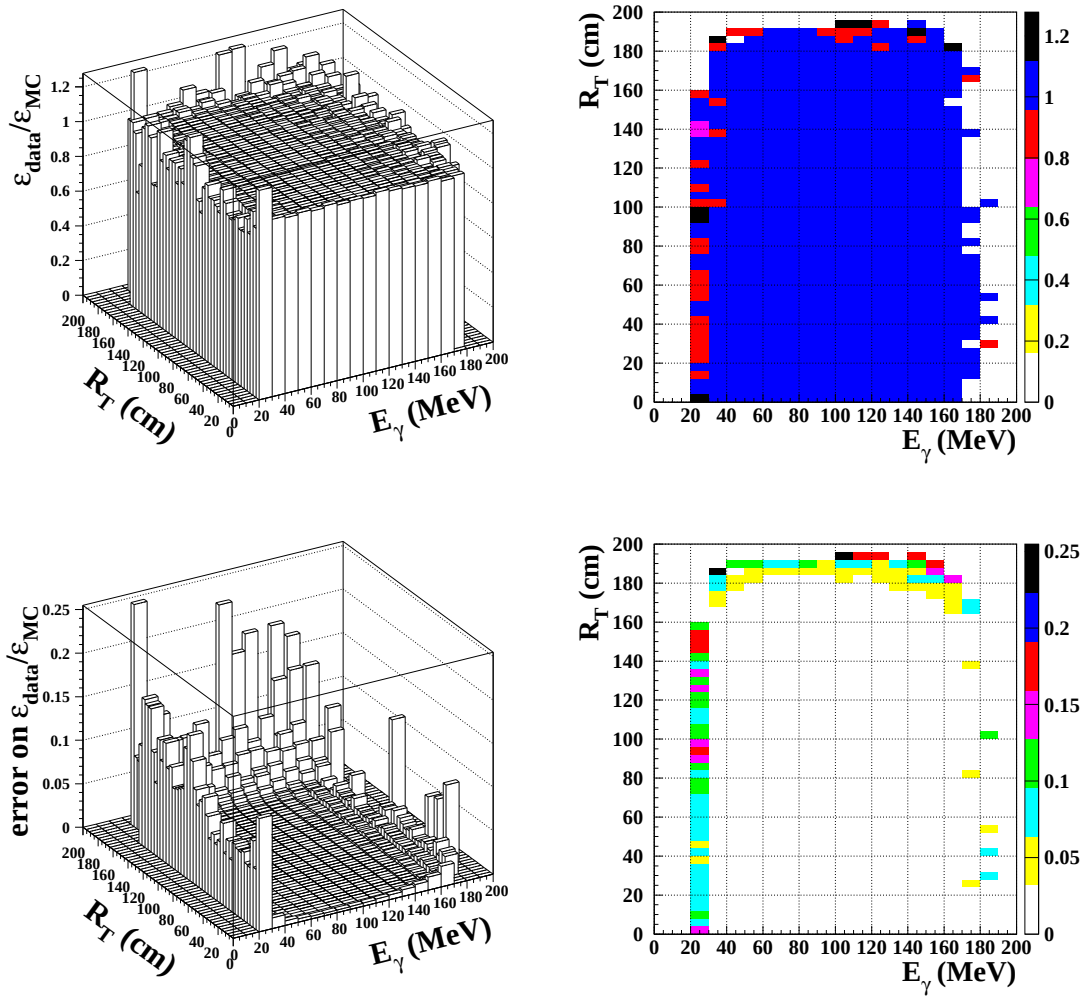

Figure 5.14: **Top left** and **right**: ratio of data-Monte Carlo single-photon efficiencies $\varepsilon_{data}/\varepsilon_{MC}$ as a function of R_T and $E_{\gamma_{exp}}$ using the first approach. **Bottom left** and **right**: associated errors.

Fig. 5.14 and Fig. 5.15 show the two-dimensional plots ($R_T \times E_{\gamma_{exp}}$) of the efficiency ratio $\varepsilon_{data}/\varepsilon_{MC}$ and relative errors, respectively for the first and the second approach.

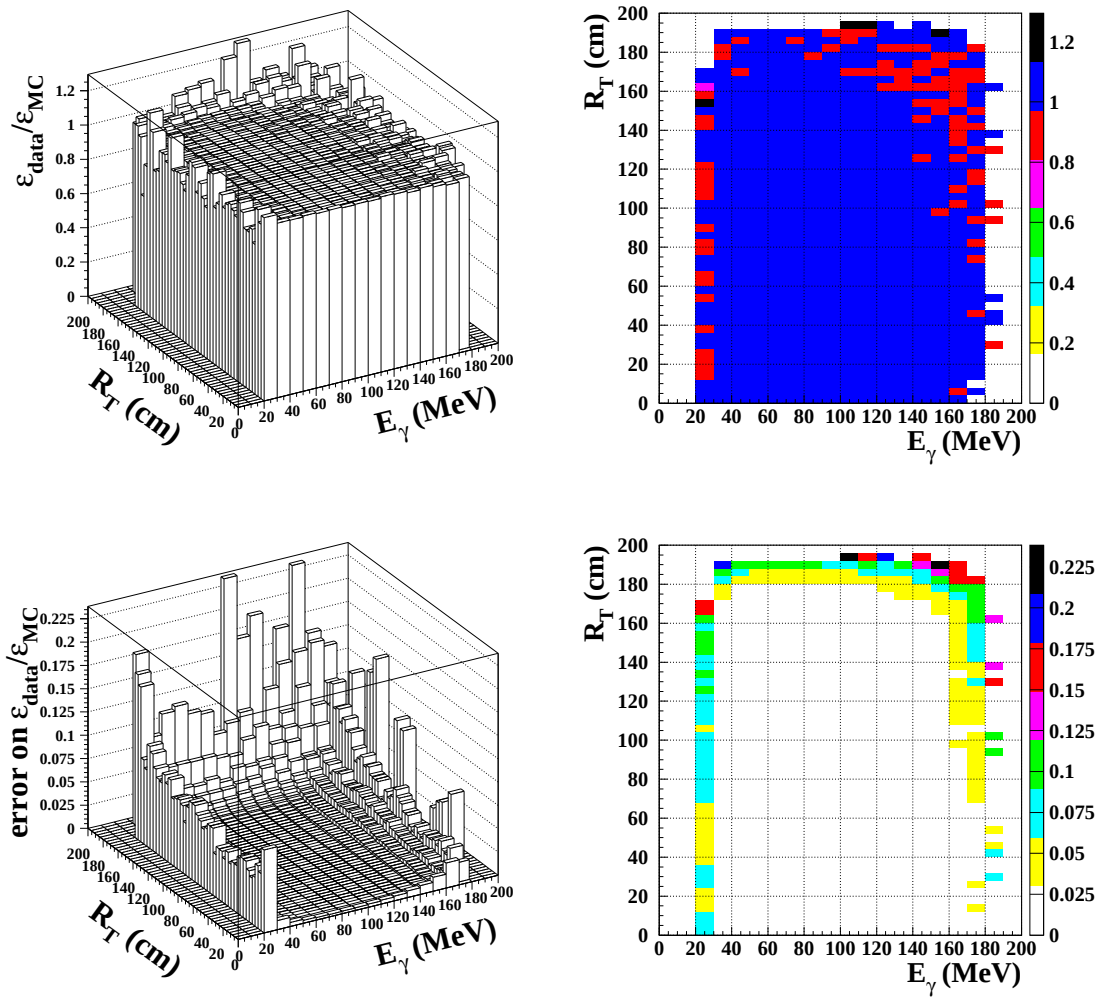

Figure 5.15: **Top left** and **right**: ratio of data-Monte Carlo single-photon efficiencies $\varepsilon_{dt}/\varepsilon_{MC}$ as a function of R_T vs. $E_{\gamma_{exp}}$ using the second approach; **Bottom left** and **right**: associated errors.

To choose the right one of the two approaches to correct the absolute Monte Carlo efficiency, a dedicated Monte Carlo sample was developed, to study in $K_L \to \pi^0\pi^0\pi^0$ decays how many photons are reconstructed in the calorimeter, and in which region. This simulation allowed to estimate the single-photon efficiency for $K_L \to \pi^0\pi^0\pi^0$ sample, used for the lifetime measurement.

By comparing both the approaches with the simulated efficiency, it was observed that the last one is more similar to the efficiency trend evaluated only retaining the clusters not associated to charged tracks. In fact, using the first method, the efficiency is evaluated on a sample of cleaner retained events, dropping the ambiguities due to the mistaken association of clusters from charged particles to photons arising from K_L neutral decay.

In the end, the first method was adopted for the two-dimensional matrix chosen

to reproduce the single-photon reconstruction efficiency. This matrix, $\mathcal{M}_{ij}$ shown in Fig. 5.14, is used to correct photon counting and the neutral vertex reconstruction for $K_L \to \pi^0\pi^0\pi^0$ decays, as explained in Sec. 5.4.1.

5.4 $K_L \to \pi^0\pi^0\pi^0$ decay identification

The K_L vertex position from $K_L \to \pi^0\pi^0\pi^0$ decays is obtained from arrival times of the photons on the calorimeter. The K_L decay vertex is requested to lie along the K_L line of flight reconstructed by the tagging decay $K_S \to \pi^+\pi^-$. Every photon arrival time gives an independent determination of the K_L decay length, L_K. The final value of L_K is obtained with a sigma-weighted average of all K_L decay length measurements.

5.4.1 Multiphoton vertex

The decay vertex of $K_L \to \pi^0\pi^0\pi^0$ decay is reconstructed grouping all the single-photon neutral vertices in one multiphoton vertex. A deviation in distance for each couple of single-photon vertices along the K_L line of flight is evaluated as:

$$D_{\gamma_i\gamma_j} = \frac{\left|R_{\gamma_i} - R_{\gamma_j}\right|}{\sigma_{\gamma_i\gamma_j}}, \tag{5.26}$$

where $i \neq j$ are indices looping on clusters not associated to charged tracks, R_{γ_i} is the i-th single-photon vertex position projected on the K_L line of flight, and $\sigma_{\gamma_i\gamma_j} = (\sigma^2_{\gamma_i} + \sigma^2_{\gamma_j})^{1/2}$, where σ_{γ_i} is the spatial resolution on the i-th single-photon vertex position evaluated with Eq. 5.19. All single-photon vertices are selected by requiring:

$$D_{\gamma_i\gamma_j} < 5. \tag{5.27}$$

This request yields a series of single-photon vertices, the so-called *chain*, that can include two or more single-photon vertices if each chain vertex lies close to another chain vertex within 5 σ. If the chain cannot be found, the event is discarded. If more than one chain is built, the chain with the maximum number of photons is chosen. If two chains have the same number of photons, the chain with higher total energy is selected, where the total energy is evaluated by adding energies of the photon clusters associated to the chain. This is done to reject the chain with accidental low energy photons from machine background.

The *photon multiplicity* refers to the number of single-photon vertices that belong to a chain. $K_L \to \pi^0\pi^0\pi^0$ decays are identified by selecting events with photon multiplicity $N \geq 3$. The photon multiplicity is corrected for the single-photon neutral vertex reconstruction efficiency evaluated in Sec. 5.3.2. As clearly visible in Fig. 5.13, for Monte Carlo sample the uncorrected photon multiplicity is generally higher than for data. For each Monte Carlo event, m uniform deviations r_i are selected, with $i = 1 \cdots m$ (one for each event cluster), and the i-th cluster is discarded if $r_i > \mathcal{M}_{ij}$, where $\mathcal{M}_{ij}$ is the matrix element of the data-MC single-photon efficiencies ratio.

The multiphoton vertex position for $K_L \to \pi^0\pi^0\pi^0$ events is evaluated as:

$$\vec{x}_{K_L} = \vec{x}_\phi + \hat{p}_{K_L}\left(\sigma^2_{\gamma\ tot}\sum_{i=1}^{n}\frac{R_{\gamma_i}}{\sigma^2_{\gamma_i}}\right) \tag{5.28}$$

where the index $i = 1 \cdots n$ loops on all single-photon vertices (R_{γ_i}) belonging to the chain after the merging procedure described in Sec. 5.4.2, and $\sigma_{\gamma\ tot}$ is defined as:

$$\sigma_{\gamma\ tot} \equiv \left(\sum_{i=1}^{n}\frac{1}{\sigma^2_{\gamma_i}}\right)^{-1/2}, \tag{5.29}$$

with σ_{γ_i} given by Eq. 5.19 (we remind that the multiphoton vertex position must lie along the K_L line of flight reconstructed using the tagging decay $K_S \to \pi^+\pi^-$, see Sec. 4.2).

5.4.2 Photon multiplicity and cluster merging

Fig. 5.16 on the left side shows the photon multiplicity, N_γ, for $K_L \to \pi^0\pi^0\pi^0$ event

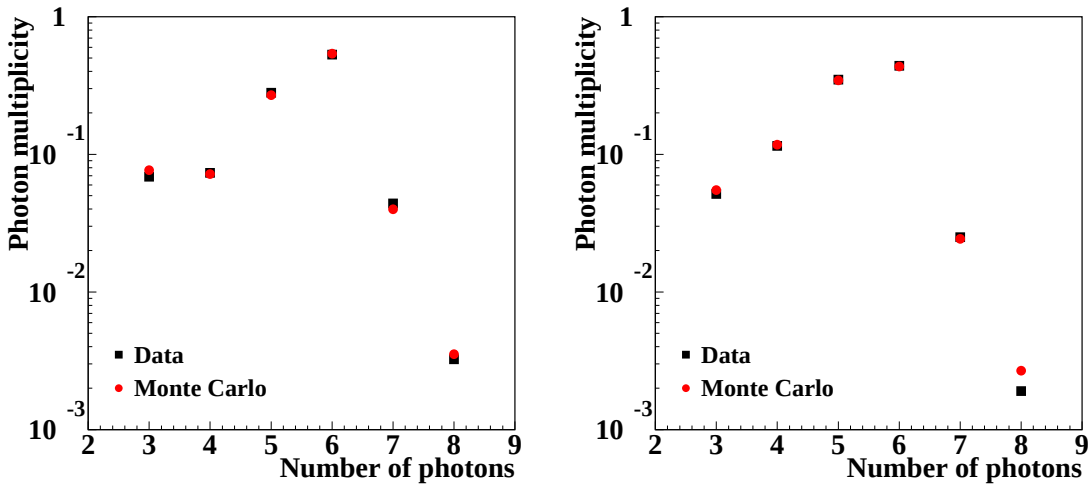

Figure 5.16: Photon multiplicity normalized distribution for data (black dots) and Monte Carlo (red dots) before (**left**) and after (**right**) the merging procedure, inside the fiducial volume.

candidates normalized with the total number of events, N_{tot}, in the fiducial volume. The data - Monte Carlo disagreement for $N_\gamma = 7$ is due to events with one or more fake vertices due to cluster splitting: one photon could produce two near clusters instead than one. This effect is underestimated in the Monte Carlo simulation. This cluster splitting effect explains the significative presence of events with $N_\gamma = 7, 8$ that originate from a $K_L \to \pi^0\pi^0\pi^0$ decay. To reduce the cluster splitting effect and improve the data - Monte Carlo agreement in the photon multiplicity distribution, a procedure was developed to merge two splitted clusters into one.

For each event, the two nearest reconstructed photons are considered, *i.e.* the cluster pair with the smallest distance between centroids: $d_{12} \equiv |\vec{x}_1 - \vec{x}_2|$. The

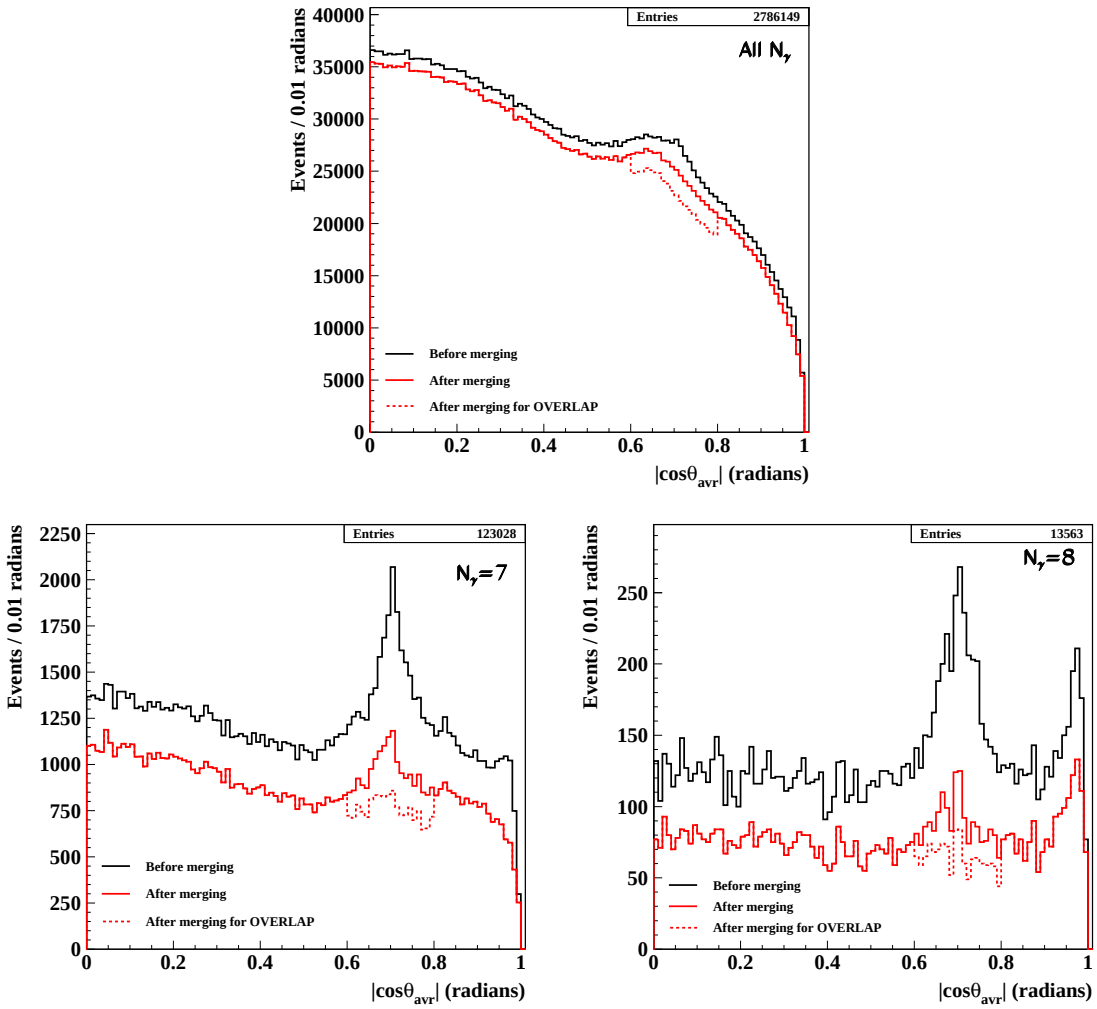

Figure 5.17: Distribution of the absolute value of the polar angle $\cos\theta_{avg}$ in the fiducial volume for run period n.3. Black line is used before the merging procedure, red dashed line after the first merging procedure, red solid line after the specific merging procedure for the overlap region. (**a**) All; (**b**) $N_\gamma = 7$; (**c**) $N_\gamma = 8$.

polar angle of the average position of the two clusters is evaluated, θ_{avg}. Fig. 5.17 shows the $\cos\theta_{avg}$ distributions in the fiducial volume for run period n.3 data sample (a) for $N_\gamma = 7$ (b) and $N_\gamma = 8$ (c). If the splitting cluster phenomenon would be homogeneous in all the fiducial volume, the $\cos\theta_{avg}$ distribution should be flat. On the contrary, as shown in Fig. 5.17, a peak is clearly evident in the range $0.6 < |\cos\theta_{avg}| < 0.8$, which corresponds to the interface calorimeter region of barrel and endcaps. Here the interface region is not the same overlap region used for single-photon efficiency evaluation as defined in Sec. 5.3.2. The cluster pair corresponding to the two nearest centroids with average position in the barrel-endcaps overlap region could be the uncorrect outcome of the reconstruction algorithm, that provides two clusters in different regions of the calorimeter instead than one. To correct this effect, all the events which have $\cos\theta_{avg}$ reconstructed in the interface region have been undergone an ad-hoc cluster merging procedure.

The quantity β_{12} for the two nearest clusters is defined as:

$$\beta_{12} \equiv \frac{d_{12}}{|t_1 - t_2|\ c}, \tag{5.30}$$

where d_{12} is the relative distance between the two nearest cluster centroids $d_{12} \equiv |\vec{x}_1 - \vec{x}_2|$, and t_1, t_2 are the arrival cluster times.

Two clusters with $\beta_{12} < 1$ cannot be originated by two separate photons arising from the same decay vertex. If L_1 and L_2 are defined as the distances between the clusters 1 and 2 and the common decay vertex, the distance between 1 and 2 is $\sqrt{L_1^2 + L_2^2 - 2L_1L_2\cos\theta_{12}}$, where θ_{12} is the opening angle centered in the K_L decay vertex between the clusters. Two clusters will have $\beta_{12} > 1$ if:

$$L_1^2 + L_2^2 - 2L_1L_2\cos\theta_{12} < (L_1 - L_2)^2 \tag{5.31}$$

or, equivalently, if $\cos\theta_{12} < 1$, that holds by assumption.

Taking into account resolution effects, the request $\beta_{12} < 1$ discriminates events in which a fake cluster arises from a fragment of another. A cluster pair with $\beta_{12} < 1$ is then the result of an instrumental cluster splitting, or a splitting effect due to bad cluster reconstruction.

The minimal energy of the two nearest clusters as a function of the variable β_{12} has been studied, to find an optimal algorithm for the cluster merging. Fig. 5.18 shows the distribution of E_{min} vs. β_{12} for nearest cluster pairs, for data and Monte Carlo.

The distributions for $N_\gamma = 3,\ 7,\ 8$ events, as expected from previous remarks on cluster splitting, have higher density for lower values of E_{min} and β_{12}: the lower energy cluster of the pair is a fake one.

Accordingly, the cluster pairs having:

$$\beta_{12} < 1.1 \quad \text{or} \quad E_{min} < (45 - 13\,\beta_{12})\ \text{MeV} \tag{5.32}$$

have been merged. The red line in Fig. 5.18 refers to the cut in β_{12} and E_{min}.

A first result in the $\cos\theta_{avg}$ is shown in Fig. 5.17 (red dashed line). As evident, this cut is not enough to drop the peak in the overlap region.

A tighter cut in the minimum energy is applied for all the events which have average position of the nearest cluster centroids reconstructed in the barrel-endcaps

interface region:

$$E_{min} < (60 - 10\,\beta_{12}) \text{ MeV} . \tag{5.33}$$

After this second cluster merging procedure, the $\cos\theta_{avg}$ distribution (red solid line) for $N_\gamma = 7,\ 8$ appears more flat (compared with black and red dashed distribution in Fig. 5.17).

When two clusters are merged in one, the resulting cluster position is evaluated as the energy-weighted average of the centroids' positions, while the time is given by the shortest between the arrival times. The new neutral vertex position is then evaluated.

Photon multiplicity distribution after merging procedure is shown in Fig. 5.16 on the right. There is a visible improvement in data - Monte Carlo agreement for $N_\gamma = 7$ events. Moreover, the fraction of $N_\gamma = 7$ and $N_\gamma = 8$ events in data sample is reduced: from 4.4% to 3.0% for $N_\gamma = 7$ and from 0.33% to 0.075% for $N_\gamma = 8$.

There is a disagreement between data and Monte Carlo for $N_\gamma = 8$ events, that are a few permil of the signal sample. The excess shown in the Monte Carlo cannot be ascribed to background. This could be explained with residual effects of cluster splitting. To reproduce the data, a cluster splitting algorithm is applied to the Monte Carlo, using a threshold of $\sim$1 photoelectron for each calorimeter channel, while in data the threshold is about 4-5 times larger; this difference is about 0.1% and can be considered negligible.

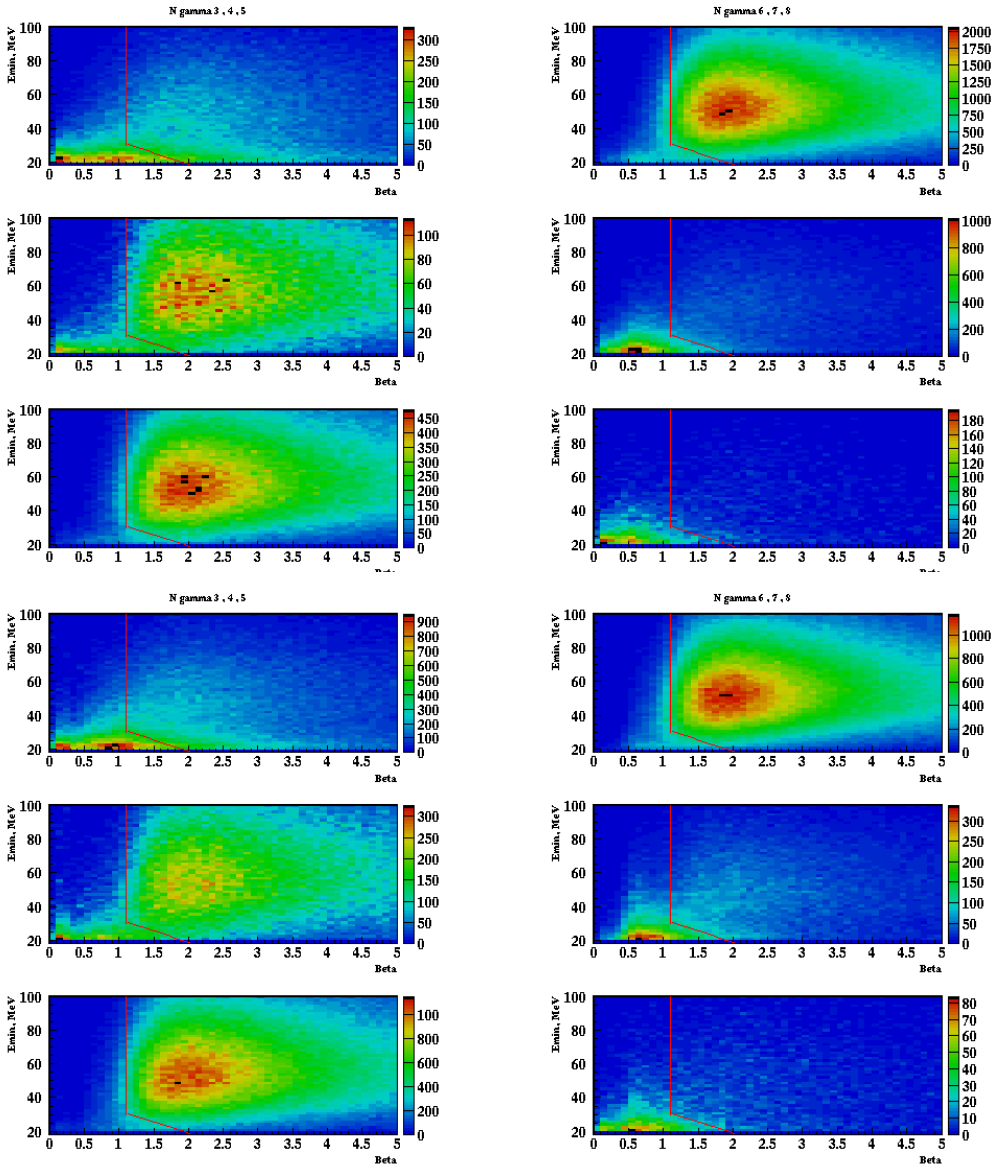

Figure 5.18: Cluster merging procedure for reconstructed cluster pairs with nearest centroids not associated to charged tracks. E_{min} vs. β_{12} for $N_\gamma = 3, 4, 5$ from top to bottom on the left side, and $N_\gamma = 6, 7, 8$ on the right side. for data (top 6 plots) and Monte Carlo (bottom 6 plots). Red solid line points at the merging cut: cluster pairs on the left side of the line have been merged.

Chapter 6

Signal selection and background

The background is concentrated in the event sample with three ($N_\gamma = 3$) and four ($N_\gamma = 4$) photons associated to the vertex, while the events with more than four photons are almost background free, as shown in Fig. 6.1 on the right side, for the Monte Carlo sample. The $N_\gamma = 3$ and $N_\gamma = 4$ samples are, from Monte Carlo, respectively ∼6.5% and ∼11.2% of the total number of events.

The dominant sources of background are:

1. $K_L \to \pi^+\pi^-\pi^0$ events where the K_L decays close to the calorimeter and the two charged pions have either one or none reconstructed track or a track not associated to a cluster;

2. the CP-violating decay $K_L \to \pi^0\pi^0$;

3. the regeneration process $K_L \to K_S \to \pi^0\pi^0$, where the K_S is regenerated either in the beam pipe, or in the inner wall of the drift chamber, or in the drift chamber itself (gas or wires);

4. nuclear interactions of the K_L meson with calorimeter wall nuclei;

5. semileptonic decays $K_L \to \pi^\pm e^\mp \nu$ and $K_L \to \pi^\pm \mu^\mp \nu$.

All these background components are simulated by the Monte Carlo, including nuclear interactions and regeneration processes (see Sec. 3.7).

6.1 Background rejection

Fig. 6.1 on the left side shows the photon multiplicity distribution after cluster merging, for data (black triangles), for a Monte Carlo sample containing only signal events $K_L \to \pi^0\pi^0\pi^0$ (green circles) and for a Monte Carlo sample including all K_L processes in their natural proportions (red circles).

There is reasonable agreement between data and Monte Carlo for $N_\gamma = 4$, 5 and 6. Moreover, there is agreement also between the whole Monte Carlo and the signal Monte Carlo, this suggests that the background is strongly suppressed for events with 4, 5 and 6 reconstructed photons.

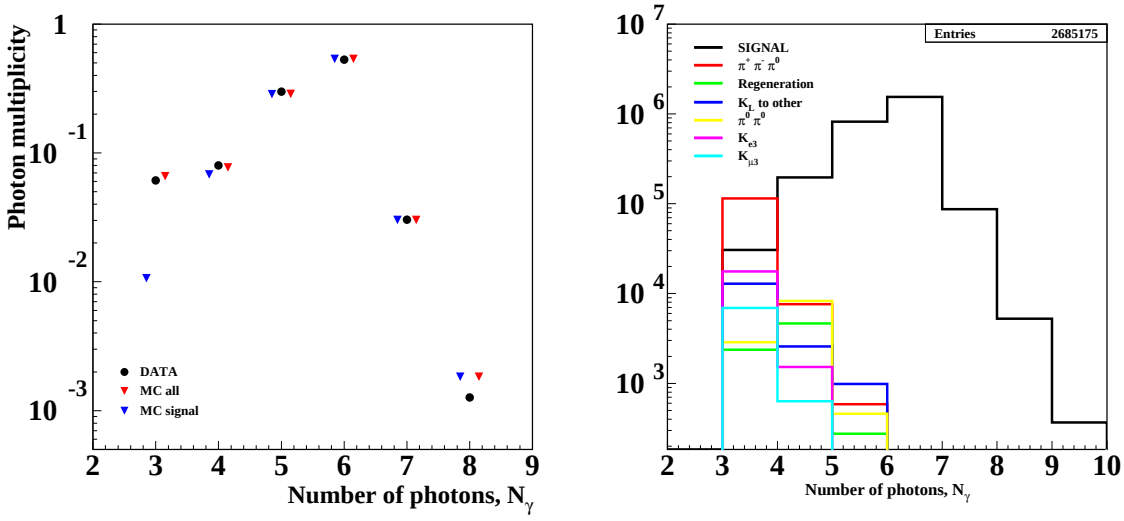

Figure 6.1: **Left**: photon multiplicity normalized distribution after cluster merging for data (black dots), Monte Carlo signal (blue triangles) and Monte Carlo including all K_L processes (red triangles). **Right**: number of reconstructed clusters for the Monte Carlo sample. Contributions from different processes are shown with different colours.

For the $N_\gamma = 8$ events, the two Monte Carlo samples are consistent, but there is a disagreement with data which cannot be ascribed to background, as explained in the end of Sec. 5.4.2.

The largest difference between the distributions for data and signal Monte Carlo is observed for the events with $N_\gamma = 3$. The agreement is much better between data and the Monte Carlo sample that includes all K_L processes, therefore the $N_\gamma = 3$ bin includes a significant fraction of background events. This background is strongly reduced by the cuts described in the following section.

6.1.1 Background rejection for three-photon vertices

The background is concentrated in the sample of events with $N_\gamma = 3$. Fig. 6.1 on the right side shows the photon multiplicity distribution associated to the reconstructed decay vertex, for signal and for background components that survive the preselection cuts (see Sec. 5.2) in the fiducial volume (FV) defined as:

$$\begin{array}{c} 35 < R_T < 150 \text{ cm} \\ |z| < 120 \text{ cm} \end{array} \tag{6.1}$$

where $R_T = \sqrt{x^2 + y^2}$ and (x, y, z) are the coordinates of the K_L decay vertex position. As clearly visible from Fig. 6.1 on the right, the main background component for events with $N_\gamma = 3$ comes from $K_L \to \pi^+\pi^-\pi^0$ decays.

The fraction of background sources that survive to the preselection cuts and the fiducial volume selection is shown in Tab. 6.1. $K_L \to$ *other* refers to processes that include nuclear interactions. To evaluate these fractions, the Monte Carlo sample for run period n.3 has been used. The percentage of signal events for $N_\gamma \geq 3$, $N_\gamma = 3$

and $N_\gamma = 4$ is, respectively, 93.55%, 17.02% and 88.07%. The sample of $N_\gamma \geq 5$ events is almost pure, with a background component of 0.111%.

K_L decay or process	$N_\gamma \geq 3$ $B/(S+B)$	$N_\gamma = 3$ $B/(S+B)$	$N_\gamma = 4$ $B/(S+B)$	$N_\gamma \geq 5$ $B/(S+B)$
All backgrounds	6.45 %	82.98 %	11.93 %	0.111 %
$K_L \to \pi^+\pi^-\pi^0$	4.30 %	60.50 %	3.40 %	0.025 %
$K_L \to K_S \to \pi^0\pi^0$	0.25 %	1.25 %	2.10 %	0.012 %
$K_L \to \pi^0\pi^0$	0.40 %	1.50 %	4.30 %	0.020 %
$K_L \to \pi^\pm e^\mp \nu$	0.67 %	9.30 %	0.69 %	0.008 %
$K_L \to \pi^\pm \mu^\mp \nu$	0.26 %	3.65 %	0.28 %	0.003 %
$K_L \to other$	0.57 %	6.78 %	1.16 %	0.043 %

Table 6.1: Background contamination $B/(S+B)$ in the fiducial volume for $N_\gamma \geq 3$, $N_\gamma = 3$, $N_\gamma = 4$ and $N_\gamma \geq 5$ events.

The total background contamination $B/(S+B)$ is ∼6.5% of analyzed events, ∼5.5% of which affects the sample with $N_\gamma = 3$ (mainly due to $K_L \to \pi^+\pi^-\pi^0$ events with splitted clusters or with a track not associated to cluster) and ∼0.9% affects the sample with $N_\gamma = 4$ (mainly due to K_L nuclear interactions with the calorimeter material, $K_L \to \pi^0\pi^0$ CP-violating decays and $K_L \to K_S \to \pi^0\pi^0$ regeneration events).

The background is rejected in the events with $N_\gamma = 3$ by two kind of cuts: one is based on the spatial and time properties of the clusters, the second deals with residual charged tracks.

The Monte Carlo distributions of RMS and $\cos\theta_{avg}$ variables have been studied for signal and background for each run period. First, we look at the root mean square (RMS) pull of the single-photon vertex positions about the multiphoton vertex position:

$$RMS \equiv \left[\frac{1}{n-1}\sum_{i=1}^{n}\left(\frac{R_{\gamma_i} - R_{K_L}}{\sigma_i}\right)^2\right]^{1/2} \tag{6.2}$$

where R_{γ_i} is the distance between the ϕ decay point and the neutral vertex computed with the i-th photon, σ_i the resolution on R_{γ_i} from Eq. 5.19 (to simplify, I will use σ_i in the following instead of $\sigma_{R_{\gamma_i}}$), and R_{K_L} the projected distance of the multiphoton vertex position (Eq. 5.28) onto the K_L line of flight. Events with $N_\gamma = 3$ having $RMS > 2$ are rejected.

Fig. 6.2 on the left side shows the Monte Carlo distribution of RMS variable for events with $N_\gamma = 3$, black line is used for the signal, and other colours for the background sources. The right side shows the distribution of $\cos\theta_{avg}$ for events with $N_\gamma = 3$. The main component of regeneration and nuclear interaction events have a polar angle of the average position of the two nearest clusters very close to 0 or π, *i.e.* near the beam line. To reject this background, only events with $|\cos\theta_{avg}| < 0.9$ are retained.

The second cut, applied to events with $N_\gamma = 3$, is based on tracking information. No veto is applied in this analysis on charged tracks that are not coming from K_S

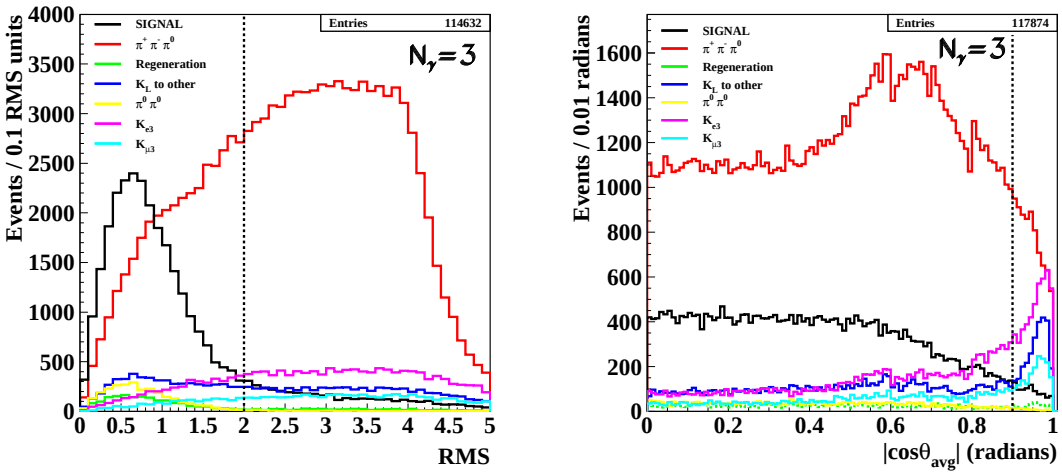

Figure 6.2: **Left**: Monte Carlo distribution of RMS variable with all background components for events with $N_\gamma = 3$; all the events on the right of the black line are rejected. **Right**: Monte Carlo distribution of the absolute value of $\cos\theta_{avg}$ variable with all background components for events with $N_\gamma = 3$; all the events on the right of the dashed black line are rejected.

$\rightarrow \pi^+\pi^-$ decay, since some fragments of tracks arising from $K_S \rightarrow \pi^+\pi^-$ secondary decay products could sometimes be observed in $K_L \rightarrow \pi^0\pi^0\pi^0$ events together with track fragments originating from photon conversion or from accidental events.

Tracks arising from K_L charged decays can be extrapolated along the K_L line of flight. The Point of Closest Approach (PCA) is defined as the point which minimizes the distance between a track and the K_L line of flight; the length d_{PCA} is defined as the distance between PCA and the multiphoton vertex position. Fig. 6.3 on the left side shows the Monte Carlo distribution of the d_{PCA} variable for all the processes. Events with $d_{PCA} < 10$ cm are rejected.

The Monte Carlo reconstruction efficiencies are shown in Tab. 6.2 for the signal and all the background components, before and after the cuts applied until now. No cuts on these variables have been applied to events with four reconstructed photons. The efficiency for regeneration and $K_L \rightarrow$ *other* processes after these cuts is not reduced enough. It is clear that nuclear interactions and regeneration processes in the fiducial volume are a relevant source of background, and considerably affect the signal proper time distribution.

The main contributions, $\bar{K}^0 N \rightarrow \Sigma\pi$, $\bar{K}^0 N \rightarrow \Lambda\pi$ and $K_L \rightarrow K_S$ regeneration are due to K_L interactions with detector materials. To reject this residual background, a very useful variable is the angle between the K_L momentum and the sum of all the photons momenta used to compute the multiphoton vertex:

$$\cos\alpha \equiv \frac{\vec{p}_{K_L} \cdot (\sum_{i=1}^{n} \vec{p}_i)}{|\vec{p}_{K_L}|\,|\sum_{i=1}^{n} \vec{p}_i|}, \tag{6.3}$$

where $\vec{p}_i$ are the photons' momenta reconstructed from time and energy cluster information. The Monte Carlo distribution of $\cos\alpha$ for signal and for background sources is shown in Fig. 6.3 on the right side, for events with $N_\gamma = 3$ and 4. Events

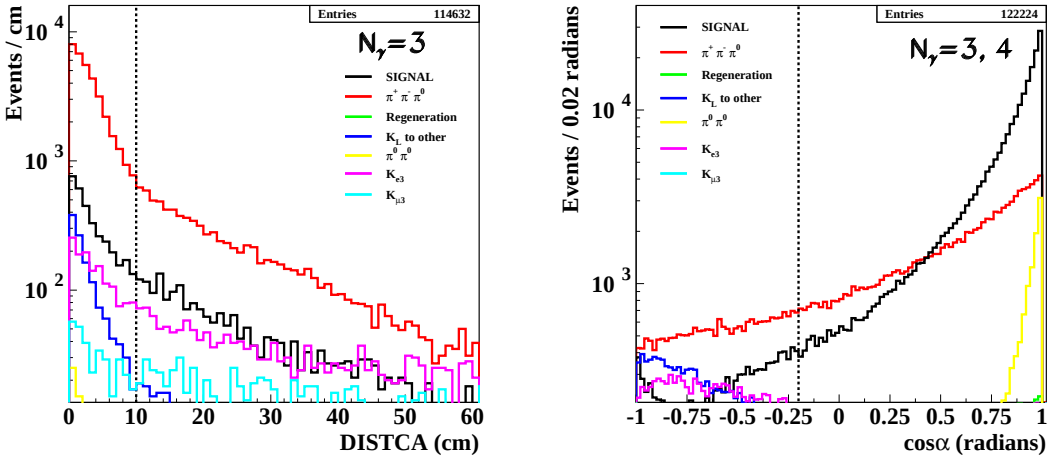

Figure 6.3: **Left**: Monte Carlo distribution of d_{PCA} variable with all background components for events with $N_\gamma = 3$; only events with $d_{PCA} > 10$ cm are retained. **Right**: Monte Carlo distribution of $\cos\alpha$ variable with all background components for events with $N_\gamma = 3$ and 4; events on the left of the black line are rejected.

K_L decay or process	ε (%) $N_\gamma \geq 3$ in the FV	ε (%) $N_\gamma = 3$ after RMS cut	ε (%) $N_\gamma = 3$ after $\cos\theta_{avg}$ cut
$K_L \to \pi^0\pi^0\pi^0$	99.08 ± 0.08	98.91 ± 0.08	98.89 ± 0.08
$K_L \to \pi^+\pi^-\pi^0$	7.56 ± 0.02	2.71 ± 0.01	2.55 ± 0.01
$K_L \to K_S \to \pi^0\pi^0$	34.66 ± 0.45	31.62 ± 0.42	31.07 ± 0.42
$K_L \to \pi^0\pi^0$	95.90 ± 1.17	94.48 ± 1.17	93.91 ± 1.17
$K_L \to \pi^\pm e^\mp \nu$	0.372 ± 0.003	0.113 ± 0.001	0.087 ± 0.001
$K_L \to \pi^\pm \mu^\mp \nu$	0.218 ± 0.002	0.066 ± 0.001	0.050 ± 0.001
$K_L \to other$	13.33 ± 0.11	7.27 ± 0.07	6.37 ± 0.07

Table 6.2: Reconstruction efficiency from Monte Carlo for each K_L process after the FV, RMS and $\cos\theta_{avg}$ cuts.

$K_L \to other$ have a peak at $\cos\alpha = -1$, that corresponds to backscattering of the products of K_L nuclear interactions with the drift chamber or calorimeter material. To reject the nuclear interaction background, only events with $\cos\alpha > -0.2$ are selected, for $N_\gamma = 3$ and 4.

Tab. 6.3 shows Monte Carlo reconstruction efficiencies for signal and background after the cuts on d_{PCA} and $\cos\alpha$ variables.

Finally, Tab. 6.4 shows a summary of the background composition after the cuts, to be compared with Tab. 6.1.

6.2 Nuclear interactions

The simulation of $\Lambda\pi$ and $\Sigma\pi$ production in K_L nuclear interactions with the detector materials has been also verified using a data sample. To calibrate the Monte Carlo

K_L decay or process	ε (%) $N_\gamma = 3$ after d_{PCA} cut	ε (%) $N_\gamma \leq 4$ after $\cos\alpha$ cut
$K_L \to \pi^0\pi^0\pi^0$	98.73 ± 0.08	98.39 ± 0.08
$K_L \to \pi^+\pi^-\pi^0$	1.010 ± 0.007	0.826 ± 0.007
$K_L \to K_S \to \pi^0\pi^0$	30.81 ± 0.41	29.11 ± 0.40
$K_L \to \pi^0\pi^0$	93.03 ± 1.16	92.47 ± 1.16
$K_L \to \pi^\pm e^\mp \nu$	0.076 ± 0.001	0.0414 ± 0.0008
$K_L \to \pi^\pm \mu^\mp \nu$	0.047 ± 0.001	0.0225 ± 0.0008
$K_L \to other$	4.82 ± 0.06	2.27 ± 0.04

Table 6.3: Reconstruction efficiency from Monte Carlo for each K_L process after d_{PCA} and $\cos\alpha$ cuts for events with $N_\gamma = 3,\ 4$.

K_L decay or process	$N_\gamma \geq 3$ $B/(S+B)$	$N_\gamma = 3$ $B/(S+B)$	$N_\gamma = 4$ $B/(S+B)$	$N_\gamma \geq 5$ $B/(S+B)$
All backgrounds	1.72 %	54.03 %	9.58 %	0.111 %
$K_L \to \pi^+\pi^-\pi^0$	0.85 %	37.69 %	2.71 %	0.025 %
$K_L \to K_S \to \pi^0\pi^0$	0.23 %	3.29 %	2.11 %	0.012 %
$K_L \to \pi^0\pi^0$	0.41 %	5.70 %	3.95 %	0.020 %
$K_L \to \pi^\pm e^\mp \nu$	0.09 %	3.31 %	0.35 %	0.008 %
$K_L \to \pi^\pm \mu^\mp \nu$	0.03 %	1.11 %	0.12 %	0.003 %
$K_L \to other$	0.11 %	2.92 %	0.34 %	0.043 %

Table 6.4: Background contamination $B/(S+B)$ in the fiducial volume for $N_\gamma \geq 3$, $N_\gamma = 3$ and $N_\gamma = 4$ events after the cuts. No cuts have been applied on $N_\gamma \geq 5$ events, so the background percentage is unchanged.

amount of nuclear interactions in different detector areas, six regions have been defined:

$$\begin{aligned} 0 \text{ cm} &< R < 35 \text{ cm} \\ 35 \text{ cm} &< R < 100 \text{ cm} \\ 100 \text{ cm} &< R < 150 \text{ cm} \\ 150 \text{ cm} &< R < 190 \text{ cm} \\ 190 \text{ cm} &< R < 210 \text{ cm} \\ R &> 210 \text{ cm} , \end{aligned} \tag{6.4}$$

where $R = \sqrt{x^2 + y^2 + z^2}$ and $(x,\ y,\ z)$ are the coordinates of the K_L multiphoton vertex.

All the $\cos\alpha$ distributions for data and two different Monte Carlo samples have been compared for each of the six detector regions as shown in Fig. 6.4 for events with $N_\gamma = 3,\ 4$.

One Monte Carlo sample includes all K_L processes (decays and interactions), while the nuclear interactions are not included in the second sample.

The K_L nuclear interactions with the internal wall of the drift chamber and with the beam pipe ($0 < R < 35$ cm) are significantly overestimated in the Monte

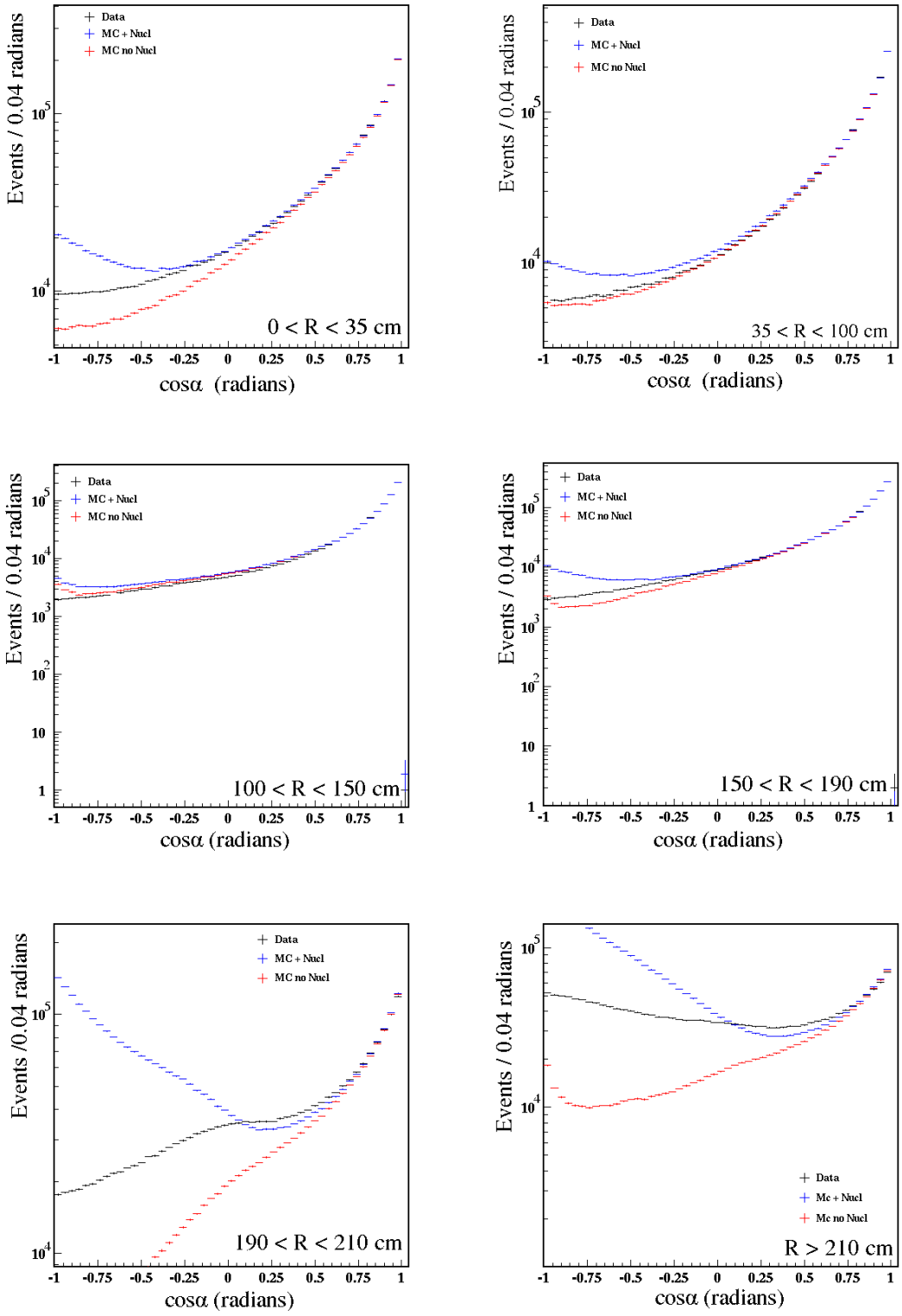

Figure 6.4: Distributions of $\cos\alpha$ variable for events with $N_\gamma = 3,\ 4$ in six different regions of the calorimeter from top to bottom, from left to right: $R \in (0, 35)$; $(35, 100)$; $(100, 150)$; $(150, 190)$; $(190, 210)$; $(210, \infty)$. Black point are used for data, red for the Monte Carlo without nuclear interactions and blue for the Monte Carlo including nuclear interactions.

Carlo. The more one approaches the fiducial volume ($35 < R < 150$ cm), the more the nuclear interactions amount reduces and the three distributions reach a similar shape.

The largest discrepancy is observed for large R values, outside the fiducial volume used in this analysis. As it is clear from the distributions, the data sample shape lies between the Monte Carlo sample including and not including nuclear interactions. This disagreement is due to the inaccurate simulation of kaons inelastic scattering processes in GHEISHA (see Sec. 3.7).

The nuclear interactions overestimation in the Monte Carlo can be assessed by comparing the difference between data and Monte Carlo without nuclear interactions with the Monte Carlo nuclear interactions provided by the simulation. Data and Monte Carlo samples are normalized requiring the same number of events in the region $\cos\alpha > 0.9$, where the amount of nuclear interactions is negligible.

Fig. 6.5 on the left side shows the difference between data - Monte Carlo without nuclear interactions and the Monte Carlo simulation of nuclear interactions for $\cos\alpha$ in different detector regions. In the regions $35 < R < 150$ cm there is a very small amount of material, therefore nuclear interactions are strongly suppressed. In fact, the data - Monte Carlo difference inside these regions gives negative results, because the Monte Carlo probably overestimates the effect of regeneration on drift chamber wires and gas, too.

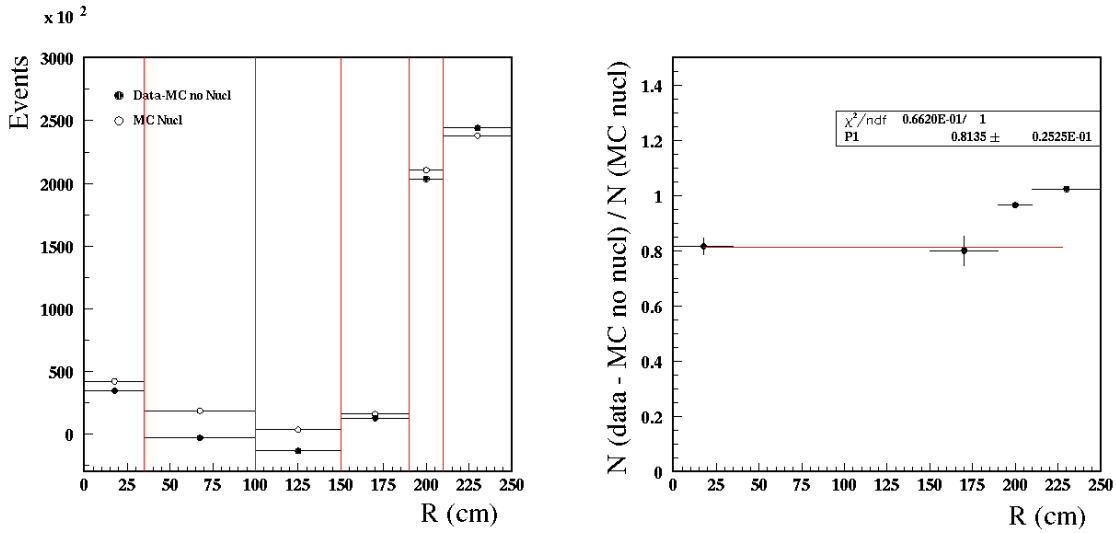

Figure 6.5: **Left**: Comparison between the $\cos\alpha$ distribution for data - Monte Carlo without nuclear interactions difference (black dots) and the $\cos\alpha$ distribution for nuclear interactions simulated from Monte Carlo (white dots), for six different regions of the detector. **Right**: Fit with a constant parameter to the weighted average of the ratio bin-by-bin of data - Monte Carlo without nuclear interactions distribution over the nuclear interactions distribution from Monte Carlo, for the two border regions of the fiducial volume.

To correct the amount of nuclear interactions simulated in the fiducial volume, the ratio $N(data - MC_{no\,nucl})/N(MC_{nucl})$ has been used; it has been measured in two contiguous regions, supposing that the same scale factor approximately holds also inside the drift chamber volume.

The fit function used to compare the ratio of these distributions is a weighted average of the ratios in the border regions of the fiducial volume. The fit result is shown in Fig. 6.5 on the right side, and its value is:

$$\xi = \frac{\left(\frac{N(data-MC_{no\,nucl})}{N(MC_{nucl})} \cdot \zeta_1|_{R_{35}} + \frac{N(data-MC_{no\,nucl})}{N(MC_{nucl})} \cdot \zeta_2|_{R_{150}}\right)}{\zeta_1 + \zeta_2} = 0.813 \pm 0.025 \qquad (6.5)$$

with ζ_1 and ζ_2 are the errors of the ratios $N(data - MC_{no\,nucl})/N(MC_{nucl})$.

6.3 $K_L \to K_S$ regeneration

In the Monte Carlo the cross section for $K_L \to K_S$ regeneration is modeled according to theoretical assumptions and there are few measurements with 110 MeV/c kaons limited to few nuclei. Then the amount of Monte Carlo $K_L \to K_S$ regeneration has been normalized to what observed in the data selecting $K_L \to K_S \to \pi^+\pi^-$ processes.

For each K_L vertex reconstructed with with two tracks of opposite curvature, the two-track invariant mass ($M_{\rm inv}$) has been evaluated:

$$M^2_{\rm inv} = E^2_{tot} - |\vec{p}_{tot}|^2 \qquad (6.6)$$

with the hypothesis of the charged pion mass:

$$\begin{aligned} \vec{p}_{tot} &= \vec{p}_{\pi^+} + \vec{p}_{\pi^-} \\ E_{tot} &= E_{\pi^+} + E_{\pi^-} = \sqrt{\vec{p}^2_{\pi^+} + M^2_\pi} + \sqrt{\vec{p}^2_{\pi^-} + M^2_\pi} \end{aligned} \qquad (6.7)$$

(see Fig. 6.6 on the left side).

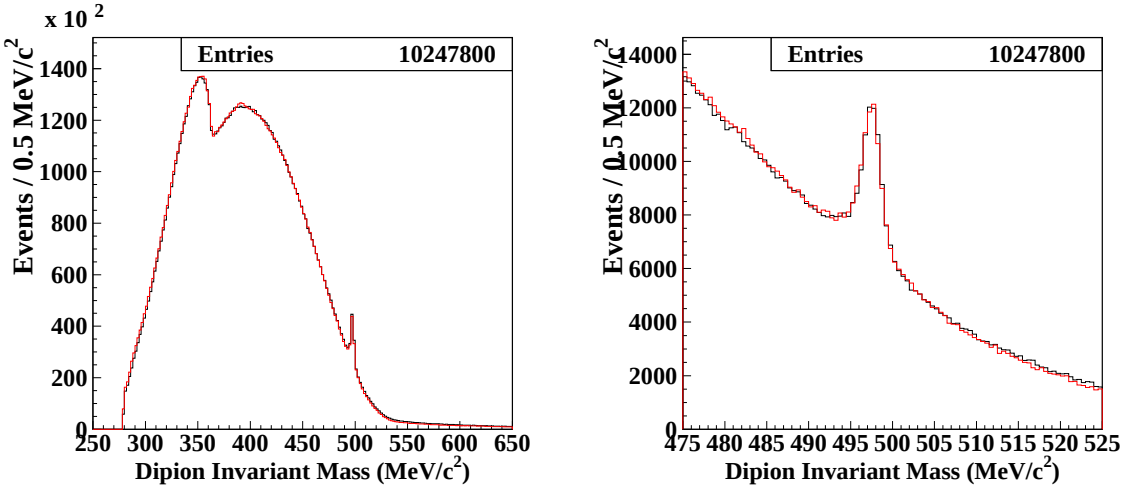

Figure 6.6: Distribution of the invariant mass associated to decay vertices made of two tracks of opposite curvature, in the pion mass hypothesis. Data and Monte Carlo refer to the 2005 run period n.3. Black is data, red is Monte Carlo. **Left**: Full $M_{\rm inv}$ range. **Right**: Zoom in the $M_{\rm inv} \sim M_{K^0}$ region.

The invariant mass for $K_L \to K_S \to \pi^+\pi^-$ regeneration events is expected to be $M_{\rm inv} \sim M_{K^0}$, so the regeneration events are selected requiring an invariant mass within 5 MeV from the kaon mass (see Fig. 6.6 on the right side):

$$|M_{\rm inv} - M_{K^0}| < 5 \text{ MeV}/c^2. \tag{6.8}$$

This requirement selects also the CP violating $K_L \to \pi^+\pi^-$ decays. The intensity of coherent regeneration is expected to be about 1000 times smaller than for incoherent regeneration. Therefore, the angular distribution of regenerated K_S mesons can be used to separate them from the $K_L \to \pi^+\pi^-$ decays by cutting in the scattering angle, the angle between the K_L direction and the K_S momentum, $\vec{p}_{\pi^+} + \vec{p}_{\pi^-}$ (see Fig. 6.7). A variable related to the scattering angle is used to select

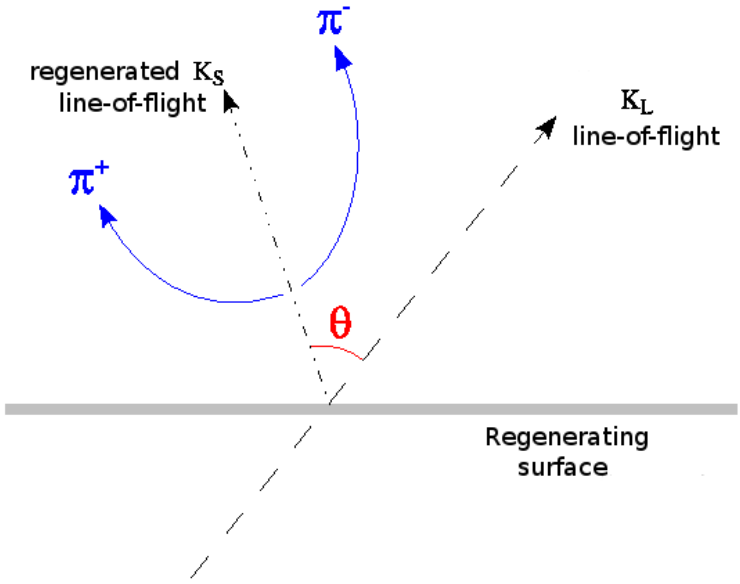

Figure 6.7: Scattering angle of a regeneration event.

the regenerated events, Q_{miss}:

$$Q_{miss} \equiv \sqrt{E^2_{miss} + |\vec{p}_{miss}|^2}, \tag{6.9}$$

where $\vec{p}_{miss}$ and E_{miss} are computed from the K_L momentum (from tagging) and the momenta of the two tracks, and E_{miss} is calculated in the charged pion mass hypothesis (see Fig. 6.8 on the left side). The $K_L \to \pi^+\pi^-$ decays are concentrated in the low Q_{miss} region (see Fig. 6.8 on the right side), so another cut is applied to reject this background:

$$Q_{miss} > 10 \text{ MeV}. \tag{6.10}$$

Then the transverse radius (Fig. 6.9) of the two-track K_L decay vertex has been reconstructed for this sample enriched in regeneration events. Two peaks arise, one on the spherical beam pipe at $R \sim 10$ cm and one on the internal wall of the DC at $R_T \sim 25$ cm. As clearly visible from the plot, the Monte Carlo reproduces only the shape of the peaks, but not the number of events, so it has been necessary to evaluate a correction.

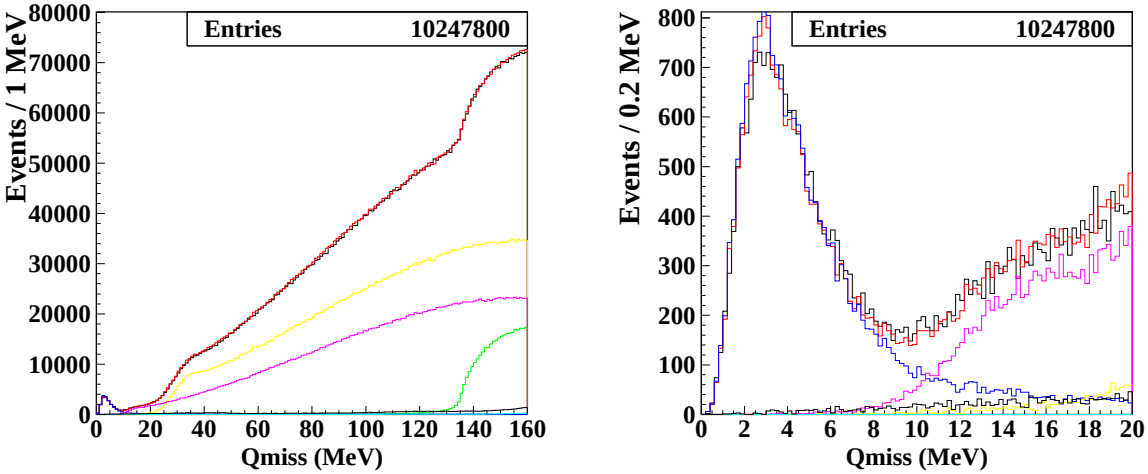

Figure 6.8: Distribution of Q_{miss} for data and for all decays from Monte Carlo. Data and Monte Carlo refer to the 2005 run period n.3. Black is data, red is the sum of all Monte Carlo simulated events, green for $K_L \to \pi^+\pi^-\pi^0$, blue for $K_L \to \pi^+\pi^-$ CP violating decays, yellow and purple respectively for K_{e3} and $K_{\mu 3}$ K_L semileptonic decays, pale blue for $3\pi^0$ decays and black for nuclear interactions. **Left**: Wide range. **Right**: Zoom on Q_{miss} variable in the region populated by $K_L \to \pi^+\pi^-$ CP violating decays.

A fit has been performed to the R_T distribution in the range [15,40] cm, near the internal wall of the drift chamber ($R_T \sim 25$ cm), after Monte Carlo background subtraction from data, using a two-gaussian function.

A scaling factor of (0.46 ± 0.01) has been obtained from the ratio between the integral of the fitted regeneration peak and the number of MC regeneration events reconstructed in that region.

6.4 Nuclear interaction effects on the K_L lifetime

K_L nuclear interactions with the material inside the drift chamber bias the lifetime measurement since they modify the rate of K_L vertices. In fact, the decrease in the number of K_L passing from L to $L + dL$ is given by:

$$N(L + dL) - N(L) = -N(L) \cdot \left(\frac{1}{\lambda_L} + \frac{1}{\lambda_I}\right) \cdot dL \tag{6.11}$$

or:

$$N(L) = N(0) \cdot e^{-L/\lambda_{exp}} \tag{6.12}$$

where:

$$\lambda_{exp} = \frac{\lambda_I \lambda_L}{\lambda_I + \lambda_L} \simeq \lambda_L \left(1 - \frac{\lambda_L}{\lambda_I}\right) \tag{6.13}$$

and λ_L is the K_L mean decay length, $\lambda_I = A/N_A \rho(L) \sigma_I$, A is the atomic weight and N_A is the Avogadro constant, $\rho(L)$ the material density and σ_I the nuclear interaction cross section.

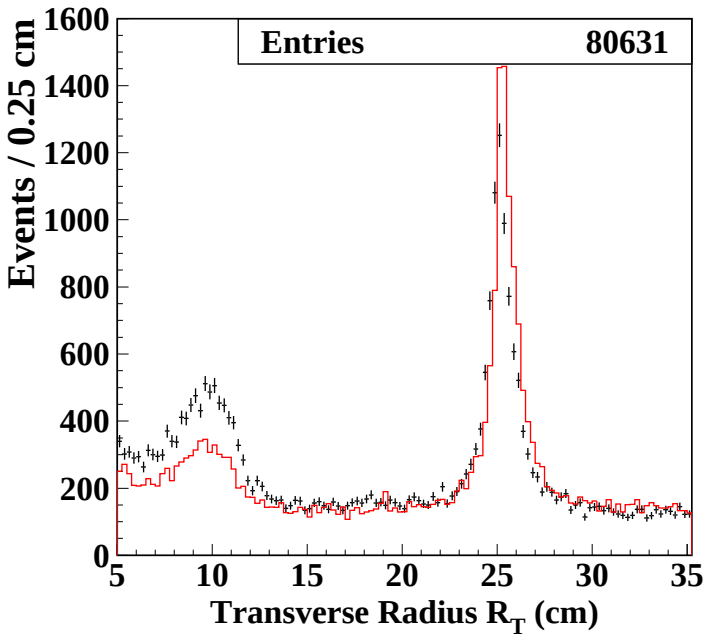

Figure 6.9: Distribution of the transverse radius for the decay vertex, black points are used for data and red line for the Monte Carlo. Two peaks are clearly visible, corresponding to the spherical beam pipe at $R \sim 10$ cm and the internal wall of the DC at $R_T \sim 25$ cm.

The dominant nuclear interaction processes, $K_L \to K_S$ regeneration, $\bar{K}^0 N \to \Sigma\pi$ and $\bar{K}^0 N \to \Lambda\pi$, are simulated in the Monte Carlo. Since the cross sections of the three type of processes are not well known, their rates have been measured from data (see Ref. [42] and previous sections), and the simulated events have been weighted accordingly.

In data the sum of all the nuclear interactions amounts to $\sim$0.33% with a conservative error of 50%, (0.33$\pm$0.16)%. This value has been taken into account to correct the K_L lifetime. For instance, a correction of + 0.165 ns has to be applied to a K_L lifetime of 50 ns.

Chapter 7

Fit results and errors

7.1 Fit to the K_L proper time distribution

The K_L proper time, t^*, is obtained for each event by dividing the K_L decay length L_K for $\beta\gamma$ of the K_L meson:

$$t^* = \frac{L_K}{\beta\gamma c} \tag{7.1}$$

Then fit to the proper time distribution is done to extract the K_L lifetime value. For this, a sample of K_L decays as clean as possible and free from distortions is needed. Ideally, the number of $K_L \to \pi^0\pi^0\pi^0$ decays, $N_{3\pi^0}$, is:

$$N_{3\pi^0}(t^*) = N_{3\pi^0}(t^* = 0) \cdot e^{-t^*/\tau_L} = N_{3\pi^0}(L_K = 0) \cdot e^{-L_K/\lambda_L} = N_{3\pi^0}(L_K) \tag{7.2}$$

After all selections, one finds:

$$N_{3\pi^0}(L_K) = N_{3\pi^0}(L_K = 0) \cdot \int f(L'_K) \cdot e^{-L'_K/\lambda'_L} \cdot g(L_K - L'_K)\, dL'_K + N_{bckg}(L_K) \tag{7.3}$$

where:

- $N_{bckg}(L_K)$ is the residual background after the selection cuts; Monte Carlo shapes for the background will be used bin-by-bin in the fit, adjusted by a scaling factor introduced as a fit parameter;
- $f(L'_K)$ is the signal efficiency function; it is evaluated from the Monte Carlo after tuning it with the ratio $\varepsilon_{data}/\varepsilon_{MC}$ for the single photon neutral vertex reconstruction efficiency;
- $g(L_K - L'_K)$ is the vertex resolution function, its effect on the lifetime is negligible;
- λ' is the effective average decay length, taking into account also the K_L nuclear interactions with the drift chamber material.

These experimental effects introduce a distortion in the proper time distribution, and must be accurately taken into account in the method to extract the result. The accuracy in the knowledge of these effects is included in the systematic error.

7.1.1 The background

The residual background, after the selection cuts discussed in Chap. 6, has been estimated with the Monte Carlo.

Since there is a difference between the number of K_L mesons after the tagging procedure obtained in data compared to the Monte Carlo, the latter needs to be normalized with the following scale factor:

$$\zeta = \frac{N_{data}(FV)}{N_{MC}^{sig}(FV) + N_{MC}^{bckg}(FV)}, \tag{7.4}$$

where $N_{data}(FV)$ is the number of data events reconstructed in the fiducial volume, $N_{MC}^{sig}(FV)$ is the number of $K_L \to \pi^0\pi^0\pi^0$ events from the Monte Carlo reconstructed in the fiducial volume, and $N_{MC}^{bckg}(FV)$ is the total number of Monte Carlo background events reconstructed in the fiducial volume.

The Monte Carlo background component due to K_L nuclear interactions with detector materials, $K_L \to \Lambda\pi$, $\Sigma\pi$, has previously been scaled with a factor $\xi = 0.81$ (see Sec. 6.2) to be used for evaluating the ζ factor.

Fig.7.1 shows the L_K and t^* distributions for data (black dots) and normalized Monte Carlo (red histogram).

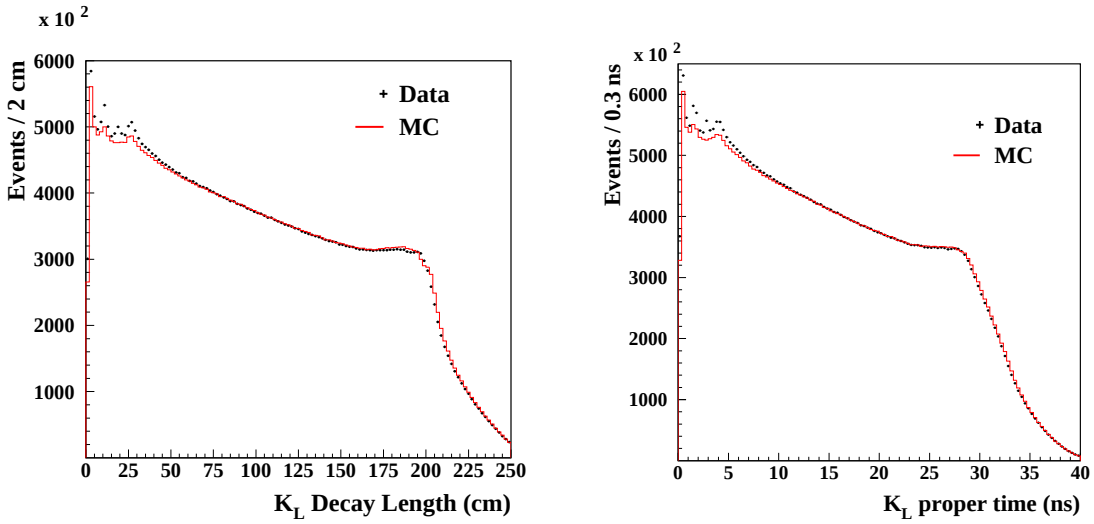

Figure 7.1: K_L decay length L_K (**left**) and proper time t^* (**right**) distributions including all 2005 statistics. Black dots are used for data, red histogram is used for all the MC (signal + background).

Fig.7.2 shows the L_K and t^* distributions for data (black dots) and normalized Monte Carlo (black histogram) with background contributions separately shown and added to the signal.

There is a good agreement between the data and Monte Carlo distributions in the fiducial volume. The dominant background contribution comes from $K_L \to \pi^+\pi^-\pi^0$ decays, and, to a smaller degree, from $K_L \to K_S$ regeneration and K_L nuclear interactions. The background shapes from Monte Carlo are used in the fit function, scaled by a general weighting factor, which will be extracted as one of the fit parameters.

Fig. 7.3 shows the relative weights of the relevant background contributions.

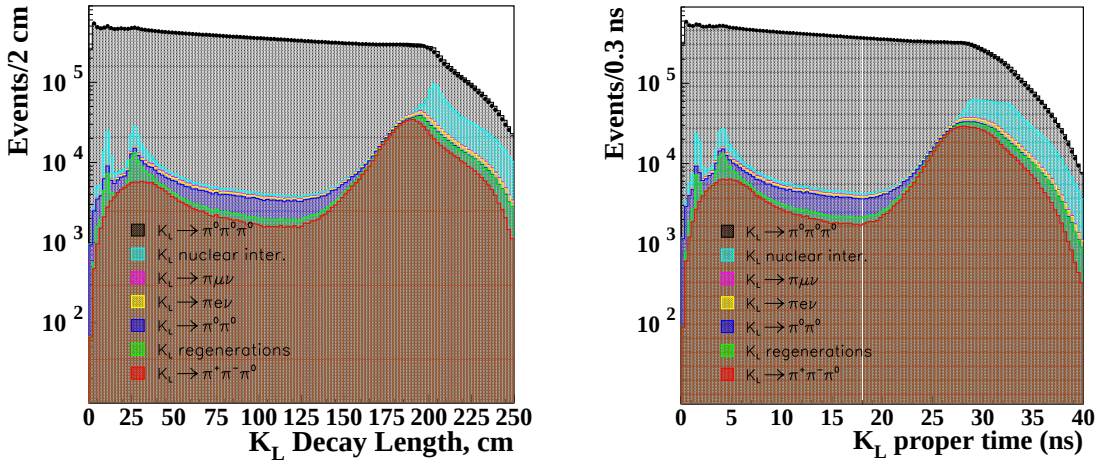

Figure 7.2: K_L decay length L_K (**left**) and proper time t^* (**right**) distributions including all 2005 statistics. Black dots are used for data, black histogram is used for all the MC (signal + background). Different components are gradually added: red area corresponds to $K_L \to \pi^+\pi^-\pi^0$, green after adding $K_L \to K_S$ regeneration, blue after adding $K_L \to \pi^0\pi^0$, yellow after adding $K_L \to \pi^\pm e^\mp \nu$, purple after adding $K_L \to \pi^\pm \mu^\mp \nu$, and finally pale blue for all the background components including the nuclear interactions rescaled by a factor 0.81.

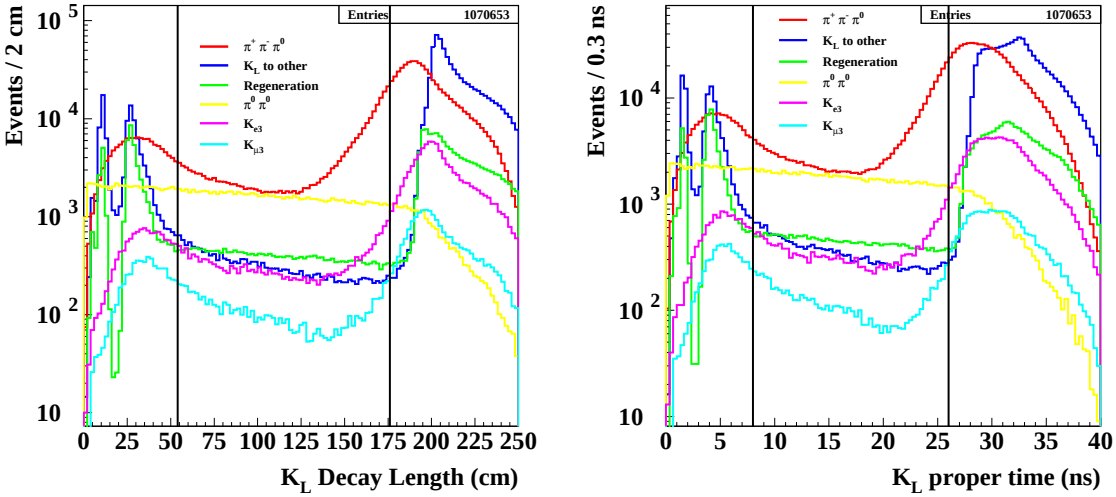

Figure 7.3: K_L decay length L_K (**left**) and proper time t^* (**right**) distributions for the dominant backgrounds to the $K_L \to \pi^0\pi^0\pi^0$ signal in their proportions: $K_L \to \pi^+\pi^-\pi^0$ in red, $K_L \to K_S$ regeneration in green and blue for K_L nuclear interactions. The fit range is labeled with two black lines.

For $t^* < 8$ and $t^* > 26$ ns, the main sources of background are $K_L \to \pi^+\pi^-\pi^0$ and nuclear interactions; the latters are only approximately reproduced by the Monte Carlo. Therefore it is more safe to exclude these regions from the fit.

7.1.2 Efficiency

The signal selection efficiency as a function of the decay length and the proper time is evaluated from the Monte Carlo by dividing the number of simulated $K_L \to \pi^0\pi^0\pi^0$ events after all cuts (described in Sec. 6.1) by the number of simulated $K_L \to \pi^0\pi^0\pi^0$ events after the tagging procedure:

$$\varepsilon = \frac{N^{MC}_{sig\ after\ all\ cuts}}{N^{MC}_{sig\ after\ tag}}. \tag{7.5}$$

The efficiency (7.5) includes the single-photon neutral vertex reconstruction efficiency, evaluated directly on data, by correcting the reconstructed L_K and t^* distributions with the ratio $\varepsilon_{data}/\varepsilon_{MC}$, using a hit or miss method, as described in 5.3.2.

This efficiency has been studied as a function of L_K and t^*. It is clear that in calculating the ratio (7.5) only the generated L_K (or t^*) can be considered because the number of events in the denominator is counted before the K_L reconstruction.

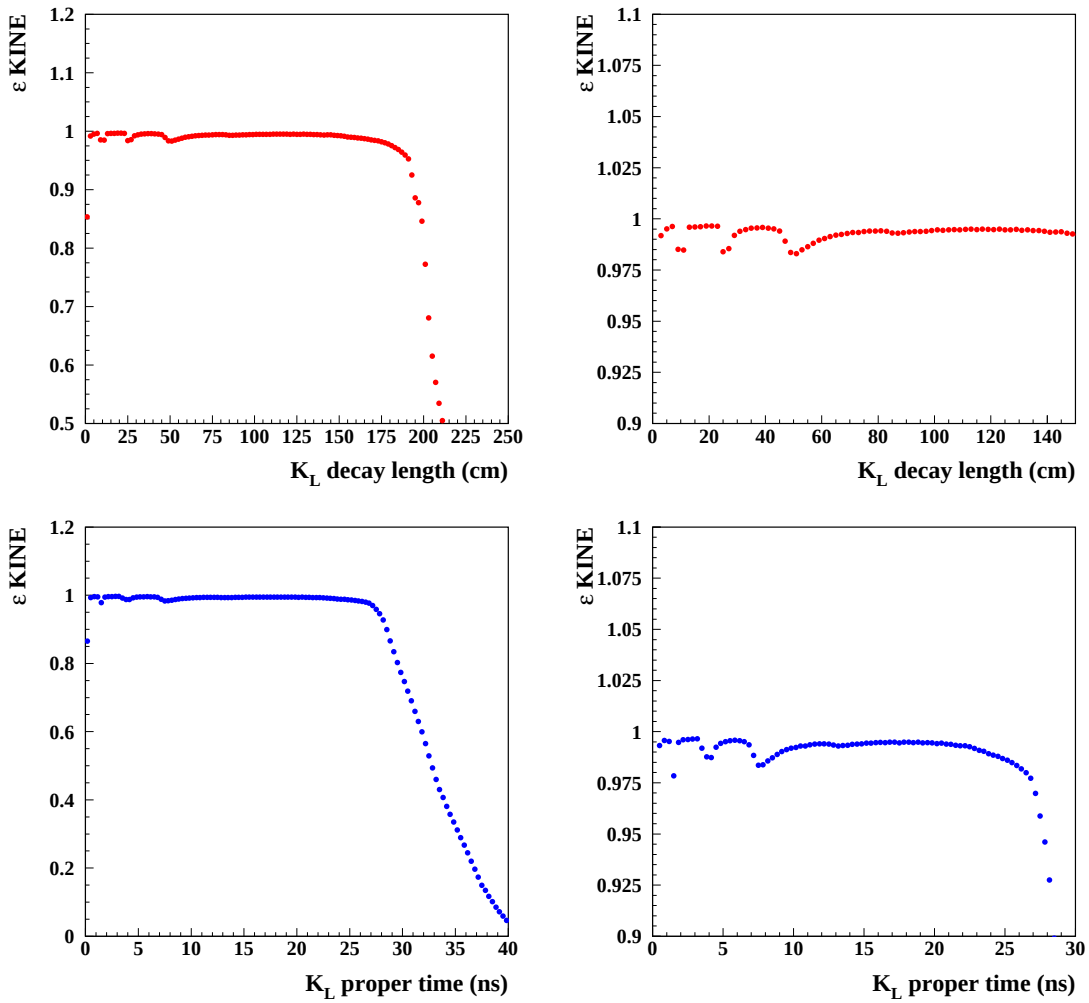

Figure 7.4: **Top left**: Monte Carlo efficiency as a function of the decay length, zoomed in the **top right** plot. **Bottom left**: Monte Carlo efficiency as a function of the proper time, zoomed in the **bottom right** plot.

A smearing matrix can be evaluated to "translate" such $\varepsilon(L_K^{gen})$ into $\varepsilon(L_K^{rec})$, to include the neutral vertex spatial resolution effects. However, since the neutral vertex resolution (∼2 cm) is much smaller than the K_L decay length (∼330 cm), the smearing effect is negligible for the lifetime fit, as demonstrated by a numerical model.

As shown in Fig. 7.4, three deeps are clearly visible in the efficiency distributions, for small values of L_K or t^*.

The deep at L_K∼10 cm (t^*∼1.5 ns) corresponds to the beam pipe, at L_K∼25 cm (t^*∼4 ns) to the internal wall of the drift chamber, and the deep at L_K∼50 cm (t^*∼7.5 ns) is due to photons absorption in the calorimeters around the quadrupoles (see Fig. 3.3), since the QCAL information has not been used in this analysis.

To decrease the effect induced by photon absorption in the QCAL, a cut has been applied on the cosine of the K_L emission polar angle ($\cos\theta_K$). The cone obscured by QCAL corresponds to a K_L polar angle equal to 0.37 radians. To reject most of the events that suffer of photon losses, it is necessary to apply a tighter angular cut, $\theta_K > 0.7$ rad, as shown in Fig. 7.5.

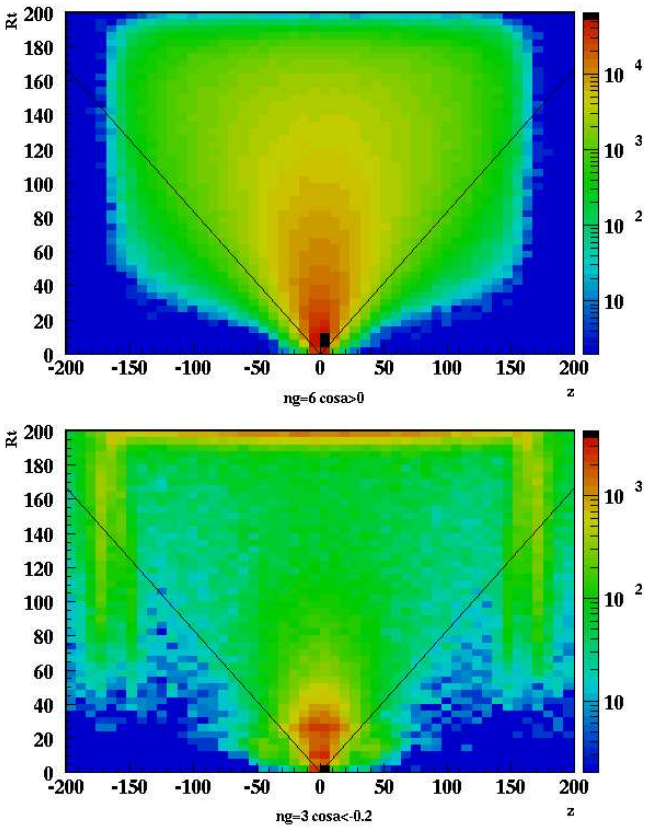

Figure 7.5: Data distribution of $R_T \times z$ for the neutral vertex position. **Top**: Distribution for $N_\gamma = 6$ with the cut $\cos\alpha > 0$ (99.98% of simulated $K_L \to \pi^0\pi^0\pi^0$ decays are retained). **Bottom**: Distribution for $N_\gamma = 3$ with the cut $\cos\alpha >$ -0.2 (background components from Monte Carlo: 79.7% of nuclear interactions, 8% of $K_L \to \pi^+\pi^-\pi^0$ decays, 5% of K_L semileptonic decays).

The figure shows the K_L neutral vertex position (R_T vs. z) for two data subsamples: in the upper part the signal is predominant ($N_\gamma = 6$ with $\cos\alpha > 0$ cut), and in the lower part the nuclear interactions are prevalent ($N_\gamma = 3$ with $\cos\alpha > 0.2$). The abundance of nuclear interactions is clearly visible in the QCAL region: $z = \pm 50$ cm and $R_T = 10 \div 15$ cm. This θ_K cut rejects $\sim$7% of events.

In fact, the Monte Carlo reconstruction and selection efficiency after the $\cos\theta_K$ cut

$$\varepsilon_{\cos\theta_K\ cut} = \frac{N^{MC}_{sig,\ \cos\theta_K\ cut}}{N^{MC}_{sig,\ after\ tag,\ \cos\theta_K\ cut}} \tag{7.6}$$

does not show any deep in the QCAL region, as clearly visible in Fig. 7.6, where only the deeps related to beam pipe and internal wall of the drift chamber are left. These deeps are due to a bad event reconstruction or to pair produced by the photons on the detector material. In equation (7.6) $N^{MC}_{sig,\ \cos\theta_K\ cut}$ is the number of $K_L \to \pi^0\pi^0\pi^0$ simulated events that are reconstructed, selected after the cuts described in Sec. 6.1 and have $\cos\theta_K < 0.7$, while $N^{MC}_{sig,\ after\ tag,\ \cos\theta_K\ cut}$ is the number of $K_L \to \pi^0\pi^0\pi^0$ simulated events that are retained after the tagging procedure and the $\cos\theta_K < 0.77$ cut). Therefore, the event reconstruction procedure in the selected angular region is not affected by the acceptance limitation due to QCAL.

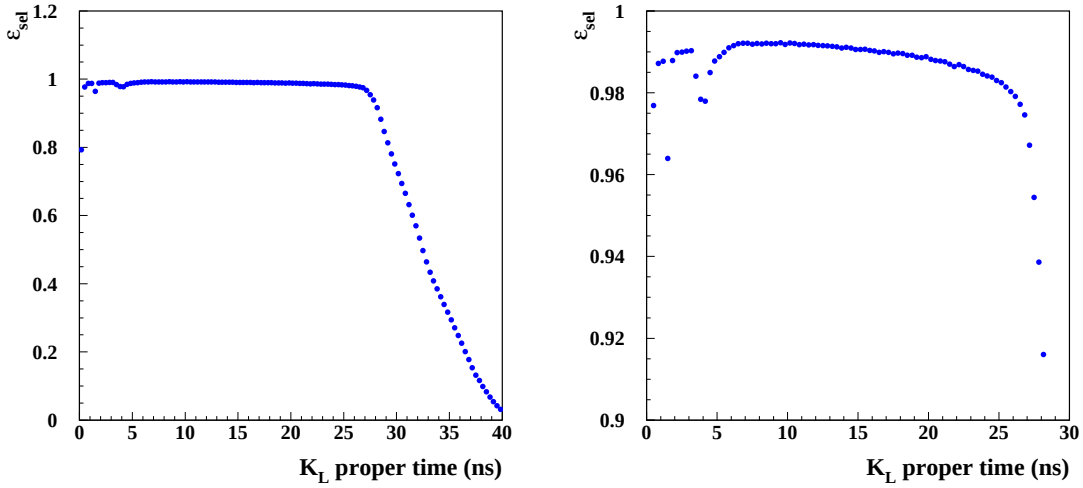

Figure 7.6: **Left**: signal selection efficiency from Monte Carlo as a function of the proper time after the cut $\cos\theta_K < 0.77$, zoomed in the plot on the **right** side.

This heterogeneity of the detector acceptance has been studied, to trace it through all the steps of the analysis. To this purpose, the ratio between the number of events retained after the tagging procedure and the $\cos\theta_K$ cut, and the number of events that satisfy the tag requirement has been evaluated as a function of the generated proper time, only for the dominant K_L decay modes. Fig. 7.7 shows the above mentioned ratio for main K_L decay modes simulated by the Monte Carlo: the trend reproduces all the distortions currently found in the Monte Carlo efficiency. A deep around $t^*\sim$7.5 ns is clearly visible, that corresponds to the QCAL region. The shape for high values of t^* is due to the calorimeter internal wall.

Since this study is entirely based on variables generated by the Monte Carlo, it is clear that the observed distortions have nothing to do with the reconstruction, but they solely reflect the detector geometrical acceptance, as proven by the trend that is identical for all K_L decay modes. It is then possible to derive a lifetime measurement by restricting *a priori* (before the tagging) the detector acceptance to $\cos\theta_K < 0.77$; thus avoiding the region with the efficiency discontinuity.

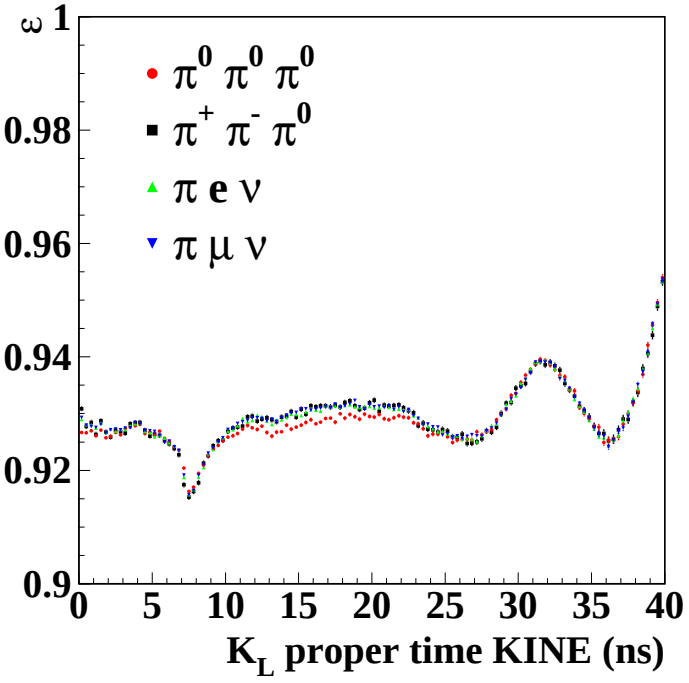

Figure 7.7: Ratio of the number of events selected after the tagging procedure and the $\cos\theta_K$ cut to the number of events retained after the tagging procedure; from Monte Carlo.

7.1.3 Fit method and K_L lifetime

The fit to the proper time distribution has been done including the Monte Carlo shape for the efficiency and the background in the following fit parameterization:

$$f(t^*) = N_0(3\pi^0)\ e^{-t^*/\tau}\ \varepsilon(t^*) + f_{\rm bck}\ B(t^*) \tag{7.7}$$

where the fit parameters to be extracted are $N_0(3\pi^0)$, the K_L lifetime τ and the Monte Carlo background scaling factor $f_{\rm bck}$, while ε is the signal efficiency and $B(t^*)$ is the bin content of the background shape from Monte Carlo.

A further check on the fit method has been carried out. A fit to the K_L lifetime has been performed using the Monte Carlo as a data sample, and the result, after applying all the due corrections, was compatible with the simulated τ value within the statistical error.

The proper time distribution (3 bins per nanosecond) obtained from the selected sample is shown in Fig. 7.8 (on the top), together with the fit result (the red thick solid line) in the range [8,26] ns. The statistical error of the Monte Carlo efficiency (∼0.1%) has been added in quadrature to the statistical fluctuation of each bin entry.

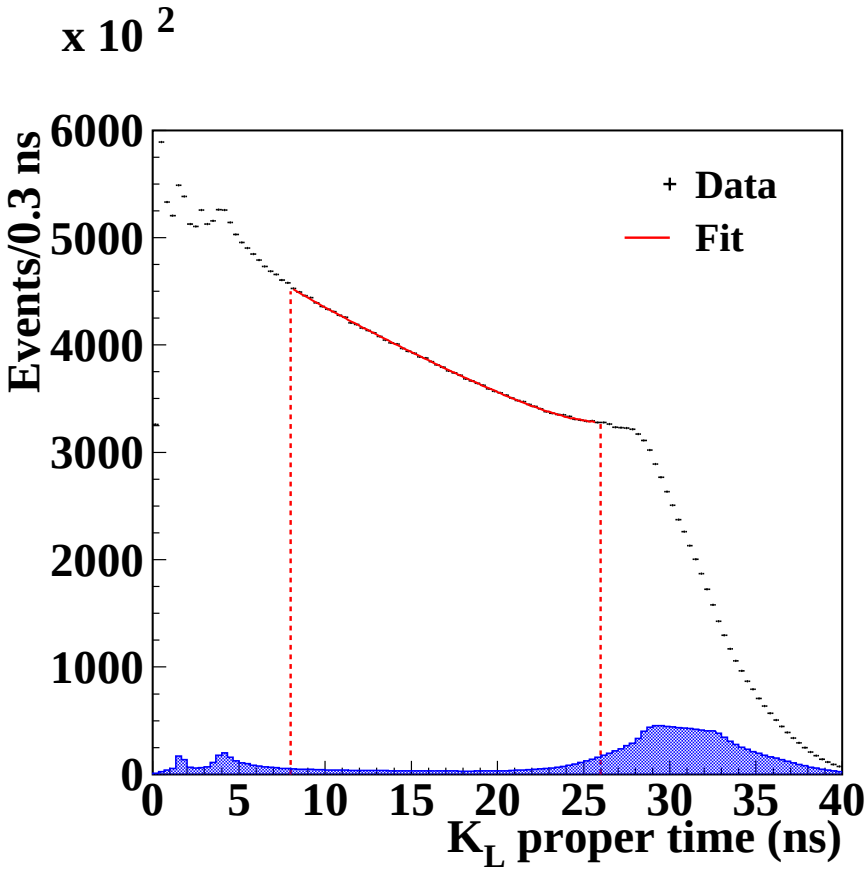

Figure 7.8: Fit to the K_L proper time distribution (3 bins per nanosecond) in the range [8,26] ns; the fit is shown as the thick solid red line, the background shape from Monte Carlo is the blue area.

The blue area represents the ∼1.72% residual background: the two peaks before 8 ns are due to regeneration events and nuclear interactions in the beam pipe and in the internal wall of the DC, while after 25 ns the background (essentially $K_L \to \pi^+\pi^-\pi^0$ decays) increases since we are approaching the limit of the fiducial volume limit, near the calorimeter. In the region [5,8] ns also a "beam loss" effect is present, because the regeneration and nuclear interaction events on the internal wall of the DC artificially decrease the number of K_L entering the fiducial volume. This effect has an apparent dependence on θ_K, because the DC wall is cylindrical while the L_K distribution is integrated over the polar angle range.

From 8 ns to lower times, the beam loss produces a fake increase of the exponential slope, but anyway this effect is negligible with respect to the background increase in the same region, shown in Fig. 7.3, due to mis-identification of regenera-

tion and nuclear interaction events as $K_L \to \pi^0\pi^0\pi^0$. The beam loss effect has been evaluated with a toy model and turns out to be essentially negligible with respect to the background induced by regeneration and nuclear interactions.

The result of the fit, obtained with ∼20 million events in the range [8,26] ns, is:

$$\tau = (51.06 \pm 0.14_{\text{stat}}) \text{ ns}. \tag{7.8}$$

with:

$$\chi^2/\text{ndf} = 50/54. \tag{7.9}$$

Fig. 7.9 shows the fit residuals (on the left side), essentially flat around zero, The pulls distribution shape (on the right side) is slightly asymmetrical, this is due

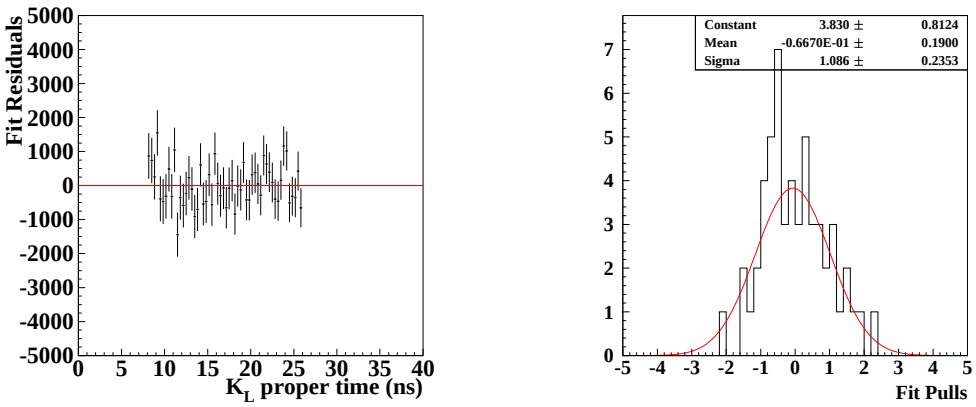

Figure 7.9: **Left**: Fit to the proper time residuals. **Right**: Fit pulls.

to the behaviour of the fit near the 8 ns border, where the background is basically regeneration and nuclear interactions, known from Monte Carlo with lower accuracy, as mentioned before.

7.2 Corrections and systematic errors

The systematic uncertainty is determined by the limited knowledge of

- the signal efficiency;
- the distribution of various background contributions used in the fit function;
- the absolute time scale;
- the cross section for nuclear interactions and K_L regeneration;

and by details concerning the fit to the proper time distribution.

7.2.1 Efficiency function

This analysis was done keeping the highest possible efficiency of the signal, in order to reduce to the minimum its variations over the decay length. In fact, for a lifetime measurement it isn't the efficiency absolute value that matters, but its uniformity on the whole time range used for the measurement. Hence, the systematic errors are related to the knowledge of the efficiency as a function of the proper time.

In the simplest case of an efficiency with a small linear dependence on t^*, $\varepsilon(t^*) = a + b\ t^*$, the resulting number $N(t^*)$ of K_L mesons, at a given t^*, is obtained in this way:

$$\begin{aligned} N(t^*) &= N_0\ e^{-t^*/\tau} \cdot \varepsilon(t^*) = N_0\ e^{-t^*/\tau} \cdot (a + b\ t^*) \simeq \\ &\simeq (N_0 \cdot a) \cdot e^{-t^*/\tau^*} \end{aligned}$$

with:

$$\tau^* \sim\ \tau \left[1 + \left(\frac{b}{a}\right) \tau\right]. \tag{7.10}$$

For instance, for $\tau \sim 50$ ns, if $(b/a) \sim 10^{-5}$/ns, we measure $\tau^* = 1.0005 \cdot \tau$, *i.e.* a 0.05% factor higher than the true value. Depending on the cases, the correction of this lifetime shift has to be done *a posteriori*, otherwise can be also included in data treatment.

Moreover, the statistical uncertainty of the a and b parameters introduces a systematic uncertainty in the knowledge of τ^* given by:

$$\frac{\delta\tau^*}{\tau^*} \sim \tau \times \frac{b}{a} \times \left(\frac{\delta b}{b} \oplus \frac{\delta a}{a}\right). \tag{7.11}$$

In this analysis the efficiency function is given by the convolution of three contributions:

$$\varepsilon = \varepsilon_{tag} \otimes \varepsilon_{rec} \otimes \varepsilon_{sel}, \tag{7.12}$$

hence it is needed to evaluate the corrections and the corresponding systematic uncertainties of the final result.

Tagging efficiency

The tagging efficiency as a function of t^* is shown in Fig 7.10. It is clearly different for the K_L decay modes, as previously discussed in Sec. 4.2.2.

The tagging efficiency $\varepsilon_{tag}(t^*)$ has been parameterized in the fiducial volume, only for signal, with a linear dependence on t^* with an intercept $a = (0.70469 \pm 0.00017)$ and a slope $b = (14.3 \pm 0.8)\ 10^{-5}$. From Eq. (7.10), the correction to the lifetime value is $(b/a) \cdot \tau$ = -1.01%, that applied to the value of Eq. (7.8), gives a correction of -0.51 ns with an error of ∼0.1%.

The $\varepsilon_{tag}(t^*)$ trend is due to the dependence of the trigger efficiency from the K_L decay vertex position in the fiducial volume, since the trigger thresholds are not equal in the various calorimeter zones, as described in Sec. 3.3. This condition, together with the requirement of at least one pion from the K_S decay being associated to a cluster with energy greater than 100 MeV, determines the observed trend. Its

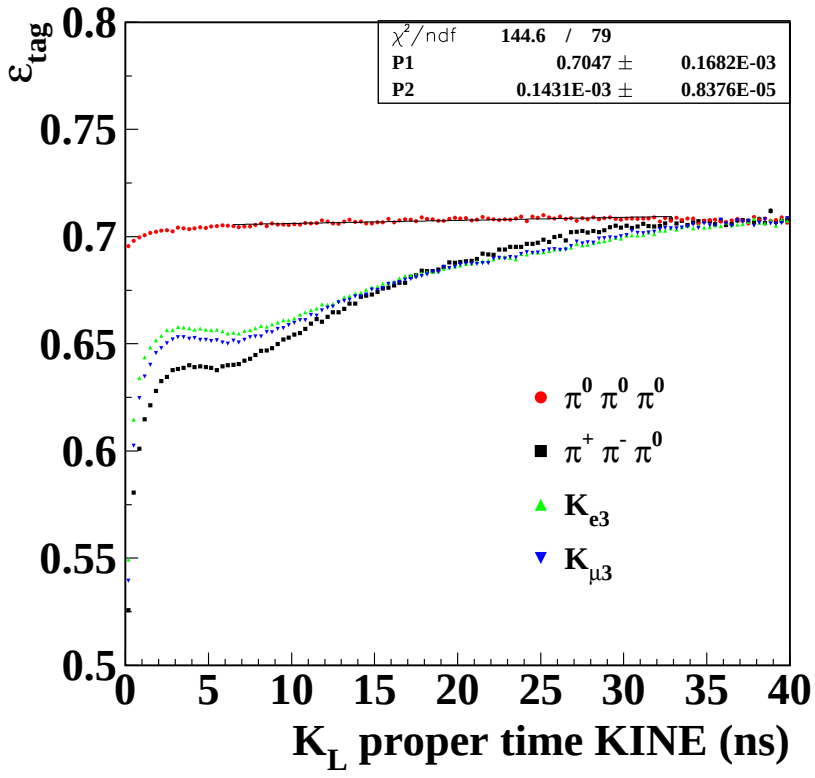

Figure 7.10: Tagging efficiency as a function of the proper time for the main K_L decay modes.

stability has been verified by varying in the analysis the energy threshold of $\pm 1\sigma$ using the calorimeter resolution of equation (3.9). The average variation of the correction obtained moving the threshold to 85 MeV and to 115 MeV is 0.16 ns, equal to a systematic error of 0.32%.

Reconstruction efficiency

The minimal requirements for a multiphoton vertex reconstruction is of at least three neutral clusters with energy E > 20 MeV connected with the same vertex within 5σ. The reconstruction efficiency of the single photon vertex has been studied with the data and corrected in the Monte Carlo before the multiphoton vertex reconstruction, as described in Sec. 5.4.1. With this technique, every possible distortion of the time distribution is automatically corrected in the efficiency evaluated with the Monte Carlo. The systematic error caused by the statistical error of this procedure to evaluate the data efficiency correction is negligible. This has been verified by moving all the correction factors by one standard deviation.

A more relevant effect comes from the uncertainty on photon threshold energy. The calorimeter resolution for a photon energy of 20 MeV is ∼7 MeV. By repeating the measurement with a threshold at 13 and at 27 MeV, a variation of the lifetime of 0.16% is obtained.

Signal selection efficiency

The selection cuts studied in section 6.1 have great impact on the background, but small effect on the signal efficiency. Moreover, these cuts have been applied only to events with $N_\gamma = 3$ and 4, that are a small fraction of the total number of events. The results of Table 6.2 and 6.3 imply that the cuts produce a total inefficiency of 0.7%.

Fig. 7.11 shows that the ratio ε(data)/ε(Monte Carlo) is constant for events almost background free, with $N_\gamma = 5$ and 6, with a RMS value of ∼0.6% in the fiducial volume. The ratio of efficiencies is the same for all values of multiplicity, N_γ, so it is possible to estimate a systematic uncertainty of the selection efficiency of 0.7%×0.6% = 4.2 $\times 10^{-5}$, completely negligible.

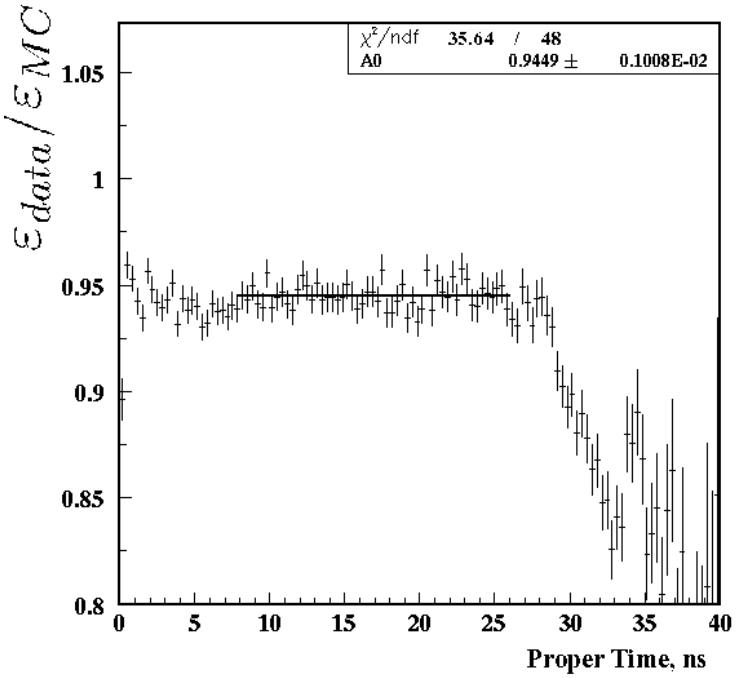

Figure 7.11: Ratio of Data to Monte Carlo signal efficiency for events with $N_\gamma = 5$ and 6 fitted with a constant.

7.2.2 Absolute time scale

In Sec. 5.3.1 we studied the difference between the K_L neutral vertex position reconstructed with the calorimeter, and the charged vertex position reconstructed with the drift chamber, using a control sample of $K_L \to \pi^+\pi^-\pi^0$ decays. In Fig. 5.7(d) it is clearly visible that the difference ΔR is not constant as a function of R_T: the increase for $R_T > 100$ cm there can be approximated by a parabola.

The effect of this mis-calibration of the absolute time scale has been evaluated with a "toy" Monte Carlo which convolutes the exponential decay function with the parabola extracted from the data. A systematic shift of -0.3% is obtained that will

be directly applied to the lifetime result. The systematic error introduced by this correction derives from the error of the parameters of the approximating parabola, and includes the systematic uncertainty on the K_L line of fight determination. Its value is 0.12%.

7.2.3 K_L nuclear interactions

As discussed in Sec. 6.4, the result has to be corrected for the effect of nuclear interactions and the regeneration in the fit region, that produce a fake increase of the decay rate, reducing the apparent lifetime.

The rate of the dominant nuclear interaction processes, $K_L \to K_S$ regeneration, $\bar{K}^0 N \to \Sigma\pi$ and $\bar{K}^0 N \to \Lambda\pi$, has been measured directly on data inside our fiducial volume, since the cross sections are not well reproduced.

It was found that the Monte Carlo overestimates these processes, therefore the simulation has been corrected accordingly.

In data the sum of all the nuclear interactions amounts to ∼0.33% with a conservative error of 50%, (0.33 ±0.16)%, that translates in a correction of + 0.17 ns to be applied to the K_L lifetime.

7.2.4 Fit range and binning

The stability of the result was studied by varying the t^* range of the fit. The lower and upper limits of were changed one at the time, keeping fixed the opposite limit to the nominal value (8 ns or 26 ns). A good stability is obtained as shown in Fig. 7.12 and the systematic error associated to the fit range can be considered negligible. The effect of the proper time distribution binning has been evaluated by repeating

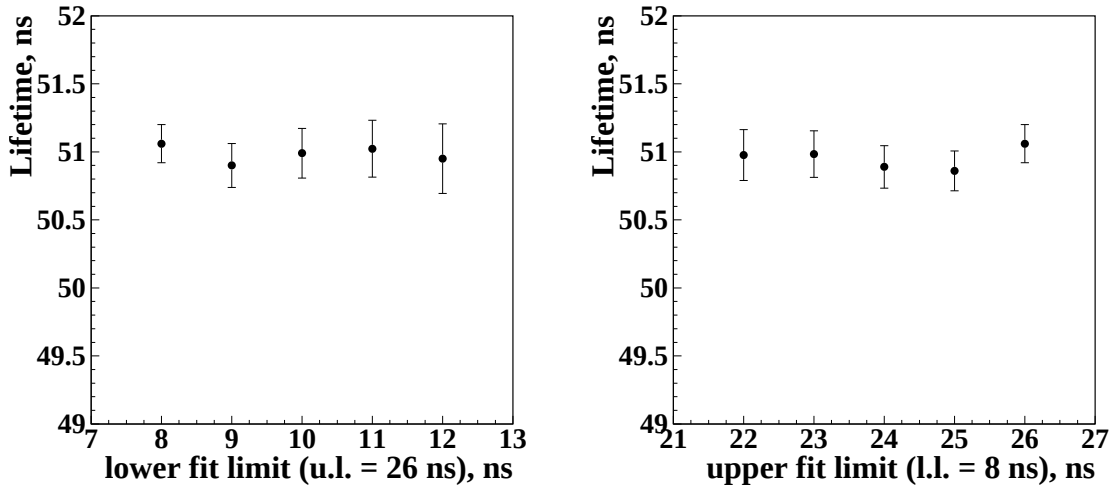

Figure 7.12: Result for the lifetime as a function of the lower (**left**) and upper (**right**) limit of the fit range.

the lifetime fit in the range between 8 and 26 ns with a factor 2 larger and smaller binning. The obtained relative variation of the K_L lifetime is $\sim 4 \cdot 10^{-4}$, thus also this systematic effect can be considered negligible.

7.2.5 Background shape

The overall L_K decay length and t^* proper time distribution shapes have been studied. As seen in Sec. 6.1.1, the main background sources are $K_L \to \pi^+\pi^-\pi^0$, $K_L \to K_S \to \pi^0\pi^0$ regeneration events and K_L nuclear interactions with detector materials, that contaminate the sample with a percentage of $\sim$1.72% (see Tab. 6.1 and Tab. 6.4, that respectively show the background percentage before and after the cuts). The data sample with $N_\gamma > 4$ photons is almost background free, while the background is essentially present in N_γ= 3, 4 photons data sample.

We are confident in the reliability of the Monte Carlo proper time distribution shape of the $K_L \to \pi^+\pi^-\pi^0$ background, because data and MC agreement has been checked several times in the control sample selected as described in Sec. 5.3.1.

The cross sections of the other two background sources (K_L nuclear interactions and regeneration) are not known with high accuracy, so the overall Monte Carlo shape of the t^* distribution has been changed, by varying artificially in turn the relative weight on one contribution by a factor 2 higher or lower, and rescaling the other one for the normalization.

The relative variation of the K_L lifetime due to the background shape has been estimated and corresponds to 0.08%.

7.2.6 Summary of corrections and systematic errors

Tab. 7.1 shows a summary of the corrections and systematic uncertainties associated to the K_L lifetime measurement.

Source	Correction	$\Delta\tau/\tau$(%)	$\Delta\tau$
Tagging efficiency	- 0.51 ns	0.32	0.16 ns
Reconstruction efficiency	-	0.16	0.08 ns
Selection efficiency	-	negligible	negligible
Time scale calibration	- 0.15 ns	0.12	0.06 ns
Nuclear interactions	+ 0.17 ns	0.16	0.08 ns
Fit range and binning	-	0.04	0.02 ns
Background shape	-	0.08	0.04 ns
Total	- 0.49 ns	0.42	0.21 ns

Table 7.1: Summary of corrections and systematic errors on the K_L lifetime measurement.

Then, the result for the K_L lifetime is:

$$\tau_L = (50.56 \pm 0.14_{\text{stat}} \pm 0.21_{\text{syst}}) \text{ ns} \tag{7.13}$$

Chapter 8

Conclusions

A measurement of the K_L meson lifetime with $\sim$1.2 fb^{-1} ($\sim$20 million events in the fit range) of KLOE data sample collected in 2005 has been discussed, using $K_L \to \pi^0\pi^0\pi^0$ events tagged by $K_S \to \pi^+\pi^-$ decays.

While the procedure of the data analysis is similar to that used for the previous KLOE measurement (Ref. [2]), it is important to stress that the data taking conditions between 2001-02 and 2004-05 runs have been changed, and the differences have been already mentioned in detail in Sec. 5.1.

A fit to the K_L proper time has been performed in a time range as wide as possible, between 8 and 26 ns, which amounts to about 36% of K_L lifetime. The overall efficiency for the detection of signal events is $\sim$98%, with a background contamination of only 1.72%. The obtained result is:

$$\tau = (50.56 \pm 0.14_{\rm stat} \pm 0.21_{\rm syst}) \text{ ns} \tag{8.1}$$

where both statistical and systematical errors have been improved with respect to previous KLOE "direct" measurement [2]:

$$\tau = (50.92 \pm 0.17_{\rm stat} \pm 0.25_{\rm syst}) \text{ ns} \ . \tag{8.2}$$

This result has been presented at KAON09 conference (2009 Kaon International Conference) in June (Ref. [44]).

A comparison between the two measurements can be done by looking at Tab. 8.1 and Tab. 7.1 in Sec. 7.2.6:

- the tagging efficiency systematic error contributions are partially correlated, this is due to a similar procedure to tag the K_L meson: as mentioned in Sec. 5.1, the same cylindrical fiducial volume for the K_S decay is required, and the same K_S momentum cut has been applied. In the present analysis the dipion invariant mass cut is looser ($\pm$15 MeV) with respect to the previous one ($\pm$5 MeV), to retain higher statistics, and finally, at least one of the two tracks arising from the K_S decay must have an associated cluster in the calorimeter of higher energy (E $\geq$ 100 MeV) with respect to the previous measurement (E $\geq$ 50 MeV), in order to reconstruct the event-start time $t_{0,\,evt}$.

  In both cases the systematic uncertainty comes from the variation of the efficiency slope as a function of the proper time when we vary the cut on the

Source	Correction (%)	$\Delta\tau/\tau$(%)	$\Delta\tau$
Tagging efficiency	- 0.6	0.25	0.13 ns
Acceptance	bin by bin	0.3	0.15 ns
Selection efficiency	bin by bin	$5 \cdot 10^{-5}$	negligible
Vertex resolution	-	0.1	0.05 ns
Background subtraction	bin by bin, + 0.2	0.2	0.10 ns
Background shape	+ 0.15	0.06	0.03 ns
Nuclear interactions	+ 0.33	0.16	0.08 ns
Momentum scale	-	0.1	0.05 ns
Time scale	-	0.07	0.04 ns
Total	+ 0.1	0.49	0.25 ns

Table 8.1: Corrections and systematic errors on the K_L lifetime measurement published by KLOE in 2005 (Ref. [2]).

pion cluster energy associated to a track coming from the K_S decay. Even if in the two measurements this cut is different, due to the different data taking conditions, the source of systematic error is physically the same and for this reason in the following we will conservatively consider this contribution to the systematic error as fully correlated.

It is also to be stressed that the evaluation procedure of this systematic contribution is extremely conservative, since it assumes a coherent shift upward or downward of all the cluster energies by one standard deviation. A detailed study of the detector effect that originates the slope of the tagging efficiency is going on, and will be implemented in the final measurement with a consistent reduction of the correlated systematic contribution;

- the reconstruction and selection efficiency systematic errors are completely uncorrelated, since different techniques have been used;

- the time scale calibration systematic errors are uncorrelated: in the previous measurement, no significant effect has been observed at the level of the control sample statistics available;

- the systematic errors from nuclear interactions are correlated, since they are based on the same KLOE measurement (see Ref. [42]); this will be matter of further studies on the 2005 data in the near future, by performing a dedicated measurement;

- the errors due to the fit range and binning are uncorrelated, since the fit procedure is completely different, as mentioned in Sec. 5.1;

- the uncorrelation of the background shape errors is due to an upgraded Monte Carlo (see Sec. 3.7), that includes machine background known on a run-by-run basis.

By summarizing, the only correlated uncertainties are the tagging efficiency and the nuclear interactions systematic error sources, all other systematics are evaluated on different conditions and cuts, so the present lifetime measurement

$$\tau = (50.56 \pm 0.14_{\text{stat}} \pm 0.11_{\text{uncorr syst}} \pm 0.18_{\text{corr syst}}) \text{ ns} \tag{8.3}$$

turns out to be compatible within $\sim$2 σ_{uncorr} from the central value of the previous measurement:

$$\tau = (50.92 \pm 0.17_{\text{stat}} \pm 0.20_{\text{uncorr syst}} \pm 0.15_{\text{corr syst}}) \text{ ns} . \tag{8.4}$$

Further improvements of the present result will be achieved soon: the statistical error will benefit from an axtension to lower proper times of the fit interval, while the systematical error can be reduced by means of a more detailed detector acceptance survey. The systematic uncertainty contribution due to the tagging efficiency will be soon reduced by means of a dedicated study.

Moreover the 2004 data sample analysis, which has to cope with a higher level of machine background, is being completed, yielding another slight improvement in the statistical uncertainty.

To conclude, the average of the previous and the present KLOE "direct" measurements, which accuracy are respectively $\sim$6 and $\sim$5 permil, taking into account of all the correlations, is:

$$\tau = (50.67 \pm 0.21) \text{ ns} \tag{8.5}$$

which relative error is $\sim$4.1 permil.

By averaging with other existing K_L lifetime measurements ([1, 3]) the error lowers from 0.41% of the present PDG value (Ref. [18]) $\tau = (50.99 \pm 0.21)$ ns to 0.33%, yielding an error contribution due to the K_L lifetime on the $|V_{\text{us}}| \times f_+(0)$ uncertainty of 0.17% instead of 0.19% for instance in the K_{e3} case (see Tab. 1.2).

This measurement brings a slight but not yet significant improvement in the $|V_{\text{us}}| \times f_+(0)$ determination accuracy. After the inclusion of the 2004 statistics and the reduction of the correlated systematic error of the final measurement, we expect to lower the lifetime error contribution to the $|V_{\text{us}}| \times f_+(0)$ determination.

Bibliography

[1] K. G. Vosburgh *et al.*, *Measurement of the K_L Mean Life*, *Phys. Rev. Lett.* **26** (1971) 866 and *Phys. Rev.* D **6** (1972) 1834.

[2] F. Ambrosino *et al.* (KLOE Collaboration), *Measurement of the K_L meson lifetime with the KLOE detector*, *Phys. Lett.* B **626** (2005) 15. [hep-ex/0507088]

[3] F. Ambrosino *et al.* (KLOE Collaboration), *Measurements of the absolute branching ratios for the dominant K_L decays, the K_L lifetime, and $V_{\rm us}$ with the KLOE detector*, *Phys. Lett.* B **632** (2006) 43. [hep-ex/0508027]

[4] G. D. Rochester and C. C. Butler, *Evidence for the existence of new unstable elementary particles*, *Nature Lond.* **160** (1947) 855.

[5] M. Gell-Mann, *Isotopic Spin and New Unstable Particles*, *Phys. Rev.* **92** (1953) 833.

[6] T. Nakano and K. Nishijima, *Charge independence for V-particles*, *Prog. Theor. Phys.* **10** (1953) 581.

[7] M. Gell-Mann and A. Pais, *Behavior of neutral particles under charge conjugation*, *Phys. Rev.* **97** (1955) 1387.

[8] K. Lande *et al.*, *Observation of Long-Lived Neutral V Particles*, *Phys. Rev.* **103** (1956) 1901.

[9] F. Muller *et al.*, *Regeneration and Mass Difference of Neutral K Mesons*, *Phys. Rev. Lett.* **4** (1960) 418.

[10] T. D. Lee and C. N. Yang, *Question of Parity Conservation in Weak Interactions*, *Phys. Rev.* **104** (1956) 254.

[11] C. S. Wu *et al.*, *Experimental Test of Parity Conservation in Beta Decay*, *Phys. Rev.* **105** (1957) 1413.

[12] R. L. Garwin *et al.*, *Observations of the Failure of Conservation of Parity and Charge Conjugation in Meson Decays: the Magnetic Moment of the Free Muon*, *Phys. Rev.* **105** (1957) 1415.

[13] P. Bassi *et al.*, *Demonstration of Parity Nonconservation in Hyperon Decay*, *Phys. Rev.* **108** (1957) 1353.

[14] T. D. Lee R. Oehme and C. N. Yang, *Remarks on Possible Noninvariance under Time Reversal and Charge Conjugation*, *Phys. Rev.* **106** (1957) 340.

[15] L. D. Landau, *On the conservation laws for weak interactions*, *Zh. Eksp. Teor. Fiz.* **32** (1957) 405.

[16] J. H. Christenson, J. W. Cronin, V. L. Fitch and R. Turlay, *Evidence for the 2π decay of the K_2^0 meson*, *Phys. Rev. Lett.* **13** (1964) 138.

[17] P. K. Kabir, *The CP Puzzle*. Academic Press, 1968.

[18] C. Amsler *et al.* (Particle Data Group), *Phys. Lett.* B **667** (2008) 1.

[19] S. Eidelman *et al.* (Particle Data Group), *Phys. Lett.* B **592** (2004) 1.

[20] P. Franzini, *Predicting the statistical accuracy of an experiment*, The Second DAΦNE Physics Handbook, Vol. II, p.823, ed. L. Maiani, G. Pancheri, N. Paver (1995). See also *Statistics, The method of maximum likelihood*, *Review of Particle Physics*, Phys. Lett. B **592** (2004) .

[21] N. Cabibbo, *Unitary Symmetry and Leptonic Decays*, *Phys. Rev. Lett.* **10** (1963) 531.

[22] M. Kobayashi and T. Maskawa, *CP-Violation in the Renormalizable Theory of Weak Interaction*, *Prog. Theor. Phys.* **652** (1973) 49.

[23] L. Wolfenstein, *Parametrization of the Kobayashi-Maskawa Matrix*, *Phys. Rev. Lett.* **51** (1983) 1945.

[24] C. Jarlskog, *Commutator of the Quark Mass Matrices in the Standard Electroweak Model and a Measure of Maximal CP Nonconservation*, *Phys. Rev. Lett.* **55** (1985) 1039.

[25] I. S. Towner and J. C. Hardy, *Improved calculation of the isospin-symmetry-breaking corrections to superallowed Fermi β decay*, *Phys. Rev.* C **77** (2008) 025501.

[26] A. Sirlin, *Large M_W, M_Z behaviour of the $O(\alpha)$ corrections to semileptonic processes mediated by W*, *Nucl. Phys.* B **196** (1982) 83.

[27] V. Cirigliano *et al.*, *Radiative corrections to $K_{\ell 3}$ decays*, *Eur. Phys. J* C **23** (2002) 121. `http://arxiv.org/pdf/hep-ph/0110153`

[28] M. Antonelli *et al.* (FlaviaNet Working Group on Kaon Decays), *Precision tests of the Standard Model with leptonic and semileptonic kaon decays*, arXiv:0801.1817 [hep-ph]. `http://arxiv.org/pdf/0801.1817`

[29] P. Franzini, Opening Remarks, PoS(KAON)002(2007).

[30] V. Bernard, M. Oertel, E. Passemar and J. Stern, *$K^L_{\mu 3}$ decay: A Stringent Test of Right-Handed Quark Currents*, *Phys. Lett.* B **638** (2006) 480. `http://arxiv.org/pdf/hep-ph/0603202`

[31] M. Adinolfi *et al.*, *The tracking detector of the KLOE experiment*, *Nucl. Instrum. Methods* **A488** (2002) 51.

[32] F. Ambrosino *et al.* (KLOE Collaboration), *Measurement of the DAΦNE luminosity with the KLOE detector using large angle Bhabha scattering*, *Eur. Phys. J* C **47** (2006) 589.

[33] M. Adinolfi *et al.*, *The KLOE electromagnetic calorimeter*, *Nucl. Instrum. Methods* **A482** (2002) 364.

[34] M. Adinolfi *et al.*, *The QCAL tile calorimeter of KLOE*, *Nucl. Instrum. Methods* **A483** (2002) 649.

[35] M. Adinolfi *et al.*, *The trigger system of the KLOE experiment*, *Nucl. Instrum. Methods* **A492** (2002) 134.

[36] R. Brun *et al.*, GEANT3, CERN-DD/EE/84-1 (1984).

[37] R. Brun *et al.*, GEANT: *Simulation for particle physics experiments, user guide and reference manual*, CERN-DD-78-2-REV (1978).

[38] A. Aloisio *et al.*, *Data acquisition and monitoring for the KLOE detector*, *Nucl. Instrum. Methods* **A516** (2004) 288.

[39] F. Ambrosino *et al.*, *Data handling, reconstruction, and simulation for the KLOE experiment*, *Nucl. Instrum. Methods* **A534** (2004) 403.

[40] S. Fiore and G. Venanzoni, *Quality selection for 2005 data*, KLOE MEMO n.331 (2006).

[41] F. Ambrosino *et al.* (KLOE Collaboration), *Precise measurements of the η and the neutral kaon meson masses with the KLOE detector*, *J. High Energy Phys.* **0712** (2007) 073.

[42] M. Antonelli, P. Beltrame, M. Dreucci, M. Moulson, M. Palutan, A. Sibidanov, *Measurements of the Absolute Branching Ratios for the Dominant K_L Decays, the K_L Lifetime and $|V_{\rm us}|$ with the KLOE Detector*, KLOE Note n. **204** (2005). `http://www.lnf.infn.it/kloe/kdocs/getfile.php?doc_fname=kn204.ps`.

[43] G. Lanfranchi, *Direct measurement of the K_L lifetime*, KLOE Note n.**203** (2005).
`http://www.lnf.infn.it/kloe/kdocs/getfile.php?doc_fname=kn203.ps`.

[44] S. Bocchetta, *Lifetimes of the K_S and K_L mesons and the absolute $K^+ \to \pi^+\pi^-\pi^+$ branching ratio with KLOE*, PoS KAON:006,2009.
`http://pos.sissa.it//archive/conferences/083/006/KAON09_006.pdf`.